Influence of a TESb flush on InAs/GaAs submonolayer stacks

vorgelegt von
Master of Science
Paul David Maximilian Quandt
geb. in Berlin

von der Fakultät II - Mathematik und Naturwissenschaften
der Technischen Universität Berlin

zur Erlangung des akademischen Grades
Doktor der Naturwissenschaften
- Dr. rer. nat. -

genehmigte Dissertation

Promotionsausschuss:
Vorsitzende: Prof. Dr. Kathy Lüdge
Gutachter: Prof. Dr. Dieter Bimberg
Gutachter: Prof. Dr. André Strittmatter
Gutachter: Prof. Dr. Armin Dadgar

Tag der wissenschaftlichen Aussprache: 24.08.2018

Berlin 2018

Zusammenfassung

Der sogenannte Submonolagen-Wachstumsmodus stellt eine Alternative zum konventionellen Stranski-Krastanov-Wachstumsmodus für die Herstellung von Quantenpunkten hoher Dichte dar. In bisherigen Untersuchungen zeigten solche Submonolagen-Stapel jedoch nur schwache Lokalisationseigenschaften. Der Einbau von Sb bietet die Möglichkeit, diese kontrolliert einzustellen.

In dieser Arbeit wurde ein MOCVD-Prozess entwickelt, in dem Sb mittels eines Pulses von Triethylantimon auf die Wachstumsoberfläche gebracht und im nachfolgenden Wachstum eingebaut wird. Die resultierenden strukturellen, elektronischen und optischen Eigenschaften der Submonolagen-Stapel, sowie deren Anwendung als aktives Medium in direktmodulierten Lasern wurden untersucht.

Entscheidend für die Analyse der elektronischen Eigenschaften ist es, den Einbau der Sb-Atome sowohl quantitativ zu erfassen als auch deren relative Position gegenüber den In-Atomen auf atomarer Ebene zu bestimmen. Dies ermöglicht sowohl eine Beschreibung des Einbauverhaltens mit Hilfe von Absorptionsmodellen als auch eine theoretische Vorhersage der elektronischen und optischen Eigenschaften indem die lokale Bandstruktur sowie der Einfluss auf die Elektron- und Loch-Wellenfunktion simuliert wird.

Ein präferierter Einbau von Sb in In-reichen Bereichen in den Submonolagen-Stapeln führt hier zu einer Ausdehnung der Elektronen-Wellenfunktion über mehrere dieser Bereiche, während die Loch-Wellenfunktion stärker in einzelnen Bereichen lokalisiert wird. Zusätzlich zur daraus resultierenden Verstärkung des elektrischen Dipolmoments ist hierdurch eine Rotverschiebung der Emissionswellenlänge zu erwarten.

Diese Vorhersagen konnten durch temperaturabhängige Photolumineszenzmessungen und räumlich aufgelöste Kathodolumineszenzmessungen bestätigt werden. Der Einbau von Sb führte zu einer Rotverschiebung der Emission, einer Zunahme der inhomogenen Verbreiterung der beobachteten Lumineszenz sowie der Intensität

von Phonon-Repliken. Zusätzlich zeigten sich einzelne Linien im integralen Emissionsspektrum.

Mittels der Menge an angebotenem Sb, der GaAs-Schichtdicke zwischen den InAs-Abscheidungen und der Anzahl der Wiederholungen des Wachstumszykluses konnten die Eigenschaften solcher Schichten zwischen denen einer nur in Wachstumsrichtung, also eindimensionalen, und denen einer dreidimensionalen Lokalisierung von Ladungsträgern variiert werden.

Da sich die Lumineszenzspektren von Submonolagen-Stapeln hinsichtlich ihrer inhomogenen Verbreiterung zwischen 10 und 50 nm in einem Wellenlängenbereich von 900 bis 1180 nm gezielt einstellen lassen, konnte der Einfluss dieser Kenngröße auf die Lasercharakteristik untersucht werden. Kantenemittierende Laserdioden mit Submonolagen-Stapeln als aktives Medium zeigen, wie zu erwarten, eine Verbreiterung des Gewinnspektrums mit zunehmender Lokalisation in der Submonolagen-Schicht. Dies hat potentielle Vorteile für die Wellenlängenabstimmbarkeit und die Anwendung in Lasern mit Modenkopplung. Direkt modulierte Laser mit Submonolagen-Stapeln sind gegenüber Quantenfilm-Strukturen trotz der sehr hohen Dichte an Lokalisationzentren in ihrer Grenzfrequenz limitiert durch einen reduzierten optischen Überlappfaktor und das stark verbreiterte Gewinnspektrum. Um die direkte Modulierbarkeit solcher Laser zu verbessern, sollte die inhomogene Verbreiterung etwas verringert werden. Weiterhin muss nach Wegen gesucht werden, den optischen Überlapp zwischen optisch geführter Mode und aktiver Schicht zu erhöhen.

Abstract

The so-called submonolayer growth mode poses an alternative to the conventional Stranski-Krastanov growth for the fabrication of high densities of quantum dots. Previous investigations, however, showed only weak confinement properties of these submonolayer stacks. The incorporation of Sb provides the possibility to intentionally tune the confinement properties.

In this work a MOCVD process was developed in which a pulse of triethylantimony leads to a deposition of Sb on the growth surface and its incorporation during the subsequent growth. The resulting structural, electronic and optical properties of the submonolayer stacks were investigated, as well as their application as active media in directly modulated lasers.

To analyze the electronic properties it is substantial to record the incorporation of Sb atoms quantitatively as well as to determine their position with respect to the In atoms on the atomic level. This not only enables the modeling of the incorporation behavior using adsorption models but also provides the possibility to theoretically predict the electronic and optical properties by simulating the local band structure and its influence on the electron and hole wave function.

A preferential incorporation of Sb into In-rich regions results in the expansion of the electron wave function across several of those regions while the hole wave function is localized more strongly in individual regions. In addition to the resulting increase of the electric dipole moment, a redshift of the emission wavelength is expected from this.

These predictions could be confirmed by temperature-dependent photoluminescence and spatially resolved cathodoluminescence measurements. The incorporation of Sb leads to a redshift of the emission, an increase of the inhomogeneous broadening of the observed luminescence and an increase of the intensity of phonon replicas. Moreover, individual emission lines were found in the integral spectrum.

Using the amount of supplied Sb, the thickness of the GaAs layer between InAs

depositions and the number of deposition cycles, the properties of such stacks can be varied between a localization only in growth direction, i.e. one-dimensional, and a three-dimensional confinement of charge-carriers.

As the inhomogeneous broadening of the luminescence spectra of submonolayer stacks can be intentionally tuned between 10 and 50 nm in the wavelength region of 900 to 1180 nm, the influence of this parameter on the laser characteristics could be investigated. As expected, edge-emitting laser diodes with submonolayer stacks as active medium showed a broadening of the gain spectrum with increasing localization in the submonolayer stack. This broadening may have benefits for the tuning of emission wavelengths and the application in mode-locked lasers. In contrast to quantum well structures, the cutoff frequency of directly modulated lasers with submonolayer stacks is limited despite the very high density of localization centers due to a reduced optical confinement factor, and the strongly broadened gain spectrum. To improve the direct modulation capabilities of such lasers, the inhomogeneous broadening needs to be reduced. Moreover, ways to increase the overlap between optically confined mode and active layer are of interest.

Publications

Parts of this work have already been published in:

- D.Quandt, J.-H. Schulze, A. Schliwa, Z. Diemer, C. Prohl, A. Lenz, H. Eisele, A. Strittmatter, U. W. Pohl, M. Gschrey, S. Rodt, S. Reitzenstein, and D. Bimberg, *Strong charge-carrier localization in InAs/GaAs submonolayer stacks prepared by Sb-assisted metalorganic vapor-phase epitaxy*, Physical Review B **91**, 235418 (2015)
- D. Quandt, J. Bläsing, and A. Strittmatter, *Analysis of InAsSb/GaAs submonolayer stacks*, Journal of Crystal Growth **494**, 1 (2018)

Conference Contributions

- *Evidence of quantum dot formation in Sb-assisted InGaAs/GaAs sub-monolayer growth*, International Nano-Optoelectronics Workshop 2013, Cargése, France
- *Charge carrier localization by Sb-assisted growth of InAs/GaAs sub-monolayer stacks*, Frühjahrstagung der Deutschen Physikalischen Gesellschaft (DPG) 2014, Dresden, Germany
- *Charge carrier localization in InAs(Sb)/GaAs sub-monolayer stacks*, International Conference on Quantum Dots 2014, Pisa, Italy
- *Localization of charge carriers in MOCVD-grown InAs(Sb)/GaAs sub-monolayer stacks*, DGKK Arbeitstreffen "Epitaxie von III-V Halbleitern" 2014, Magdeburg, Germany
- *Localization of charge carriers in MOCVD-grown InAs(Sb)/GaAs sub-monolayer stacks*, Frühjahrstagung der Deutschen Physikalischen Gesellschaft (DPG) 2015, Berlin, Germany
- *Enhanced localization of charge carriers in InAs(Sb)/GaAs submonolayer stacks*, European Workshop on Metal-Organic Vapour Phase Epitaxy (EWMOVPE) 2015, Lund, Schweden
- *Submonolayers with antimony and 1.3 µm low-density quantum dots*, DGKK Arbeitstreffen "Epitaxie von III-V Halbleitern" 2015, Göttingen, Germany

- *Influence of Sb as an additional atom species in MOCVD of InAs/GaAs submonolayer stacks*, International Conference on Metalorganic Vapor Phase Epitaxy, 2016, San Diego, USA
- *Sb-assisted MOCVD growth of InAs/GaAs submonolayers*, EMN Meeting on Epitaxy 2016, Budapest, Hungary
- *Influence of Sb on MOCVD-grown InAs/GaAs submonolayers*, DGKK Arbeitstreffen "Epitaxie von III-V Halbleitern" 2016, Duisburg, Germany
- *Characteristics of InAsSb/GaAs submonolayer lasers*, Frühjahrstagung der Deutschen Physikalischen Gesellschaft (DPG) 2018, Berlin, Germany
- *Incorporation of Sb into MOCVD-grown InAs/GaAs submonolayer stacks*, International Conference on Metalorganic Vapor Phase Epitaxy, 2018, Nara, Japan

Contents

1 Introduction

Light-emitting semiconductor devices have become an integral part of todays technology due to the ever increasing areas of application, e.g. in general lighting, automotive, cutting and welding as well as many more. Using gallium arsenide (GaAs) as a substrate basis, a large wavelength range in the near-infrared can be covered, allowing for a multitude of applications. Those include data transmission via plastic optical fibers [1, 2], photodynamic therapy of cancer [3–5] in the spectral range from 600 to 800 nm, to pump lasers for Nd:YAG or Nd:YLF lasers at about 808 nm [6–8] and lasers emitting at 850 nm [9–15] as well as 980 nm [16–23] for short reach optical interconnects. Emission wavelengths up to 1100 nm are also of interest for optical interconnects [24, 25] as well as for optical coherence tomography [26–28]. Operating wavelengths beyond 1100 nm have also been explored for frequency-conversion to yellow-green emission [29] as well as for data transmission applications [30, 31]. Even longer wavelengths of 1310 and 1550 nm enable device operation at the transmission windows of low attenuation in optical fibers [32, 33] and have been demonstrated as well [34–38].[1]

All of these applications were made possible by the development of the double heterostructure and, later, the separate confinement heterostructure (SCH) [39–41]. Quantum wells (QWs) [42–44], which provide electronic and optical confinement, led to significant improvements in laser performance as it increases the possibilities to achieve different emission wavelengths by adjusting composition and thickness of the quantum well and its barriers. With indium gallium arsenide (InGaAs) quantum wells surrounded by GaAs barriers, the short-wavelength limit at room temperature is given by the GaAs band gap of 1.42 eV [45, p. 116] while the long-wavelength limit is imposed by the formation of defects due to the large lattice mismatch ($\sim 3\%$ for $In_{0.4}GaAs/GaAs$), thus enabling emission between about 870 and 1240 nm [31].

A route towards better device performances is given by quantum dots (QDs),

[1] The given examples are for an operating temperature of about 300 K.

promising several advantages compared to quantum wells due to 3D carrier confinement. Those include an enhanced temperature stability, increased material gain and decreased threshold currents [46, 47]. In the In(Ga)As/GaAs material system, quantum dots are usually fabricated in the Stranski-Krastanov (SK) growth mode [48, 49]. To utilize this approach, a moderate but sufficiently large difference in lattice constant between the QD material and the substrate, i.e. a large enough strain has to be present. Provided such strained layer growth can be achieved, QDs may form because of free-energy minimization of the layer-substrate system. Previous works have found that the low composition limit lies at about 40% In-content in metalorganic chemical-vapor deposition (MOCVD) growth [50]. As excess strain-energy is realased upon QD formation, the spectral range can be extended to longer wavelengths, without employing additional materials. In(Ga)As quantum dots with a GaAs cap have been shown to reach emission wavelengths of up to 1320 nm [51–53]. If an InGaAs cap is used instead, even longer emission of up to 1520 nm has been realized [54].

Quantum dots have been successfully developed at the Technical University of Berlin for use as active media in directly modulated lasers [55–57], mode-locked lasers [58–63], distributed feedback lasers [64], semiconductor optical amplifiers [59, 65–73], and vertical cavity surface emitting lasers (VCSELs) [74, 75]. The typical base length of In(Ga)As/GaAs quantum dots grown in the Stranski-Krastanov growth mode is 7–26 nm [76–83], limiting the maximum areal density to about 10^{10}–10^{11} cm^{-2}. Therefore, the optical confinement factor of a quantum dot layer is reduced as compared to that of a quantum well with comparable thickness. This counteracts the beneficial influence of the increased material gain on the modal gain. Consequently alternative fabrication methods yielding larger quantum dot densities are of interest.

One such method is the submonolayer (SML) growth mode where cycled deposition of less than 1 monolayer (ML) indium arsenide (InAs) and a few MLs of GaAs results in a high density (10^{12} cm^{-2}) of In-rich regions [84, 85]. Semiconductor disk lasers [86], high power diode lasers [87] and VCSELs [88–91] using InAs/GaAs SML stacks as active media have been successfully demonstrated. Due to the high density of localization centers and the moderate localization potential, lateral electronic coupling results in optical properties best described by as a mixture of 0D and 2D states [85, 92]. Electronic structure modeling using eight-band k·p theory [93] suggests a delocalization of the electron wave function and hole wave functions localized

in In-rich regions. Such electronic configuration has therefore been termed heterodimensional and it has been postulated to be beneficial for high speed modulation [94].

In this thesis, the influence of Sb as an additional atom species during the growth of InAs/GaAs submonolayer stacks is investigated. As the method of supply, a TESb flush prior to each InAs deposition is chosen. After the analysis of structural, electronic and optical properties, the application of Sb-containing SML stacks as active media in devices is investigated. The work is structured as follows:

- **Chapter 2** starts with the basics of semiconductors and nanostructures. Additionally the influence of Sb incorporation on the electronic structure and the adsorption kinetics of materials during growth is discussed. Finally, the basic functionality of semiconductor laser diodes is described.

- **Chapter 3** describes briefly the experimental methods and processes used for sample fabrication and characterization.

- **Chapter 4** presents theoretical and experimental investigation of the structural, electronic and optical properties of SML stack with and without Sb by eight-band k·p simulations, X-ray based measurements, cross-sectional scanning tunneling microscopy (XSTM), as well as photoluminescence (PL) and cathodoluminescence (CL).

- **Chapter 5** deals with the application of SML stacks with Sb as active media in edge-emitting lasers using the previously obtained knowledge. The static laser characteristics are determined from L-I measurements on broad-area lasers as well as gain measurements on narrow-stripe lasers. Additionally, the dynamic characteristics are investigated by modulation measurements.

- **Chapter 6** summarizes the presented results and discusses possibilities for further research and application.

2 Fundamentals

This chapter provides informations on the background related to the investigations performed in this work by starting with the basic idea behind semiconductor nanostructures. Afterwards electronic and optical properties of quantum dots and submonolayer stacks are treated. It follows a discussion of the influence of Sb as an additional atom species during growth of InGaAs layers and Langmuir-type adsorption models of atomic species are presented. Finally, the characteristics of infrared laser diodes and their functionality are derived.

2.1 Semiconductor nanostructures

By confining at least one charge carrier type in one or more dimensions, its density of states changes according to the number of confined dimensions.

$$\rho_{3D} = \frac{1}{2\pi^2}\left(\frac{2m^*}{\hbar^2}\right)^{3/2}\sqrt{E} \tag{2.1}$$

$$\rho_{2D} = \frac{1}{\pi L_z}\left(\frac{m^*}{\hbar^2}\right)\sum_{i=0}^{n}\theta(E-E_i) \tag{2.2}$$

$$\rho_{1D} = \frac{1}{\pi L_y L_z}\left(\frac{m^*}{\pi^2\hbar^2}\right)^{1/2}\sum_{i=0}^{n}(E-E_i)^{-1/2} \tag{2.3}$$

$$\rho_{0D} = \frac{1}{\pi L_x L_y L_z}\sum_{i=0}^{n}\delta(E-E_i) \tag{2.4}$$

$L_{x,y,z}$ is the size of the potential well in the respective direction, m^* is the effective carrier mass, $\hbar = h/2\pi$ is the reduced Planck constant, E_i is the Eigenenergy of the carrier in the potential well. θ and and δ are the Heaviside step function, and the Dirac delta function, respectively.

In literature, two size limits are given, rendering such structures a nanostructure

or not. The first one is the de Broglie wavelength, which is defined as

$$\lambda_B = \frac{h}{p} = \frac{2\pi\hbar}{\sqrt{2m^*E}} = \frac{2\pi\hbar}{\sqrt{3m^*k_BT}} \tag{2.5}$$

where h and $\hbar$ are the Planck constant and its reduced variant, p is the momentum, m^* is the effective carrier mass again, $E = \frac{3}{2}k_BT$ is the particles energy, k_B is the Boltzmann constant and T is the temperature.

For typical semiconductors, the de Broglie wavelength for electrons is in the range of 7.3 to 73 nm at 300 K [95, p. 166]. A second definition is based on the exciton Bohr radius. For III-V semiconductors respective values are in the region from 2.9 to 101.7 nm [45, p. 234]. Both are illustrated in Fig. 2.1 for the binary semiconductor compounds used in this thesis.

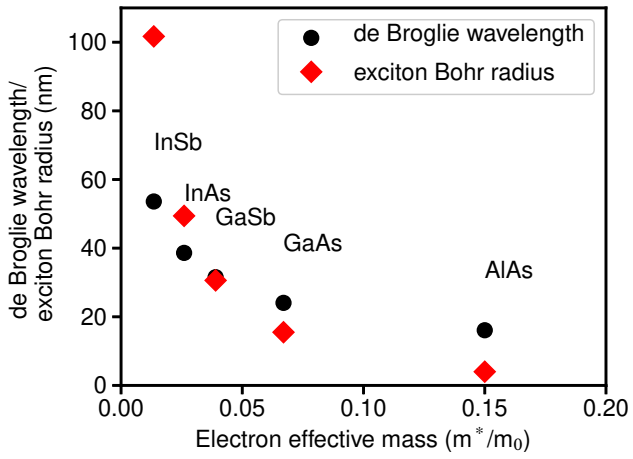

Figure 2.1: de Broglie wavelength for electrons at 300 K (calculated with data for m^* from [96]) and exciton Bohr radius (taken from [45, p. 234])) for selected III-V compounds.

If one or more dimensions of the structure are in the region of the two conditions mentioned above, the terms quantum well, quantum wire or quantum dot are applicable for one, two and three confined dimensions, respectively.

2.2 Growth and properties of quantum dots

Fabrication-wise, epitaxial growth can take place in three different growth modi [49]. Which of those occurs depends on the difference between the lattice constants of the substrate and the deposited material.

- In the **Frank-van der Merwe** growth mode [97], the lattice mismatch is small and two-dimensional layer growth proceeds up to virtual infinite layer thickness. Unless the lattice constant of the deposited material is identical to the lattice constant of the substrate (e.g. GaAs on GaAs or $In_{0.48}GaP$ on GaAs), the deposited layer is pseudomorphically strained. Strain generally imposes an upper thickness limit before the formation of defects. Several models for the prediction of this critical thickness exist, the most popular being the models by Matthews and Blakeslee [98] and People and Bean [99]. For InGaAs grown on GaAs, the maximum composition for which two-dimensional defect-free strained layer growth has been demonstrated is about 40% [31, 100, 101]

- A second possibility is given by the **Stranski-Krastanov** growth mode [48] which occurs for moderate but noticeable differences in lattice constant. Here, the deposited material initially grows two-dimensional. With increasing layer thickness, the strain energy increases proportionally. Once a critical layer thickness is reached, a material redistribution resulting in the formation of islands is energetically favorable. This growth mode is commonly observed for In-contents larger than 40%.

- For large differences in lattice constant, growth only happens in the form of three-dimensional islands. This is called **Volmer-Weber** growth [102]. This has been observed in for InAs/GaP quantum dots where the mismatch is 11.4 percent [103]. This growth mode is usually not observed for InGaAs on GaAs growth.

In the InAs/GaAs material system, the Stranski-Krastanov growth mode is the most popular way of realizing self-organized quantum dots. The necessary 2D/3D transition results in a typical size distribution. Quantum dots often take the shape of a truncated pyramid [79, 81, 104] and base lengths between 7 and 26 nm have been found by previous works [76–83].

Quantum dots have unique electronic and optical properties, resulting from the three-dimensional charge carrier localization. As shown in (2.4), the density of states becomes a delta function, which has been experimentally proven by spatially resolved cathodoluminescence [105] where spectrally narrow luminescence lines with widths below 0.15 meV were found within the integral spectrum. The electronic

properties of pyramidal quantum dots have been theoretically calculated [93, 106, 107], showing different extents for the electron and hole wave functions localized in the quantum dot according to the different effective masses of electrons and holes.

Due to this difference in spatial charge carrier localization, dipoles are formed by the electrons and holes localized in the quantum dot (excitons). In polar crystals like GaAs, this leads to a distortion of the surrounding crystal lattice. Recombination of the exciton leads to the disappearance of the dipole and thus, the cause of distortion. The lattice then relaxes by emitting a phonon. This can also be observed indirectly by luminescence measurements as in case of phonon emission, the energy of the emitted photon is reduced by the phonon energy and accordingly shifted peaks appear in the luminescence spectrum. The intensity ratio between these phonon replicas and the zero-phonon line is a measure for the probability of phonon emission and is described by a Poisson distribution [108, 200 and 208] [107, 109–111].

$$\frac{I_n}{I_0} = \frac{S^n \cdot e^{-S}}{n!} \tag{2.6}$$

Here, n is the number of involved phonons and S is the Huang-Rhys factor (HRF) [112] which is defined by the spatial overlap between the electron and hole wave functions [107, 113]. For InAs/GaAs quantum dots, Huang-Rhys factors of up to 0.03 have been theoretically and experimentally reported [110, 111].

Various advantages of quantum dots over quantum wells, including an increased material gain, decreased threshold current and improved temperature stability, have been theoretically [46, 47] and experimentally [78, 114] shown. Additionally, the growth as an ensemble of islands instead of fully strained, contiguous layers allows for a larger local In-content [81, 104]. Thus, smaller transition energies can be realized and the wavelength range is extended further to the infrared region.

Despite these advantages, quantum dots fabricated by Stranski-Krastanov growth are subject to some inherent limitations. The self-organized nature of the 2D/3D transition results in the above-mentioned typical base length. From this, a lower wavelength limit follows for InGaAs/GaAs quantum dots and room temperature emission below 1000 nm has rarely been reported [115]. Due to the size restriction, the maximum areal density is also limited to about 10^{10} – 10^{11} cm^{-2}. Therefore, the maximum achievable modal gain is limited as the optical confinement factor depends on the areal density. Additionally, self-organized growth leads to a size and composition distribution of the quantum dots, from which an inhomogeneous

energy broadening arises. This increases the gain bandwidth but at the same time further limits the achievable peak gain. Annealing of the quantum dot structures at sufficiently high temperatures is a tool to reduce the inhomogeneous broadening but additionally may result in a blueshift of the emission [116, 117].

2.3 Submonolayers

An alternative growth technique attempting to circumvent the density and size distribution limitations of SK quantum dots is the submonolayer growth mode.

Historically, the development of quantum well lasers with an ever decreasing well width led to the investigation of ultrathin quantum wells. One of the first publications dealing with the InAs/GaAs material system and having a well thickness around 1 ML was published by Gerard *et al.* [118], who observed excitonic emission with a small linewidth. Further investigations of ultrahin InAs insertions into GaAs all showed excitonic emission [119–123] being attributed to the localization of excitons at the InAs insertion. Although they can be considered as quantum dots, the presence of bound eigenstates in InAs insertions is questionable [124].

Later research focused on stacks of submonolayer which are formed by the the alternating deposition of nominally less than 1 ML and a few MLs of GaAs. Vertically correlated and anti-correlated ordering of islands is expected, depending on the spacer layer thickness [125]. XSTM measurements showed high lateral densities of In-rich regions with a density of around 10^{12} cm^{-2} while the lateral size was about 5 nm (see Fig. 2.2) [84, 85]. Furthermore it was found that In segregates into subsequent GaAs layers and a segregation coefficient of 0.75±0.07, corresponding to a segregation length of 0.98±0.32 nm or 3.48±1.13 MLs (GaAs), was determined [85].

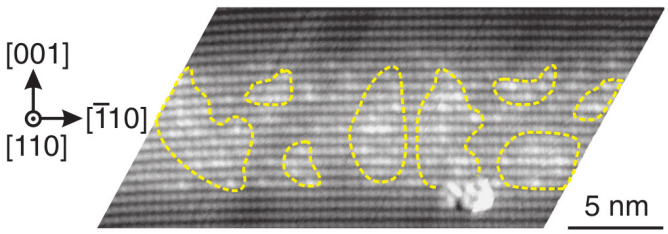

Figure 2.2: Filled-state XSTM image of a submonolayer stack with 5x 0.5 ML InAs and 4 ML GaAs. Taken from [84].

Electronically, as deduced from eight-band k·p simulations[1], a single column of InAs insertions localizes both electrons and holes (Fig. 2.3a). However, simulations of a 3x3 configuration of columns of InAs/GaAs SMLs suggest, both electron and hole wave functions may couple laterally between adjacent submonolayer columns (Fig. 2.3b).

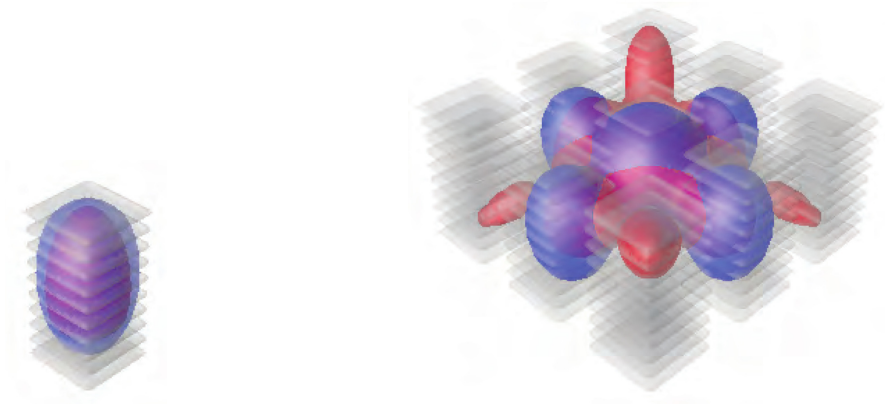

(a) **(b)**

Figure 2.3: Eight-band k·p simulation of electron (blue) and hole (red) wave functions in 10x submonolayer stacks. 0.5 ML thick InAs islands are separated vertically by 3 monolayers of GaAs. (a) Simulation of a single column. (b) Simulation of a 3x3 arrangement with a lateral spacing of 2 nm between the InAs islands. Taken from [126, 127].

An earlier investigation using micro-PL and temperature-dependent PL measurements already pointed out the coexistence of quantum dot and quantum well states in this system [92]. This was further confirmed by magneto-PL measurements, effective mass calculations and eight-band k·p simulations which used an In-distribution more closely reflecting the actual structural properties of the SML stacks as obtained from XSTM [94]. Here, the simulation was performed assuming spherical In-rich regions embedded into a homogeneous $In_{0.25}GaAs$ quantum well. This investigation has shown that the electron wave function is delocalized over several over these regions until the local In-content in the QDs reaches about 60%. In contrast, the hole wave function localizes at a much lower In-content. For this diverging behavior of the wave functions the electronic configuration was termed heterodimensional and it was speculated to be beneficial for high-speed operation of laser diodes.

Indeed, InAs/GaAs submonolayer stacks have sucessfully been used in high-speed

[1]Performed by Dr. Andrei Schliwa.

VCSELs with modulation speeds of up to 20 Gb/s [89–91]. Further successful applications include edge-emitting lasers [126–128], semiconductor disk lasers [86] and high-power diode lasers [87]. Additionally, the SML stacks were investigated experimentally and theoretically in semiconductor optical amplifiers [129, 130]. However, an analysis of the performance of SML-based lasers as a function of the degree of localization has not been presented up to now.

2.4 Changes in electronic configuration due to Sb

The addition of an additional chemical element to the already utilized material combination is a possibility to further tune the sample properties. By using isoelectronic atoms, i.e. atoms which are of the same group as the main constituting elements, in sufficient amounts, the band gap and the lattice constant can be tuned.

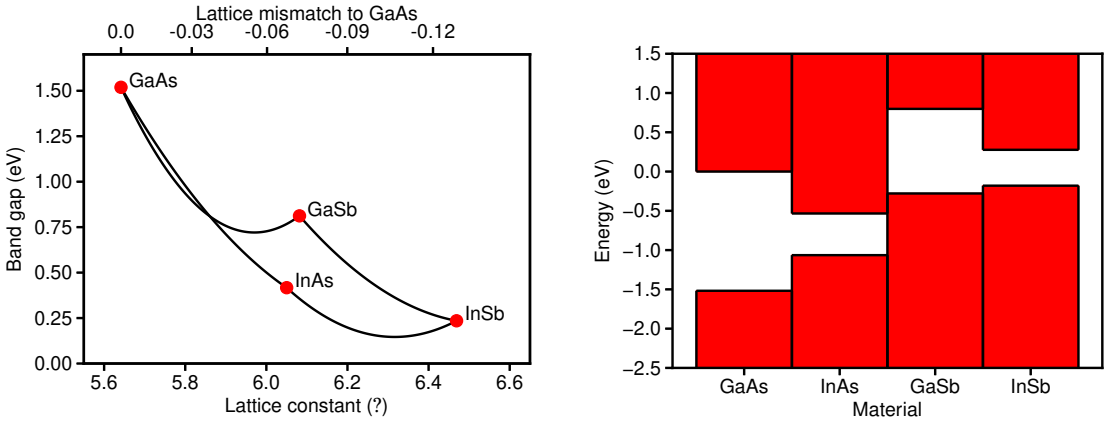

(a) **(b)**

Figure 2.4: III-V material parameters at 0 K as relevant for the investigated SML-stacks. (a) Bulk band gaps, lattice constants and mismatch to GaAs (drawn with data from [96]). (b) Band lineups for a 5 nm thick quantum well lattice matched to GaAs (calculated with the Schroeder program from [50]).

A first estimate of the influence of Sb incorporation into InGaAs can be gained by considering band gaps and lattice constants of the involved III-V binary materials (Fig. 2.4a, which additionally shows the lattice mismatch with respect to GaAs). Mechanically, the incorporation of Sb into GaAs has a very similar effect as the incorporation of In. The lattice constants of GaSb and InAs differ only by

about 0.6% (a_{InAs}: 6.0583 Å, a_{GaSb}: 6.0959 Å [96]), yielding lattice mismatches of 6.7% (InAs) and 7.2% (GaSb) with respect to GaAs (a_{GaAs} = 5.6533 Å [96]). Electronically, the decrease in band gap is also very similar until In- or Sb-contents of about 60%. Assuming a constant In content and thickness, the addition of Sb to an InGaAs quantum well would result in increased overall strain in the system while the decreased band gap leads to a further redshift of the emission energy.

The implicit assumption up to this point was an homogeneous distribution of In and Sb. In a disordered system like a submonolayer stack, however, the local In and Sb distribution is decisive. As mentioned previously (section 2.3), a large enough local In content may trigger localization of charge carrier wave functions. A very basic estimation of the effect of Sb on the charge carrier wave functions can be performed by considering the band lineups of the constituting binary materials. They can be theoretically calculated using the model-solid theory as proposed by van de Walle [131] which is based on fully self-consistent interface calculations. Using this, the band lineups of quantum wells lattice matched to GaAs can be calculated (Fig. 2.4b). From the energetic position of the bands of GaSb and InSb to GaAs and InAs one can expect as well rising energetic positions of the local conduction and valence bands of ternary and quaternary alloys with increasing Sb content. Therefore, a decrease of the electron localization and a simultaneous increase of the hole localization would follow at sites of increased Sb incorporation. A detailed investigation using eight-band k·p calculations[2] taking three different incorporation schemes into account is presented in section 4.1.1 of this thesis.

2.5 Langmuir-type adsorption models

An important aspect for the analysis of the submonolayer growth mode is the behavior of atoms reaching the sample surface. As such, they can either be adsorbed at the surface or desorb from it. A relatively simple framework describing this behavior was presented by Irving Langmuir in 1916[3] [132]. Assuming the sample surface has a finite number of sites per unit area n_{total}, incoming atoms can only adsorb at unoccupied sites n_{free} while desorption can only take place from occupied

[2]Performed by Dr. Andrei Schliwa.
[3]Nobel prize in Chemistry in 1932.

sites $n_{adsorbed}$ [133][4].

$$n_{total} = n_{free} + n_{occupied} \tag{2.7}$$

The rate of adsorption is controlled by the number of available free sites n_{free} and the number of atoms supplied by the gas phase which is proportional to the partial pressure P. In contrast, the rate of desorption is only dependent on the number occupied sites $n_{adsorbed}$. Thus rate equations for each number of sites can be established

$$\frac{dn_{free}}{dt} = -n_{free} \cdot P \cdot k_{ads} + n_{occupied} \cdot k_{des} \tag{2.8}$$

$$\frac{dn_{occupied}}{dt} = n_{free} \cdot P \cdot k_{ads} - n_{occupied} \cdot k_{des} \tag{2.9}$$

with k_{ads} and k_{des} being the respective reaction constants. By combining (2.7) with (2.9), a dependency for the number of occupied sites on the partial pressure can be derived. The resulting function is called a Langmuir isotherm and is obtained by assuming equilibrium conditions ($\frac{dn_{occupied}}{dt} = 0$).

$$\begin{aligned} &\underbrace{(n_{total} - n_{occupied})}_{n_{free}} \cdot P \cdot k_{ads} = n_{occupied} \cdot k_{des} \\ \Rightarrow \quad & n_{occupied} = \frac{n_{total} \cdot P \cdot k_{ads}}{k_{des} + P \cdot k_{ads}} \end{aligned} \tag{2.10}$$

An analytical expression for the occupied site density over time can be obtained by solving (2.9).

$$n_{occupied}(t) = \frac{n_{total} \cdot P \cdot k_{ads}}{k_{des} + P \cdot k_{ads}} \cdot (1 - \exp(-(k_{ads} \cdot P + k_{des}) \cdot t)) \tag{2.11}$$

The influence of time and partial pressure on the adsorption behavior is illustrated in Fig. 2.5. As also seen from (2.11), saturation values for the adsorbed atom density

[4]The original paper of Langmuir uses the surface coverage instead of the surface density. The former is simply the ratio of surface density and the maximum possible density. It is assumed that the surface can be covered by a single layer at maximum. From this follow $\Theta_{occupied} = \frac{n_{occupied}}{n_{total}}$, $\Theta_{free} = \frac{n_{free}}{n_{total}} = 1 - \Theta_{occupied}$, and $1 = \Theta_{free} + \Theta_{occupied}$. The notation used here is derived from the paper of Murota *et al.* [133].

are determined only by the partial pressure (Fig. 2.5b). Consequently, adsorption curves as a function of it will always saturate at maximum available site density (Fig. 2.5a). At sufficiently large partial pressure, the incorporation will reach a maximum value n_{total} at comparatively short time scales (Fig. 2.5b). In turn, at lower pressures, the density of adsorbed atoms will saturate at lower values. For a given set of adsorption and desorption constants, the main controlling growth parameter is therefore the partial pressure.

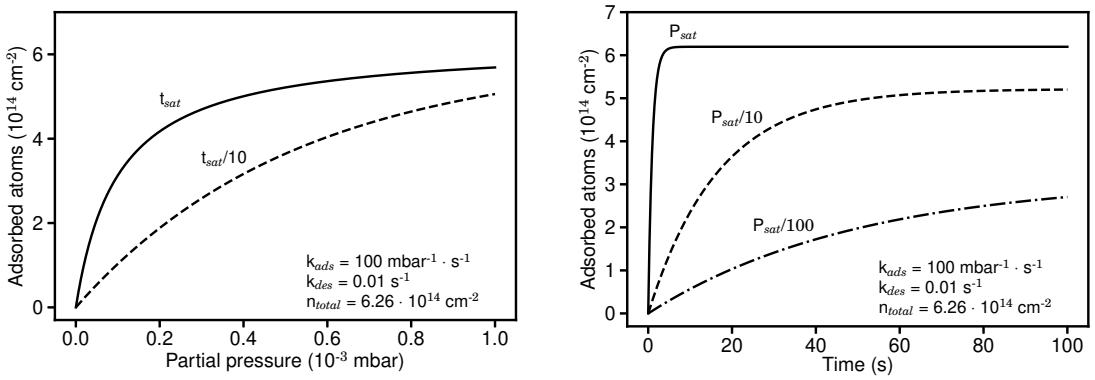

(a) **(b)**

Figure 2.5: Adsorption behavior according to Langmuir for different times and pressures. t_{sat} is chosen sufficiently large to ensure that the time-dependent part has saturated. Analogous for P_{sat}. (a) Density of adsorbed atoms with respect to partial pressure of the source gas at constant supply times. (b) Time-dependent density of adsorbed atoms at constant partial pressures.

By assuming that all of the adsorbed atoms are also incorporated during growth, this model can be used to analyze the atomic incorporation behavior during a flush of atoms. For such a analysis, the average number of incorporated atoms per unit area has to be experimentally determined. After the adsorption and desorption constants are obtained, such a model would be helpful to predict from growth parameters the incorporation of atoms into a single sheet of islands.

An extended model taking into account an only fractional incorporation of the adsorbed atoms into the final layer was presented by Murota *et al.* [133]. Here, the total number of atoms per unit area is given by

$$n_{total} = n_{free} + n_{adsorbed} + n_{reacted} \tag{2.12}$$

As before, n_{free} is the density of unoccupied sites while the density of occupied sites $n_{occupied}$ is now divided into sites with adsorbed atoms $n_{adsorbed}$ and sites where atoms have reacted and are actually incorporated into the crystal $n_{reacted}$.

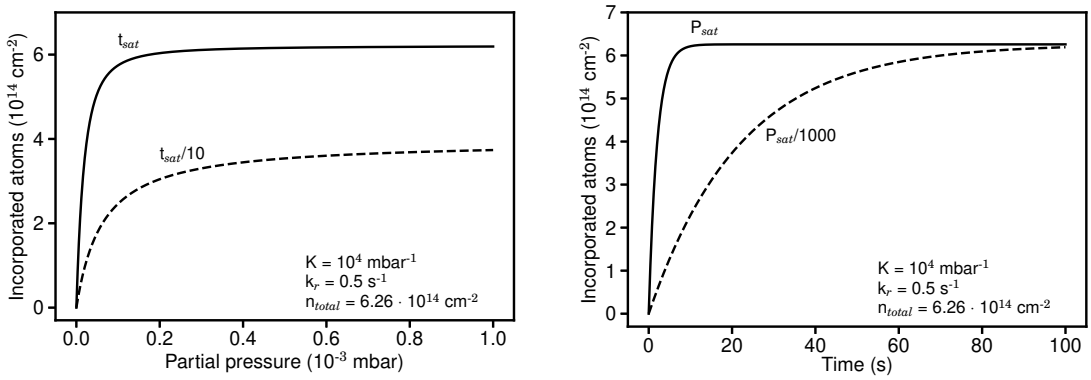

(a) **(b)**

Figure 2.6: Incorporation behavior according to the model proposed by Murota *et al.* [133] for different times and pressures. t_{sat} and P_{sat} are chosen sufficiently large to ensure that their respective contribution has saturated. (a) Density of incorporated atoms with respect to partial pressure of the source gas. (b) Time-dependent density of incorporated atoms.

The governing rate equations are then

$$\frac{dn_{free}}{dt} = -k_{ads} \cdot P \cdot n_{free} + k_{des} \cdot n_{adsorbed} \tag{2.13}$$

$$\frac{dn_{adsorbed}}{dt} = k_{ads} \cdot P \cdot n_{free} - k_{des} \cdot n_{adsorbed} - k_{reac} \cdot n_{adsorbed} \tag{2.14}$$

$$\frac{dn_{reacted}}{dt} = k_{reac} \cdot n_{adsorbed} \tag{2.15}$$

The analytical solution to (2.15) can be obtained by assuming thermal equilibrium for the adsorption component [133].

$$n_{reacted} = n_{total} \cdot (1 - \exp(-k_r \cdot \Theta \cdot t))) \tag{2.16}$$

$$\Theta = \frac{K \cdot P}{1 + K \cdot P}$$

Here, K is the ratio of the adsorption and desorption constants ($K = \frac{k_{ads}}{k_{des}}$).

Fig. 2.6 again shows the interaction between partial pressure and time. Opposed to the previous model, the additional reaction component now results in a much more significant influence of supply time on incorporated atom density. When atoms are adsorbed at the sample surface, they can either desorb again or be incorporated. As the latter mechanism is assumed to be irreversible, the number of available sites for adsorption and desorption continuously decreases with advancing time until eventually all sites are occupied with incorporated atoms (Fig. 2.6b). In case of short supply times, only a small fraction of the adsorbed atoms may get incorporated, regardless of partial pressure (Fig. 2.6a). This model is suited to analyze both pressure and time dependencies of atom incorporation.

2.6 Laser diodes

A simple description of the generation of light from matter is usually derived from a two-level system (Fig. 2.7). An electron on a higher energy level E_2 can radiatively recombine via two processes to a lower energy level E_1. The first one occurs spontaneously and is therefore accordingly called spontaneous recombination (Fig. 2.7a). The second process is a stimulated energetic transition of the electron by a photon of the same energy as the transition energy. Thereby, a second photon of the same energy and spatial direction is generated (Fig. 2.7b). This process is called stimulated emission and forms the basis for devices emitting coherent light, called lasers. The word laser in itself is an acronym and stands for **L**ight **A**mplification by **S**timulated **E**mission of **R**adiation.

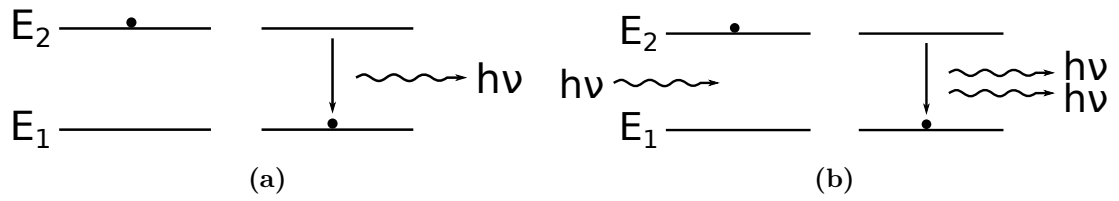

Figure 2.7: Radiative emission processes. Redrawn after [134]. (a) Spontaneous emission. (b) Stimulated emission.

In modern separate confinement heterostructure lasers light emission occurs in the active region providing the lowest transition energy and the largest confinement for charge carriers within the layer structure. The active region commonly consists of one or more quantum wells or alternatively one or more layers of quantum dots. In

order for the stimulated emission to become the dominant recombination process, a certain amount of feedback is necessary. Provided enough modal gain in the active region, the cleaved facets of an edge-emitting laser have a large enough reflectivity and provide sufficient feedback to enable transition into the lasing regime.

The performance of a semiconductor laser can be evaluated in terms of a number of device parameters as discussed in the following.

Internal parameters

A photon passing through a cavity with an inverted active medium can experience three different mechanisms:

1. The photon can stimulate the emission of another photon (Fig. 2.7b).

2. Internal loss mechanisms (scattering, absorption) destroy the photon as potential photon generator.

3. The photon can escape the cavity via one of the mirrors.

The overall change in intensity of light which completes a round-trip through a cavity is described by

$$\frac{I_2}{I_1} = \underbrace{R_1 R_2}_{3.} \cdot \exp((\underbrace{\Gamma g(J)}_{1.} - \underbrace{\alpha_i}_{2.}) \cdot 2L) \tag{2.17}$$

In this equation, I_1 and I_2 are the light intensities before and after the cavity round-trip, $R_{1,2}$ is the respective reflectivity of the mirrors which can be calculated using refractive indexes of semiconductor materials from the Afromowitz model [135], Γ and g(J) are optical confinement factor and material gain provided by the active region at a given current density, α_i are internal losses, and L is the cavity length. The numbers mark the associated effect as mentioned above.

The onset of lasing is defined as the point where the intensity after a cavity round-trip is unchanged, i.e. $I_1 = I_2$. From this, (2.17) can be rearranged, yielding the lasing condition

$$R_1 R_2 \cdot \exp\Big((\Gamma g_(J) - \alpha_i) \cdot 2L\Big) = 1$$
$$\Rightarrow \Gamma g(J) = \alpha_i + \underbrace{\frac{1}{2L} \ln\left(\frac{1}{R_1 R_2}\right)}_{\alpha_m} \tag{2.18}$$

where α_m are the mirror losses.

With this, the response of a semiconductor laser to any excitation source gets divided into two regimes, one below and one above the lasing threshold. Both regimes can usually be clearly distinguished in the dependence of the light power on the injection current (also known as the L-I curve of a laser, compare Fig. 2.8).

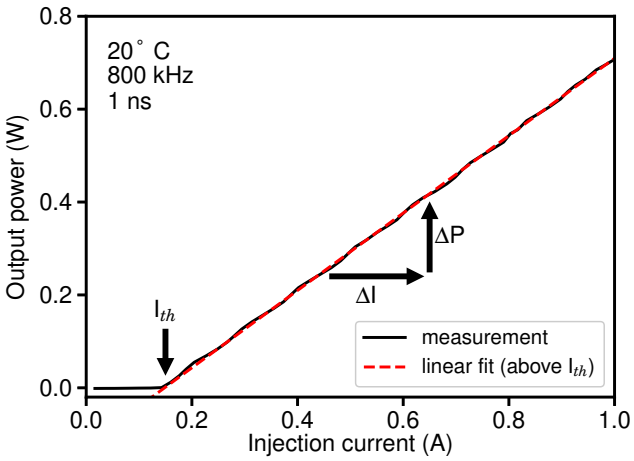

Figure 2.8: Example of an experimentally measured L-I curve obtained from a measurement of a 100 µm wide broad-area laser at pulsed excitation. Adapted from [136].

From the slope above threshold, the efficiency of the device in converting injected charge carriers to photons can be extracted. This is the external differential quantum efficiency and is defined as

$$\eta_{ext} = \frac{\text{Number of photons}}{\text{Number of charge carriers}} = \frac{\Delta P \cdot \lambda}{h \cdot c} \cdot \frac{e}{\Delta I} \tag{2.19}$$

ΔP and ΔI are respective changes in output power and drive current, h is the Planck constant, e the elementary charge, λ and c are the emission wavelength of the device and the speed of light, respectively.

To draw conclusions regarding the employed active region, the internal quantum

efficiency has to be determined. External and internal quantum efficiency are connected by the ratio of the mirror losses to the sum of internal and mirror losses. By using α_m from (2.18), one obtains [137, 138]

$$\begin{aligned} \eta_{ext} &= \eta_i \cdot \frac{\alpha_m}{\alpha_i + \alpha_m} \\ \Rightarrow \frac{1}{\eta_{ext}} &= \frac{1}{\eta_i} \cdot \left(1 + \frac{\alpha_i}{\ln\left(\frac{1}{R}\right)} \cdot L\right) \end{aligned} \tag{2.20}$$

Performing length-dependent L-I measurements therefore enables extraction of η_i and α_i.

Another parameter of interest is the current density at which the material becomes transparent, i.e. where the generated light compensates internal losses. Here, the lasing condition (2.18) can be extended by an empirical relation between material gain and current density, where g_0 is the gain parameter at the point of material transparency, J_{tr} is the corresponding transparency current density and J_{th} is the threshold current density [139–141].

$$g(J_{th}) = g_0 \cdot \ln\left(\eta_i \frac{J_{th}}{J_{tr}}\right) \tag{2.21}$$

With this, two equivalent ways of obtaining J_{tr} and Γg_0 are available. In the first one, the internal losses α_i as obtained from length-dependent L-I measurements, the calculated refractive index, and the laser length are used to calculate the corresponding threshold modal gain. The results are plotted versus measured threshold current density for each laser length. Afterwards, a fit of (2.21) to the obtained data points is performed, yielding the parameters in question.

Alternatively, (2.21) helps to rearrange (2.18) which yields

$$J_{thr} = \frac{J_{tr}}{\eta_i} \exp\left(\frac{\alpha_i + \frac{1}{L}\log\left(\frac{1}{R}\right)}{\Gamma g_0}\right) \tag{2.22}$$

This allows extraction of Γg_0 and J_{tr} from the dependence of threshold current density on inverse cavity length.

In both cases, the threshold current density can easily be extracted from the intercept of the linear fit above threshold with the x-axis (Fig. 2.8). If the confinement

factor Γ is known, e.g. by calculation from the laser geometry with an effective index method [142, 143], g_0 can be calculated. As this value is inferred from the measured output power, it is averaged over the whole emission spectrum.

To determine a spectrally resolved gain, another measurement technique is necessary. A simple method was proposed by Hakki and Paoli [144, 145]. Here, high-resolution optical spectra are recorded for drive currents below threshold. Based on an analysis of multi beam interference, the gain can then be calculated from the ratio of the maxima and minima of the longitudinal modes as follows

$$G_i = \frac{1}{L}\ln\left(\frac{\sqrt{r_i}-1}{\sqrt{r_i}+1}\right) + \frac{1}{L}\ln\left(\frac{1}{R}\right) \tag{2.23}$$
$$\text{with } r_i = \frac{P_i + P_{i+1}}{2V_i}$$

P_i is the ith Peak in the longitudinal mode spectrum and V_i is the valley. From this analysis, the net modal gain of each mode ΓG_i is obtained. A prerequisite for this technique is the selection of a single lateral mode. This can either be done by performing the measurement on narrow-stripe lasers which are laterally single-mode or by using spatial far field filtering [146].

A drawback of this technique is sensitivity to noise if the measured output power is not sufficient. In such cases, one can alternatively apply a nonlinear least-squares fitting method to fit each mode individually with an Airy function [147, 148].

$$I(\lambda) = \frac{C(\lambda)}{(1-P_{RG}(\lambda))^2 + 4\cdot P_{RG}(\lambda)\cdot \sin^2\left(2\cdot\pi\cdot n_g\cdot L\cdot\left(\frac{1}{\lambda}-\frac{1}{\lambda_0}\right)\right)} \tag{2.24}$$
$$\text{with } C(\lambda) = C(\lambda_0) + \gamma\cdot(\lambda-\lambda_0)$$
$$\text{and } P_{RG}(\lambda) = P_{RG}(\lambda_0) + \beta\cdot(\lambda-\lambda_0)$$

In this function, $C(\lambda)$ and $P_{RG}(\lambda)$ vary linearly with wavelength to account for an asymmetry of the mode caused by gain dispersion [148]. By fitting this function to each individual mode in the optical spectrum, the group index n_g, mode wavelength λ_0, mode intensity C_0 as well as its adjustment parameter γ and finally the gain-reflectivity product P_{RG} and its dispersion parameter β is obtained. The net modal

gain can finally be calculated from the gain-reflectivity product via

$$G = \frac{1}{L} \cdot \ln\left(\frac{P_{RG}}{R}\right) \tag{2.25}$$

Lastly, the internal loss α_i can be determined from the long wavelength region of the obtained gain spectra as the gain is assumed to be negligible there [149].

Through repeated measurements at different drive currents below threshold, the gain current relation (2.21) can again be used to extract g_0. With this, the material gain g_{mat} is obtained from

$$G = \Gamma g_{mat} - \alpha_i \tag{2.26}$$

Another parameter that can be extracted from optical spectra is the group index either from the fitting of equation 2.24 or directly from mode spacing via

$$n_g = \frac{\lambda^2}{L \cdot \Delta\lambda} \tag{2.27}$$

It yields the average group velocity v_g and the photon lifetime in the cavity τ_p by [150]

$$v_g = \frac{c}{n_g} \tag{2.28}$$

$$\tau_p = \frac{1}{v_g\left(\alpha_i + \frac{1}{L}\ln\left(\frac{1}{R}\right)\right)} \tag{2.29}$$

As a last basic figure of merit, the temperature stability of a laser can be examined. Here, the change in threshold current with temperature is of interest. It is often analyzed using the following exponential function

$$J_{thr}(T) = J_{thr}(0) \cdot \exp\left(\frac{T}{T0}\right) \tag{2.30}$$

which yields the temperature coefficient T_0.

Modulation response

All previously extracted parameters are relevant for applying a constant drive current to a laser diode. In the field of data transmission, however, the optical response

of laser diodes to modulated drive currents is of interest.

The most common description for temporal behavior of laser diodes is given by a set of rate equations, describing the charge carrier density in the SCH region and the active region (e.g. a quantum well)as well as the photon density in the latter [151, p. 308].

$$\text{Carrier density in SCH region: } \frac{dN_{SCH}}{dt} = \frac{\eta_i \cdot I}{q \cdot V_{SCH}} - \frac{N_{SCH}}{\tau_s} + \frac{N \cdot V_{QW}}{\tau_e \cdot V_{SCH}} \tag{2.31}$$

$$\text{Carrier density in QW region: } \frac{dN}{dt} = \frac{N_{SCH} \cdot V_{SCH}}{\tau_s \cdot V_{QW}} - \frac{N}{\tau} - \frac{N}{\tau_e} - v_g \cdot g \cdot N_p \tag{2.32}$$

$$\text{Photon density: } \frac{dN_p}{dt} = \Gamma v_g g N_p + \Gamma \beta R_{sp} - \frac{N_p}{\tau_p} \tag{2.33}$$

$\frac{\eta_i \cdot I}{q \cdot V_{SCH}} \Rightarrow$ Pump current

$\frac{N_{SCH}}{\tau_s} \Rightarrow$ relaxation from SCH to QW

$\frac{N \cdot V_{QW}}{\tau_e \cdot V_{SCH}} \Rightarrow$ escape from QW to SCH

$\frac{N}{\tau} \Rightarrow$ spontaneous recombination

$v_g g N_p \Rightarrow$ stimulated recombination

$\frac{N_p}{\tau_p} \Rightarrow$ photons leaving the cavity

Here, τ_s is the transport time between SCH and QW, τ_e is the thermionic emission time and τ is the spontaneous recombination lifetime. V_{QW} and V_{SCH} are the volumes of the QW and SCH region, and β is the fraction of spontaneous emission into the mode.

Assuming only a small modulation around a working point and setting

$$I = I_0 + I_1 \exp(i\omega t) \tag{2.34}$$

$$N = N_0 + N_1 \exp(i\omega t) \tag{2.35}$$

$$N_p = N_{p0} + N_{p1} \exp(i\omega t) \tag{2.36}$$

enables the derivation of an analytical equation known as the transfer function

which describes the optical response of the laser with respect to the frequency of the applied modulation.

$$|H(f)| = \frac{f_R^2}{\sqrt{(f_R^2 + f^2)^2 + \frac{f^2\gamma^2}{4\pi^2}}} \cdot \frac{1}{\sqrt{1 + 4\pi^2 f^2 \tau_s^2}} \tag{2.37}$$

Here, f_r is the resonance frequency and γ is the damping factor. These parameters are obtained by fitting the transfer function to a measured small-signal response curve.

By repeating this measurement at several working points, some figures of merit can be derived from the parameter relation to the drive currents.

The first is the D-factor, which is given by the resonance frequency with respect to the square root of the current above threshold [152, 153].

$$f_r = D \cdot \sqrt{I - I_{th}} \tag{2.38}$$

$$D = \frac{1}{2\pi}\sqrt{\frac{\eta_i \Gamma v_g}{qV}\frac{\partial g/\partial n}{\chi}} \tag{2.39}$$

While the transport factor χ is assumed to be 1 for simplicity, the internal quantum efficiency from broad area laser measurements, the calculated confinement factor and group velocity as extracted from optical spectra recorded for the gain measurements enter into the formula to extract the differential gain $\partial g/\partial n$.

The second factor to be extracted is the so called K-factor which is defined by the relation of damping factor and squared resonance frequency [154].

$$\gamma = K \cdot f_r^2 + \gamma_0 \tag{2.40}$$

$$K = 4\pi^2 \left(\tau_p + \frac{\varepsilon\chi}{v_g \frac{\partial g}{\partial n}}\right) \tag{2.41}$$

Together with the previously obtained parameters, the gain compression factor ε can be determined from this fit.

Lastly, the -3-dB frequency with respect to the square root of the current above

threshold yields a modulation current efficiency factor (MCEF) [155].

$$f_{3dB} = MCEF \cdot \sqrt{I - I_{th}} \tag{2.42}$$

Apart from measurements for extracting physical parameters for comparative purposes, the suitability of a laser for data transmission applications can be tested by performing large-signal experiments.

Here, a working point is chosen again but in contrast to small-signal measurements, the modulation amplitude is significantly larger. For the modulation signal, a square signal with a pattern as defined by a pseudo-random binary sequence (PRBS) [156] is used. The resulting optical signal is collected by a detector and subsequently recorded by a sampling oscilloscope, resulting in a so-called eye diagram. As a simplest quality measure, the presence or absence of data points in the eye opening is taken, i.e. errors where a distinction between 0 and 1 is not possible. With increasing modulation speed, the amount of errors increases. The ratio between wrongly received and total received bits is the bit-error ratio (BER). More detailed accounts concerning eye diagrams and BER measurements can be found in [157] and [158].

3 Experimental methods

In this chapter, the fabrication and characterization methods employed in this work are presented. It starts with a short summary of MOCVD with which all samples in this thesis are fabricated. Afterwards, the methods for the characterization of structural and optical properties are presented. Finally the processes used for the fabrication and characterization of laser devices are briefly described.

3.1 Sample fabrication

Metalorganic chemical vapor deposition, is a technique which was first demonstrated in the 1960s for GaAs [159, 160] and has since then been applied to fabricate an ever increasing variety of semiconductor materials and layer structures [161–168]. The thermal and catalytic decomposition of precursor molecules and the subsequent adsorption and incorporation at the surface of a crystalline substrate surface form the basis for this process. Nowadays it is the most widely used growth technology for the high-volume fabrication of compound semiconductor devices. Detailed accounts of the involved processes of as well as possible precursors and materials can be found in [169–171].

A commercial Aixtron 200/4 machine with a horizontal quartz reactor and an infrared lamp heater was used to perform the epitaxial growth in this thesis. Standard conditions are a reactor pressure of 100 mbar at a total flow of 15 sccm with hydrogen as carrier gas and have been used for all samples. Available group-III precursors are TMGa, TMIn, and TMAl while group-V sources are TBAs, TESb, and AsH_3. Doping for lasers structures can be achieved by using SiH_4, CBr_4 and DMZn.

Exactly oriented n-doped GaAs(001) 2" wafers were used as substrates for nearly all samples, the exception being doping level calibration samples which were grown on undoped substrates.

A thermocouple inside the graphite susceptor measures the reactor temperature. The actual substrate temperature is about 20° C lower [172]. All temperature values given in this thesis are nominal values.

A Laytec EpiRAS is employed to monitor and record the sample reflectivity during an epitaxy. This allows for the detection of potentially developing sample roughness during a process run as well as the determination of growth rates for sufficiently thick layers from the Fabry-Pérot oscillations.

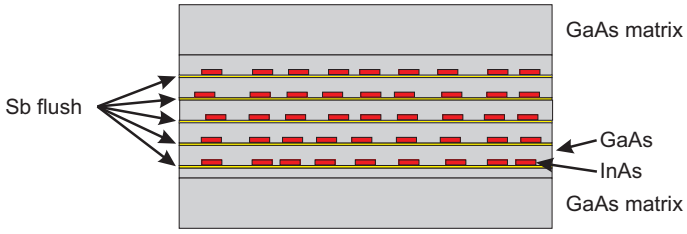

Figure 3.1: Basic submonolayer structure, here a 5x SML-stack. The InAs insertions are marked in red and the TESb flush is indicated in yellow.

With the exception of a few calibration samples for laser structures, all samples contain one or more submonolayer stacks. In general, the growth starts with a deoxidation of the samples at 735° C, followed by a GaAs buffer at 700° C. All subsequent layers up until the SML stacks are also grown at this temperature.

The basis structure of the SML stacks is shown in Fig. 3.1. Growth parameters which were employed previously to successfully fabricate semiconductor disk lasers [86] were used as a starting point for this work. A low growth temperature of 520° is used which corresponds to the usual temperature range around 500° usually used for the growth of quantum dots [50, 127, 172] to avoid clustering by long range adatom diffusion [173]. To prevent In/Ga intermixing [86], a low V/III of 2 for InAs and 2.5 for GaAs was used in the SML growth cycle. Low growth rates of 0.044 ML/s and 0.4 ML/s were chosen for InAs and GaAs, respectively. The employed SML tuning parameters in this thesis were the number of deposition cycles and the GaAs spacer growth time.

Sb was supplied in the form of a TESb flush prior to each InAs deposition during which all other sources were disabled. Control of the nominally supplied amount was given by varying the flush time or partial pressure.

To achieve optimal device performances, cladding layers should feature smooth surfaces and low point defect densities which is only achieved at sufficiently high

growth temperatures above 600° C [173]. Consequently, the temperature was increased to 615° after deposition of the SML stack. Higher overgrowth temperatures were not employed to prevent potential intermixing, which has been shown on quantum dots to cause a blueshift of the emission wavelength [116, 117].

3.2 Sample characterization

3.2.1 X-ray diffraction

The average composition and thickness of the SML stacks was determined from X-ray diffraction measurements on 5-fold SML/GaAs superlattice structures (Fig. 3.2). For this purpose ω-2Θ-scans around the GaAs(004) reflection were performed using a commercial Panalytical X'pert Pro MRD setup operating with the Cu-Kα line (1.54 Å or 8.04 keV).

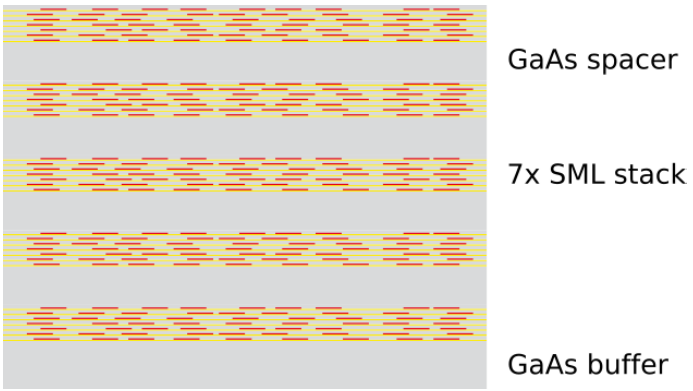

Figure 3.2: Sample structure for X-ray based measurements.

Data analysis was performed either by employing Panalytical's X'pert Epitaxy software or with the python package xrayutilities [174]. It is noted here that the actual SML stack structure is not resolved by this method. Instead, each single SML stack appears as a more or less homogeneous InGaAs layer. Consequently, an InGaAs/GaAs superlattice was assumed for the analysis. From the obtained thickness and composition of the SML stack, the average thicknesses of the InAs and GaAs depositions within the stack can be calculated. To resolve the actual SML structure, X-ray reflectivity (XRR) measurements (see section 3.2.2) were applied on the same samples.

An important point in the analysis of quaternary $In_xGa_{1-x}As_{1-y}Sb_y$ alloys is the influence In and Sb of on diffracted X-rays. Two effects need to be considered. The first one is the similar influence In and Sb have on the lattice constant (section 2.4, Fig. 2.4a). Within the range of In or Sb content used in this work of about 40% total content, the difference in lattice constant between $In_{0.4}GaAs$ and $GaAsSb_{0.4}$ is only about $\sim 0.3\%$ ($a_{In_{0.4}GaAs} \approx 5.815$ Å, $a_{GaAsSb_{0.4}} \approx 5.830$ Å). Consequently, only a minor shift of the diffraction angle can be observed when varying the In/Sb ratio. Secondly, the scattering and structure factors of the constituting have to be taken into account. The scattering factors have been theoretically calculated by Cromer and Mann [175] who also provided the following analytical formula.

$$f\left(\frac{sin(\Theta)}{\lambda}\right) = \sum_{i=1}^{4} a_i \cdot \exp\left(-b_i \cdot \frac{sin^2(\Theta)}{\lambda^2}\right) + c \tag{3.1}$$

a_i, b_i and c are fitting coefficients obtained from the simulations in [175], λ is the X-ray wavelength in Å and Θ is the diffraction angle. The angle-dependent scattering factors have been calculated using the Cu-Kα wavelength and are shown in Fig. 3.3a. To determine the influence of In and Sb atoms in the diffracted X-ray intensity, the structure factor of In_xGaAs and $GaAsSb_x$ needs to be calculated. For the (004)-reflection of a fcc-lattice like GaAs it is defined by the group-III and group-V scattering factors [176]

$$S = 4 * (f_{III} + f_V) \tag{3.2}$$

In the case of ternary materials, (3.2) needs can be modified to include the composition

$$S = 4 * (x * f_{III,1} + (1 - x) \cdot f_{III,2} + f_V) \tag{3.3}$$

Analogous for mixing on the group-V sublattice. Using (3.3), the structure factors of In_xGaAs and $GaAsSb_x$ can be calculated for the GaAs(004) reflection (see Fig. 3.3b), yielding virtually identical results.

Therefore, simulations with a constant In+Sb content but varying In/Sb ratios result in very similar diffraction curves (see Fig. 3.4), preventing an unambiguous determination of the quaternary layer composition. Only the In+Sb content can be obtained from XRD measurements.

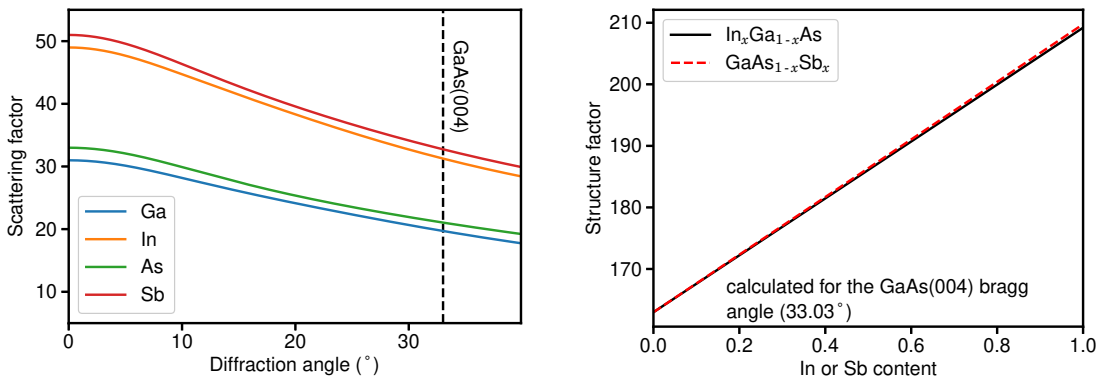

(a) **(b)**

Figure 3.3: Calculation of (a) the angle-dependent scattering factors for the elements relevant to the SML growth and (b) the structure factors of involved ternary compounds.

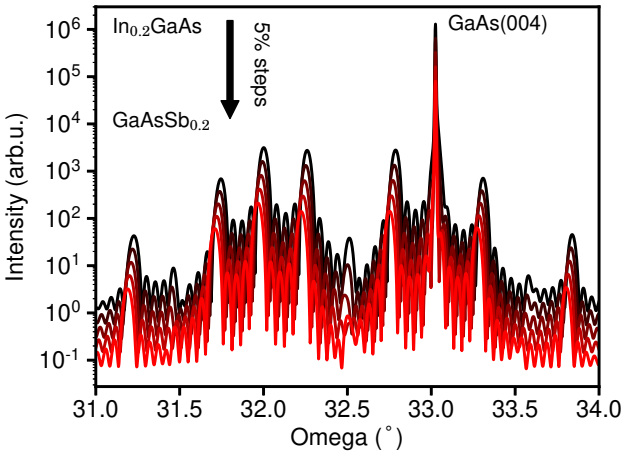

Figure 3.4: Simulation of X-ray diffraction curves for varying In/Sb ratios at a constant In+Sb content. The assumed sample structure is a 5-fold superlattice, containing 10 nm thick $In_xGa_{1-x}As_{1-y}Sb_y$ separated by 10 nm GaAs. Curves are vertically shifted for clarity.

To separate the determined composition into the contributions of In and Sb, an additional characterization method is necessary. In this thesis, grazing-incidence X-ray fluorescence (GIXRF) was utilized for this task (see. section 3.2.3).

3.2.2 X-ray reflectometry

In addition to the scattering by atoms in the crystal lattice, X-rays are also refracted at interfaces between layers [177] due to the changing electron densities. This effect can only be observed for comparatively small incidence angles ($< 10°$) where X-rays are evanescently coupled into the near-surface layer structure. XRR is capable of resolving very small layer thicknesses and interface roughnesses and was used here to analyze the properties for submonolayer stacks [178–181].[1]

Fig. 3.5a shows the comparison of XRR simulation performed assuming homogeneous InGaAs layers and 7x SML stacks of the same average thickness and composition. Using the submonolayer stack results in the appearance of additional peak groups around 3° and 6° incidence angle which reflect the internal periodicity of the SML stack. The intensity of these peaks is strongly dependent on the roughness of the individual layers. Using the same roughness parameter σ for all SML layers, an average internal roughness of the whole stack can be defined. As is depicted in Fig. 3.5b, the relative intensity of the SML peaks decreases with increasing σ. This can be used as a tool to monitor the development of disorder in the SML stack.

Care has to be taken when fitting such XRR scans. The periodicity of the SML stack is defined be the distance between InAs or GaAs sheets, meaning the sum of the average InAs and GaAs thickness. Simulations of SML stacks with identically total thicknesses but differing InAs/GaAs ratios yield therefore peaks at the same reflection angles but with differing peak intensities. Therefore, the average composition and thickness has to be determined from XRD measurements first before further analysis of the internal SML stack roughness.

Analysis was again performed using the tool xrayutilities.

Individual submonolayer islands cannot be analyzed by the presented XRD and XRR techniques as the primary beam size is several orders of magnitude larger. Consequently, another measurement technique like cross-sectional scanning tunneling microscopy (XSTM, section 3.2.4) is needed to gain information about the distribution of In and Sb on the nanometer scale.

[1] The measurements used in this thesis were performed by Dr. Jürgen Bläsing at the Otto-von-Guericke University in Magdeburg.

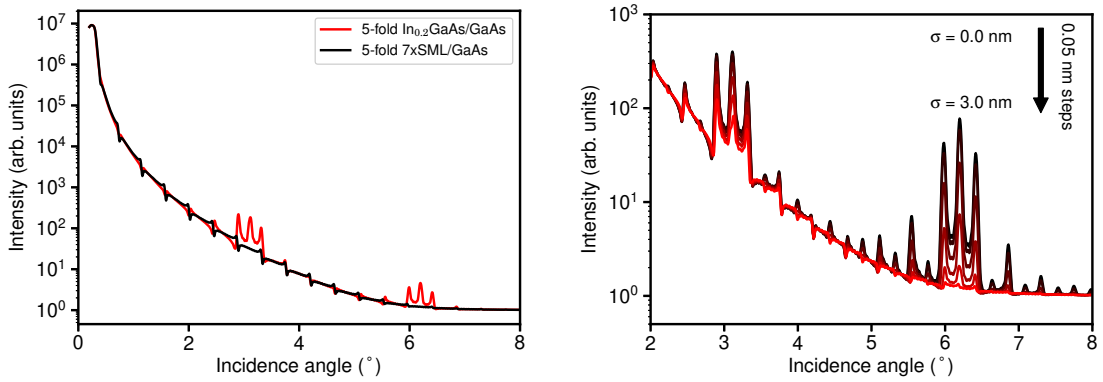

(a) **(b)**

Figure 3.5: Simulation of X-ray reflectivity scans. The assumed sample structures are identical on average (10 nm $In_{0.2}GaAs$ layers separated by 10 nm GaAs). (a) Influence of the internal SML structure (b) of the internal roughness.

3.2.3 Grazing-incidence X-ray fluorescence

X-ray fluorescence is based in the ionization of electrons from the inner shells of atoms. The resulting vacancies are then filled up again with electrons from higher shells. During this process characteristic X-rays are emitted. At large incidence angle, X-ray radiation has a large penetration depth (> 1 µm) into the semiconductor crystal. As the samples investigated here only have a total layer thickness of about 100 nm, the majority of fluorescence signal would originate from the substrate.

For small incidence angles close to the angle of total internal reflection for X-rays, however, the penetration depth is much lower and the fluorescence signal mainly originates from the near-surface epitaxial layers. Therefore, GIXRF measurements [182, 183] were performed[2] on the samples. For excitation, the Co-Kα line (1.79 Å or 6.93 keV) was used and the incidence angle for each sample was set to the first XRR superlattice fringe (about 0.5°, compare Fig. 3.5a) in order to ensure a defined positioning of the X-ray standing wave field.

As can be seen from the electronic structure of In and Sb shown in Fig. 3.6, the atomic transitions of both elements are energetically close to each other. Though the usual width of the atomic transitions lies in the range of about 10 eV [185], a distinction of individual emission lines is not possible due to the resolution of the measurement setup.

[2] Also by Dr. Jürgen Bläsing at the Otto-von-Guericke University in Magdeburg.

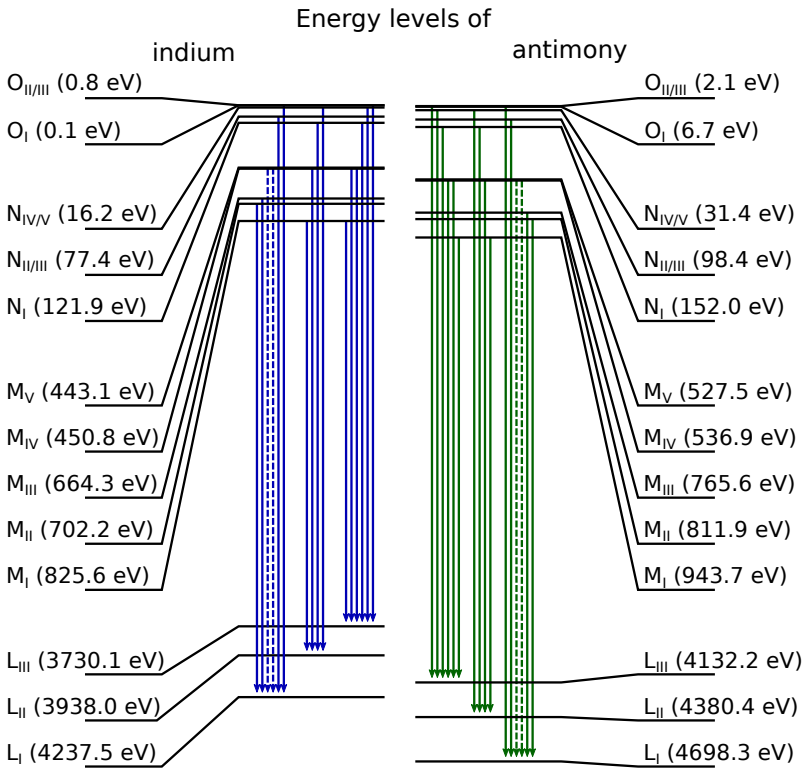

Figure 3.6: Electronic structure of In and Sb, drawn with data from [184]. Solid lines are allowed and dashed lines are forbidden transistions according to the quantum mechanical selection rules. K level is omitted for clarity.

Fig. 3.7 shows a typical GIXRF spectrum with indicators of different sources of X-ray fluorescence. All recorded peaks are significantly broader than the aforementioned linewidth. An estimation of the setup resolution can be gained by taking the brightest line in the energy region of In and Sb atoms (3 - 5 keV) which consist only of the In-Lα1 and -Lα2 lines [186] and fitting a double gaussian with fixed energetic positions and a shared width to it (not shown here). From such fit an FWHM of $\sim$110 meV was obtained which represents in a first approximation the setup resolution.

To determine the In/Sb ratio, the GIXRF signal needs to be separated into the In and Sb contributions. As will be described further in section 4.1.2, this can be achieved using reference samples.

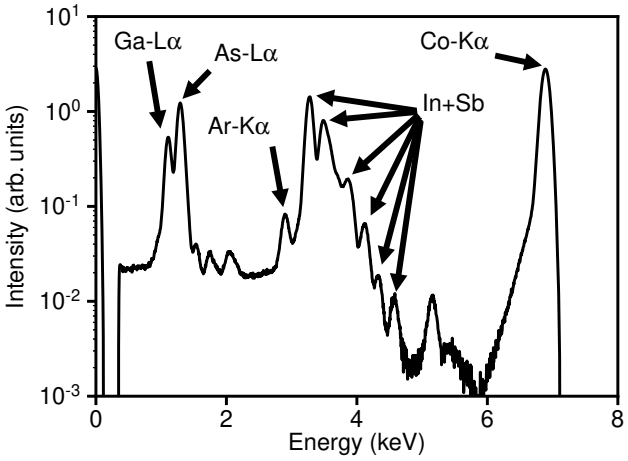

Figure 3.7: GIXRF spectrum obtained from a 5-fold superlattice consisting of 7x InAsSb/GaAs SML stacks separated by GaAs and a TESb supply of 27.92 µmol per flush.

3.2.4 Cross-sectional scanning tunneling microscopy

To map the local atom distribution of a given sample, XSTM measurements[3] can be performed. A fine tip is brought close to the (cleaved) sample surface. Between both, a tunneling current with an exponential dependence on the distance between tip and surface flows. Several mechanisms define the observed contrast.

Firstly, the polarity between tip and sample determines whether the group-III or the group-V sublattice is observed during a measurement. An image taken at positive sample voltage is called empty-state image as the electrons tunnel from the electron-filled tip into the empty states of the sample. Vice versa, in a measurement taken at negative sample voltage tunneling occurs from the filled sample states to the empty tip. This is called a filled-state image [187]. As the empty-states of a III-V semiconductor sample are located at the positions of the group-III atoms (dangling cation bonds) whereas the filled states are located at the group-V atoms, empty-state and filled-state images can be used to image the group-III and group-V sublattice, respectively [188].

The local band gap of the images sample yields a material contrast as the second influence. Materials with a lower band gap provide more states available for the tunneling process, thus appearing brighter in the recorded image [188].

[3]Performed by Zeno Diemer, Christopher Prohl, and Dr. Andrea Lenz at the TU Berlin.

Lastly, cleaving of a sample containing strained layer structures results in the structural relaxation by surface buckling. This is not only the case for a complete structure, e.g. a strained quantum well or quantum dot, but also for individual atoms, allowing for the determination of atom positions [188].

For XSTM measurements, the surface to be investigated is uncovered by cleaving. As steps can form at strained layers during this process, samples for this investigation usually contain the same layers multiple times to increase the chances of obtaining a clean and step-free surface at the regions of interest. Additionally the samples are thinned down to a thickness of about 100 µm prior to cleaving. Two dedicated samples comprised of several SML stacks samples were grown (Fig. 3.8). Additionally a thick GaAs cap layer to prevent the tip from slipping off the sample surface and an AlGaAs marker layer were grown on top of the SML stacks. Substrate and cap are doped to enable biasing of the sample.

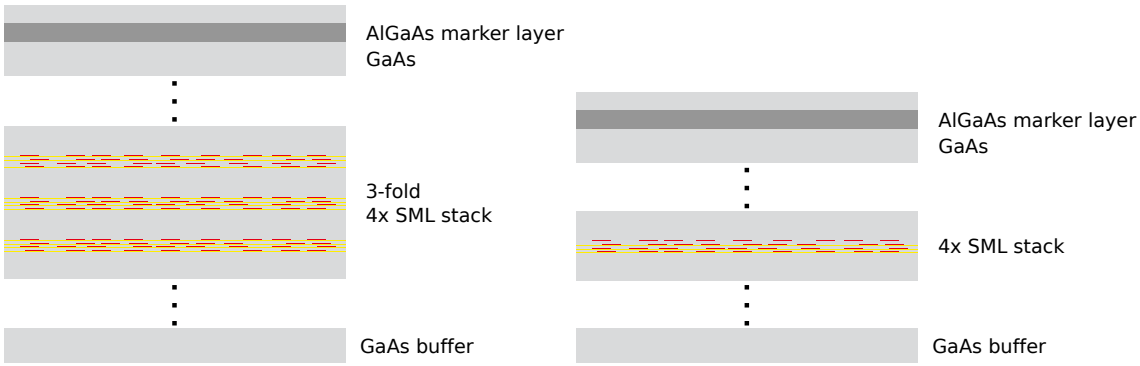

(a) First sample. **(b)** Second sample.

Figure 3.8: Sample structures for the XSTM measurements. Only the layers analyzed in this thesis are depicted.

3.2.5 Photoluminescence

The optical and electronic properties of semiconductors can be probed by spectroscopic techniques. Using light with a sufficiently large energy (usually larger than the largest band gap of the investigated material system), free charge carriers can be generated. Before recombining, these relax into the available states of lower energy which are defined by the material and structure of the investigated sample. As SML stacks are best described by a mixture of QW and QD states [85, 92, 94, 127], an analysis of recorded lineshapes needs to consider potential contributions from

all states present in the system. This is further explored in section 4.2.1. A more extensive overview of luminescence properties and measurements can be found in [189] and [190].

In this thesis, samples for photoluminescence (PL) measurements consist of a GaAs matrix with a single embedded SML stack as well as enclosing lower and upper AlGaAs diffusion barriers (Fig. 3.9).

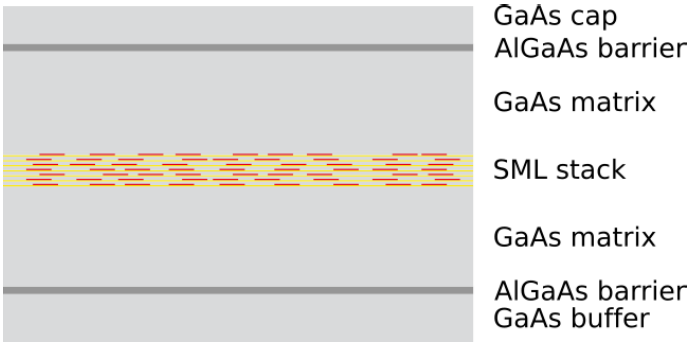

Figure 3.9: Sample structure for PL measurements.

The samples are either mounted on a metal heatsink for room temperature measurements or in a closed-cycle helium cryostat for temperature-dependent measurements down to ∼10 K. Optical excitation is done via a blue 440 nm (2.82 eV) laser diode or a green 532 nm (2.33 eV) DPSS laser, both being above the band gap of GaAs (1.52 eV at 0 K [96]). The light emitted from the sample is spectrally selected by a monochromator and detected by an InGaAs or a Si diode connected to a lock-in amplifier. All measurements are corrected with the system characteristics.

In addition to the setup resolution of about 0.5 nm, the excitation spot diameter is about 35 µm for both lasers, which corresponds to an area of 10^{-3} cm^2. This means that in samples with quantum dots a large number of them will be potentially excited. Even in samples with a low quantum dot density of 10^8 cm^{-2}, 10^5 quantum dots contribute to the luminescence signal. Thus, the appearance of single emission lines in the integral spectrum is highly unlikely. As the expected density in submonolayers is four orders of magnitude larger (10^{12} cm^{-2}, see section 2.3), even more localization centers are located in the area of the excitation spot and emit light. To resolve single lines, a technique with a better spatial resolution is needed. In this thesis, cathodoluminescence (CL) was employed (section 3.2.6).

3.2.6 Cathodoluminescence

Another method to excite the samples is the use of an electron beam. In contrast to photoluminescence, a vacuum environment is mandatory. The advantage of cathodoluminescence[4] is the small diameter of the excitation spot which lies in the region of 1 µm (depending on diffusion and energy transfer processes). The lateral resolution can be further enhanced by using a shadow mask, an electron-transparent metal film with small apertures ($\sim$ 100 - 200 nm). Thereby, the light emitting surface area is reduced and the lateral resolution is enhanced further. For the smallest holes, the emitting surface area is $\sim 3 \cdot 10^{-8}$ cm^2, thus drastically decreasing the number of localization centers contributing to the luminescence compared to PL measurements. A detailed description of the cathodoluminescence setup can be found in [191] and with additional information about the shadow masks in [192].

3.3 Laser fabrication and characterization

3.3.1 Processing of edge emitting lasers

Laser structures (see Fig. 3.10) were grown on Si-doped GaAs(001) wafers and consisted of a single SML stack which was embedded into the center of a 600 nm wide $Al_{0.15}GaAs$ waveguide. 2 µm thick n- and p-doped $Al_{0.25}GaAs$ layers were used for bottom and top cladding. A highly p-doped GaAs layer served as a current spreading layer.

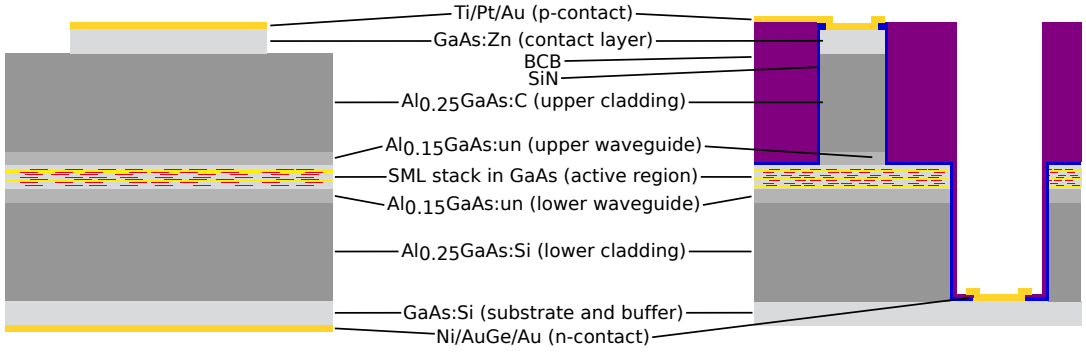

Figure 3.10: Schematic laser structures. (left) Broad area and (right) narrow stripe edge-emitters. The layer thicknesses and growth temperatures can be found in table 3.1

[4]The measurements in this thesis were performed by Manuel Gschrey and Dr. Sven Rodt at the TU Berlin.

Table 3.1: Growth parameters for the laser structures

Layer	thickness	material	growth temperature
contact layer	200 nm	GaAs:C	570° C
upper cladding	2000 nm	$Al_{0.25}$GaAs:C	615° C
upper waveguide	300 nm	$Al_{0.15}$GaAs:un	615° C
interlayer	6.5 nm	GaAs:un	520° C
SML stack	8.1 or 2.5 nm	InAs:un (+TESb flush)/GaAs:un	520° C
interlayer	6.5 nm	GaAs:un	700° C
lower waveguide	300 nm	$Al_{0.15}$GaAs:un	700° C
lower cladding	2000 nm	$Al_{0.25}$GaAs:Si	700° C
buffer layer	300 nm	GaAs:Si	700° C
substrate		GaAs:Si	

The fabrication of broad-area lasers was done using a wet chemical process as detailed below:

1. Definition of the top contact metalization area using a negative UV photoresist (100 µm ridge width)
2. Deposition of a Ti/Pt/Au top p-contact and lift-off
3. Definition of the laser ridges by removing the p-GaAs contact layer with a 1:8:100 H_2SO_4:H_2O_2:H_2O etching solution
4. Lapping of the sample backside to about 130 µm thickness
5. Deposition and annealing of a Ni/AuGe/Au backside n-contact
6. Cleaving into laser bars of the desired laser lengths

In contrast, the narrow-stripe lasers were fabricated by dry etching in an inductively coupled plasma reactive-ion etching (ICP-RIE) process:

1. Definition of the ridge area using positive UV photoresist
2. Etching of the ridge waveguides until about 300 nm above the active region (about 2.2 µm etch depth, 3.3 µm ridge width) using ICP-RIE
3. Deposition of 200 nm SiN

4. Opening of SiN areas next to the ridges for the n-contact metalization using a positive resist UV lithography and RIE etching
5. Etching of the n-contact area (about 2.8 µm etch depth) with ICP-RIE
6. Lithography with a negative UV photoresist for and deposition of Ni/AuGe/Au n-contact
7. Planarization using BCB
8. Removal of BCB and SiN from the top of the ridge waveguides
9. Deposition of Ti/Pt/Au metal stack for the p-contact
10. Removal of the BCB from the n-contact
11. Lapping of the sample backside to about 110 µm thickness
12. Cleaving into laser bars of desired laser lengths

3.3.2 Characterization of broad-area lasers

To extract the internal parameters as described in section 2.6, L-I measurements were performed on lasers with different lengths.

The laser bars were put on a copper heatsink which also provides the backside contact while the top contact is probed by needle contact probes. Lasers were driven in pulsed mode with pulses of 800 ns length and 1 kHz repetition frequency to avoid self-heating effects. The emitted light was collected by a optical multimeter directly placed in front of one facet. A more detailed description of the setup can be found in [193] and [194].

3.3.3 Characterization of narrow-stripe lasers

For the characterization of the narrow-stripe lasers, laser bars with a width (laser length) of 700 µm were mounted on a copper block which could be attached to the heatsink.

For gain measurements, both n- and p-contact were connected to a dc current source via needle probers and a tapered fiber attached to an optical spectrum analyzer (OSA) was used to record high-resolution spectra.

For dynamic measurements, needle probes were replaced by a high-frequency probe head. Additionally, the fiber was now attached to a single-mode 45 GHz photodetector and a vector network analyzer to measure small-signal response curves.

For large-signal operation, direct modulation signals with a non-return-to-zero pseudo-random binary sequence of 2^7-1 bit length were provided by a bit pattern generator. On the detection side, a custom made 28-GHz limiting photoreceiver was used in combination with a 80 GSa/s realtime oscilloscope for acquisition of eye diagrams and an error analyzer for the measurement of error ratios.

More in detail descriptions of the measurements and setups can be found in [157].

4 High density QD ensembles by Sb-assisted submonolayer growth

In the first part of this chapter, the influence of an TESb flush on structural, electronic and optical properties of InAs/GaAs submonolayer stacks is investigated. With the help of eight-band k·p simulations [93], yielding different extensions of the electron and hole wave functions, the way Sb atoms get incorporated was analyzed. The average incorporation of Sb was obtained from XRD and GIXRF measurements applying a model based on Langmuir-type adsorption [132, 133] to describe the incorporation behaviour. XRR and XSTM measurements allowed for the determination of microscopic changes introduced by the TESb flush and the position of Sb atoms relative to In-rich regions in the SML stack. Optical and electronic properties as presented in the second part were probed using low-temperature and temperature-dependent photoluminescence, as well as low-temperature cathodoluminescence measurements. Two existing lineshape models [195, 196] were combined to include 0D and 2D contributions as well as longitudinal optical (LO) phonon replicas in the analysis of low-temperature PL spectra. Three different tuning parameters (Sb supply, GaAs spacer between the InAs sheets, and number of deposition cycles i.e. total stack thickness) were investigated with respect to localization properties. The obtained knowledge was then used to specifically tune emission properties of the SML stacks as demonstrated in the last section.

4.1 Sb incorporation into InAs/GaAs-SML stacks

4.1.1 Electronic properties of SML stacks in the presence of Sb

As the basic structure of InAs/GaAs submonolayer stacks has previously been determined to be an InGaAs quantum well with regions of increased In content [85,

127], the simulation structure consisted of an 8.5 nm thick $In_{0.15}GaAs$ quantum well with spherical quantum dot regions with sinusoidal In composition profile. A peak In content of 35% was assumed as input for eight-band k·p simulations [93]. The spacing between quantum dot regions was 13.6 nm, giving a QD density of $5.4{\cdot}10^{11}$ cm^{-2}.

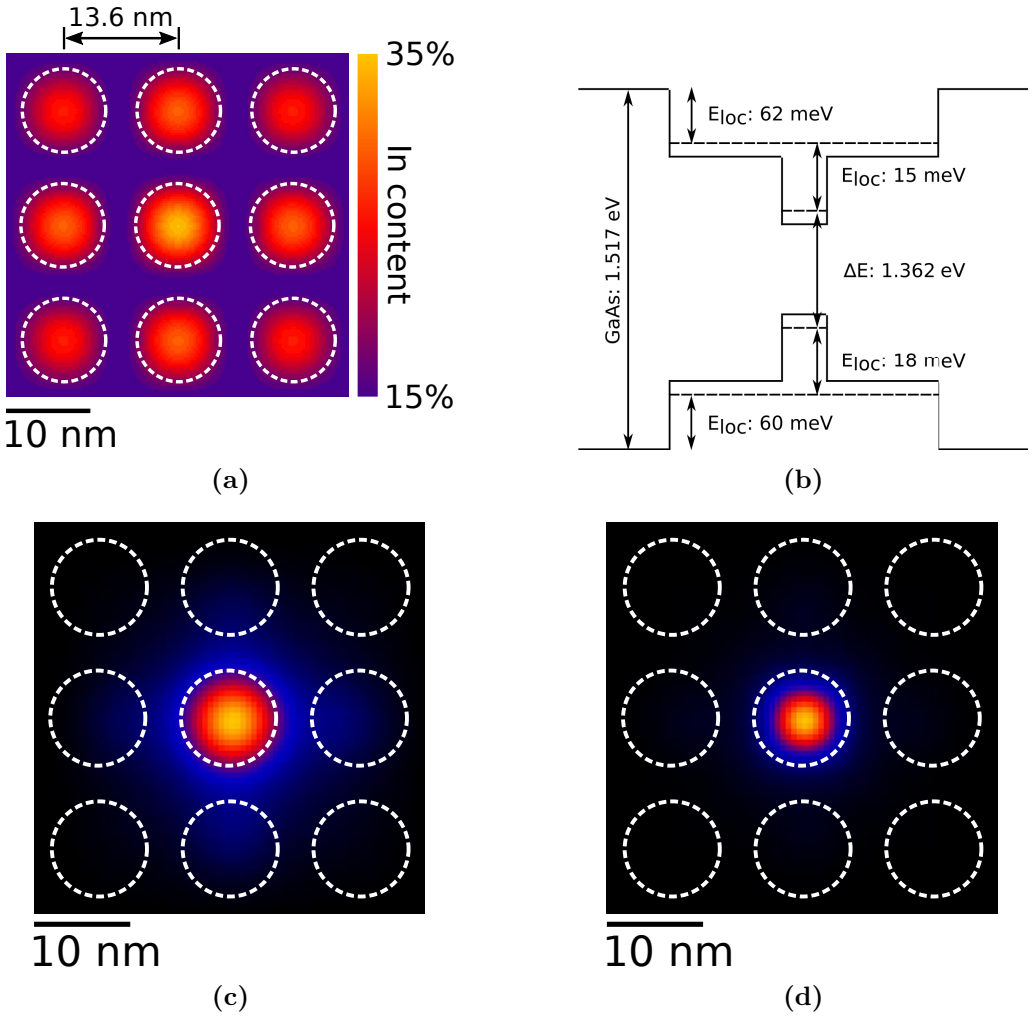

Figure 4.1: Settings and results of the simulation without Sb. Dashed white circles mark In-rich QD regions. (a) Assumed In distribution. (b) Schematic band alignment. (c) Electron wave function. (d) Hole wave function.

Additionally a gaussian composition profile was assumed over the whole simulation area, resulting in the central quantum dot region having the largest In content (see Fig. 4.1a), thus keeping the wave functions in the center of the simulation area. A schematic band alignment of the simulated structure is presented in Fig. 4.1b,

showing the ground states of electrons and holes in the $In_{0.15}GaAs$ QW with localization energies of 62 and 60 meV with respect to the surrounding GaAs bulk material. For electron and hole eigenstates in the quantum dot regions, energetic separations to the QW of 15 and 18 meV are found, respectively. The calculated transition energy is 1.362 eV.

Both wave functions are mainly localized in the central quantum dot region, with the electron wave function being more extended to adjacent quantum dot regions due to its smaller localization energy (Figs. 4.1c and 4.1d). This difference in localization was termed "heterodimensionality" in [94]. A Huang-Rhys factor of 0.005 could be calculated from the overlap integral of the wave functions.

Three Sb incorporation behaviors are conceivable:

- Incorporation preferentially at In-rich regions
- Incorporation preferentially between In-rich regions
- Homogeneous distribution throughout the SML stack

All three options were considered through the eight-band k·p simulations theoretically by varying the local Sb content in steps of 5%. Possible influences on the basic structure, e.g. growth rate variations leading to varying layer thicknesses or modified atom surface mobilities resulting in different quantum dot dimensions were not taken into consideration.

Sb incorporation into QDs

Sb incorporation into QD regions (Fig. 4.2a) leads to shift of the local conduction band edge to larger energies, thereby decreasing the offset between the electronic eigenstate of the QD region and the surrounding quantum well. The local valence band edge is also shifted to larger energies, leading to an increased offset (Fig. 4.2b). For the largest simulated local Sb content of 20%, the localization energy for electrons is decreased from 15 meV to 6 meV while it is increased from 18 to 154 meV for holes. Consequently the electron wave function delocalizes from the central quantum dot and extends over a larger area (Fig. 4.2c). Simultaneously the hole wave function is stronger localized as compared to the case without Sb (Fig. 4.2d). A redshift of the emission is to be expected due to the reduction of transition energy by 127 meV to 1.235 eV. Finally, the decreased wave function overlap results in an increase of the dipole moment and increases the Huang-Rhys factor to 0.076.

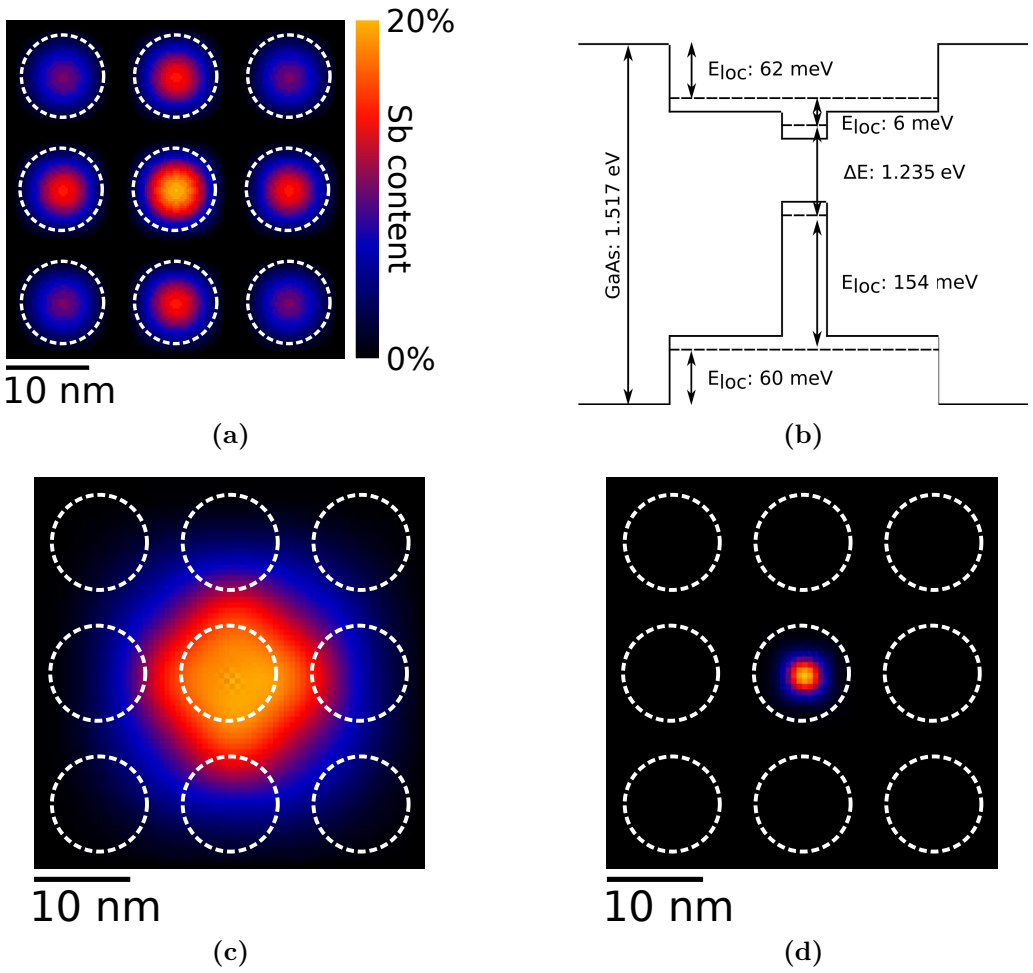

Figure 4.2: Settings and results of the simulation with Sb incorporated into QD regions (marked by dashed white circles). (a) Assumed Sb distribution and (b) schematic band alignment. (c) Electron and (d) hole wave function.

Sb incorporation outside QDs

The second possibility is a preferential incorporation of Sb between QD regions (see Fig. 4.3a) which would lead to formation of additional potential steps in the quantum well (Fig. 4.3b) with a hole localization energy of 114 meV. As this is significantly larger than the 18 meV of the central quantum dot region (compare Fig. 4.1b), the hole wave function delocalizes from the QD region to the new potential steps (Fig. 4.3d). As the electron wave function is still located in the central quantum dot, the overall band alignment changes to a type-II arrangement. As in the previous incorporation case, a redshift would be expected as the transition energy decreases to 1.268 eV at 20% local Sb content. An increase of the dipole

moment and the Huang-Rhys factor to 0.018 is found here.

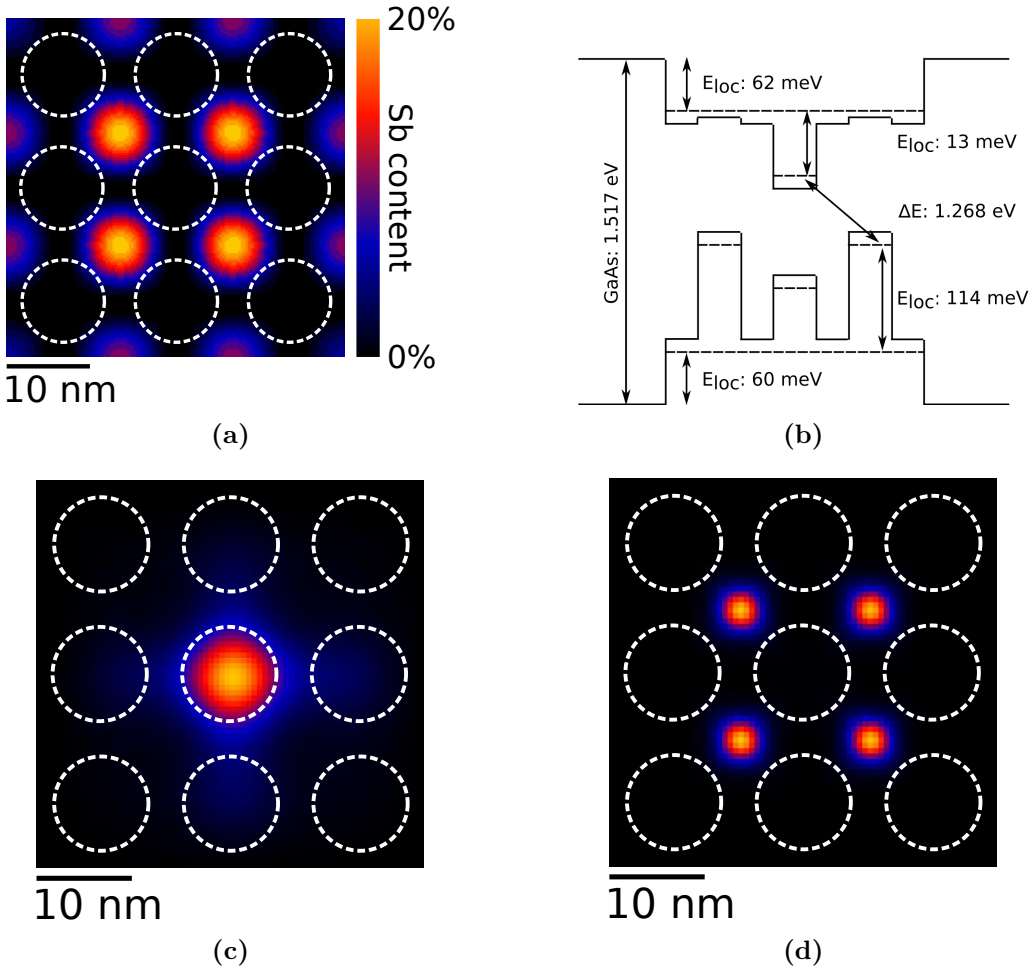

Figure 4.3: Settings and results of the simulation with Sb incorporated between QD regions (dashed white circles) (a) Assumed Sb distribution. (b) Schematic band alignment. Wave function of (c) electrons and (d) holes.

Homogeneous incorporation into the SML stack

The last possibility of Sb incorporation is a distribution without preference with respect to the QD regions in the SML stack. Here, the simulation was only performed until 10% Sb content as the quantum well forms a type-II band alignment with respect to GaAs for larger Sb contents. In this configuration, both the local conduction and the valence band are shifted to larger energies with respect to the surrounding barrier material (Fig. 4.4a). Consequently the extension of the wave functions remains nearly unchanged, aside from a slight delocalization of the

hole wave function (Figs. 4.4b and 4.4c). This incorporation scheme yields the largest redshift of 140 meV at only 10% Sb content. The increased overlap of the wave functions leads to a nearly vanishing dipole moment and Huang-Rhys factor of 0.001.

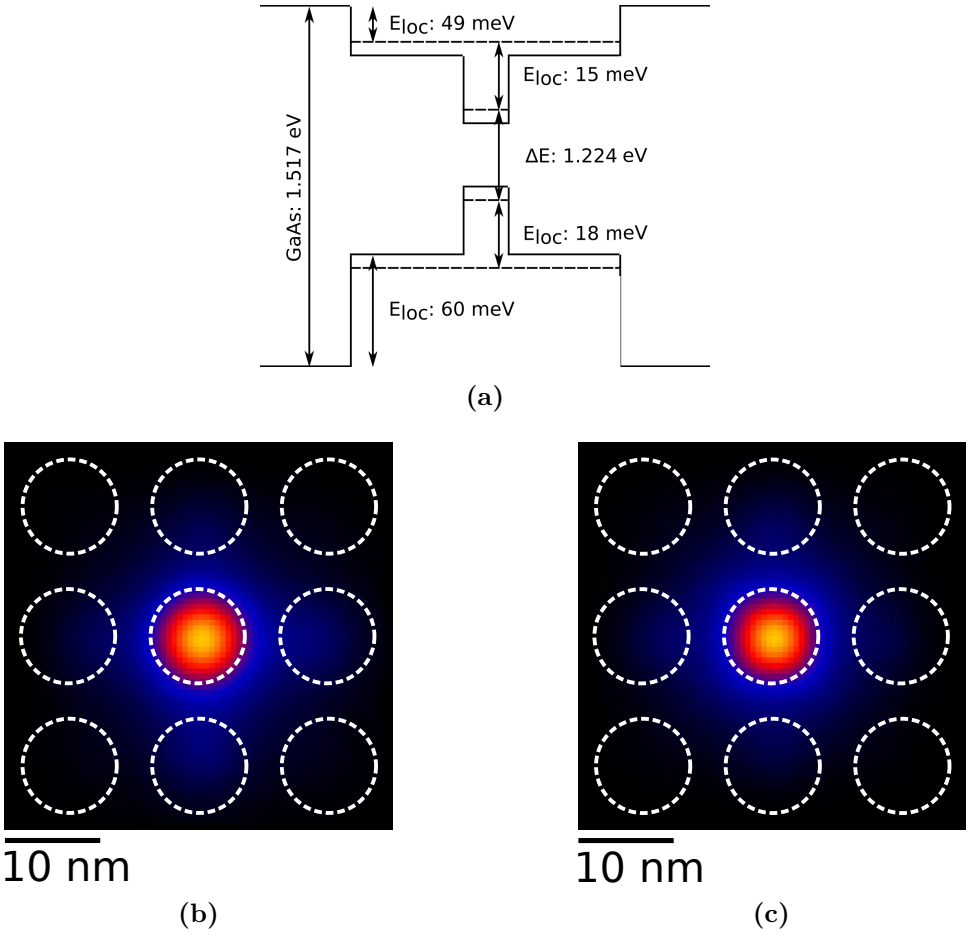

Figure 4.4: Results of the simulation with Sb evenly incorporated throughout the SML stack. Dashed white circles mark the QD regions as defined by In-rich regions. (a) Schematic band alignment. (b) Electron wave function. (c) Hole wave function.

In conclusion, while all three incorporation schemes lead to a redshift of the emission, the effects on the charge carrier wave functions differ significantly. Which of the three cases is present when using an TESb flush prior to the InAs deposition was be determined experimentally by examination of the structural and optical properties (see sections 4.1.3 and 4.2). The transition energies and Huang-Rhys factors for all simulated Sb contents are summarized in Fig. 4.5.

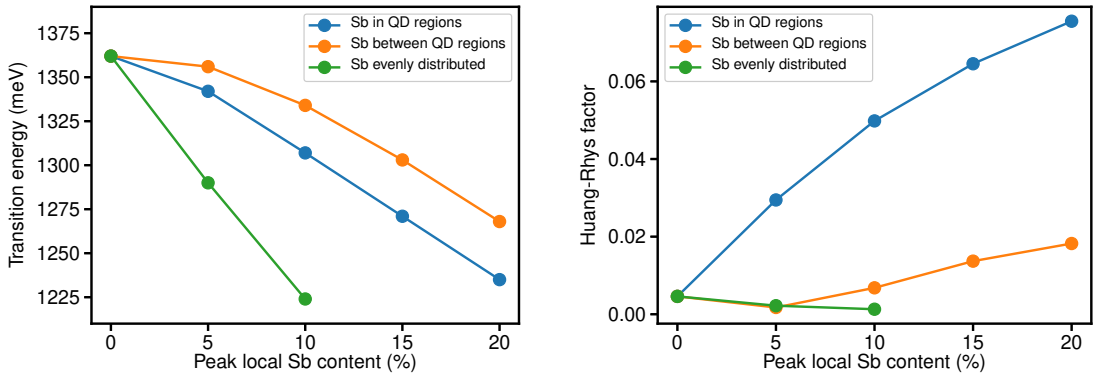

(a) **(b)**

Figure 4.5: (a) Transition energies and (b) Huang-Rhys factor as obtained from eight-band k·p simulations for the three incorporation schemes.

4.1.2 Determination of the average Sb incorporation

5-fold superlattices containing 7x InAs/GaAs SML stacks grown with increasing TESb supplies and separated by GaAs spacers were investigated to determine the average composition. XRD scans in $\omega - 2\Theta$ geometry around the GaAs(004) peak yielded the total thickness of the SML stack and the In+Sb composition. In superlattices with otherwise identical growth parameters, an addition of TESb results in a reduced thickness of the SML stack. This growth rate reduction is further adressed in section 4.1.3.

Two sample series using different approaches to control the Sb amount were investigated. In the first one, the TESb flush time was held constant at 3 s, while the molar flow rate was varied between 0.44 µmol/min and 8.72 µmol/min, corresponding to $6.5{\cdot}10^{-5}$ to $1.3{\cdot}10^{-3}$ mbar partial pressure or a total TESb supply of 0.02 to 0.44 µmol. For the second approach, the TESb partial pressure in the reactor was held constant at $1.3{\cdot}10^{-3}$ mbar, whereas the flush time was varied between 6 and 192 s, yielding a total TESb supply of 0.87 to 27.92 µmol. A reference sample without Sb was grown for each sample series. The resulting XRD data can be fitted assuming a 5-fold InGaAs/GaAs superlattice (see Fig. 4.6) with one InGaAs layer representing one 7x SML stack. To separate the determined average composition into In and Sb-related contents, the In/Sb ratio needs to be determined.

For this, GIXRF measurements were performed on the samples. The incidence angle was set to the first superlattice fringe (located at about 0.5°) appearing in XRR

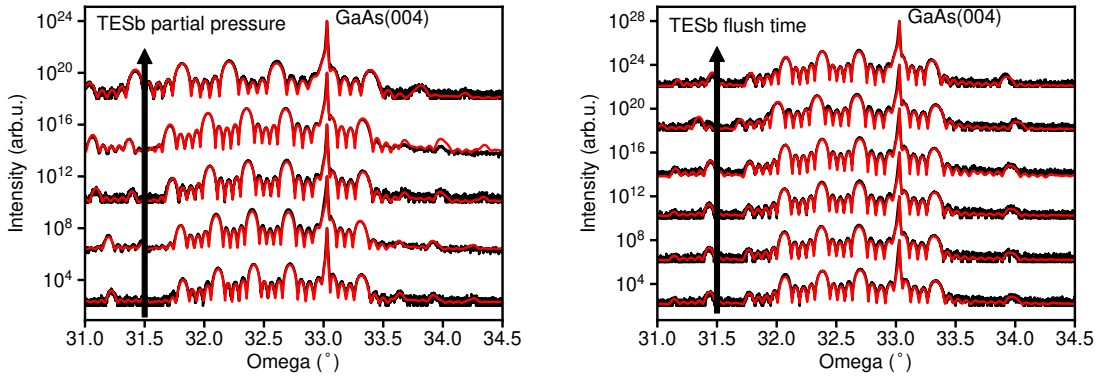

(a) **(b)**

Figure 4.6: XRD scans (black lines) and simulations (red lines). (a) Variation of the partial pressure from 6.5·10⁻5 to 1.3·10⁻3 mbar during a constant TESb flush time of 3 s. (b) Adjustment of the TESb supply by varying the flush time from 6 to 192 s at a constant partial pressure of 1.3·10⁻3 mbar. The shift of the satellite peaks to smaller angles in (a) is due to a growth rate reduction upon TESb addition. It has been compensated in (b) by adjusting the GaAs growth time accordingly. The measurements are vertically shifted to improve visibility.

measurements for each sample to ensure a defined position of the standing wave field. As shown in Fig. 4.7a, the resulting data was normalized to the brightest In peak at ∼3.28 keV, consisting of the In-Lα_1 line (3.28694 keV) and In-Lα_2 line (3.27929 keV) [186]. To separate the signals into In and Sb contributions, the fluorescence from the respective InAs/GaAs reference sample was subtracted from the measurements of the Sb-containing samples (Fig. 4.7b). To ensure that the resulting data contains information from Sb only, a further comparison to the signal from a GaSb sample (blue dashed line in Fig. 4.7b) was made. Finally, by integrating the data between 3.59532 and 4.2367 keV (lowest Sb and highest In-related emission lines), taking into account the about 10% larger photoabsorption cross section of Sb for Co-Kα excitation (In: $6.43{\cdot}10^4$ barns/atom, Sb: $7.23{\cdot}10^4$ barns/atom [197]), the In/Sb ratio was obtained by comparison with the integrated intensities of the reference samples of known stoichiometry. As the considered signals are energetically close to each other, the system characteristic (detector, window transmission etc.) was assumed to be constant. A maximum Sb incorporation of 5.8% is found for the used parameter set (see Fig. 4.8).

In order to further analyze the incorporation behavior of Sb into the SML stacks,

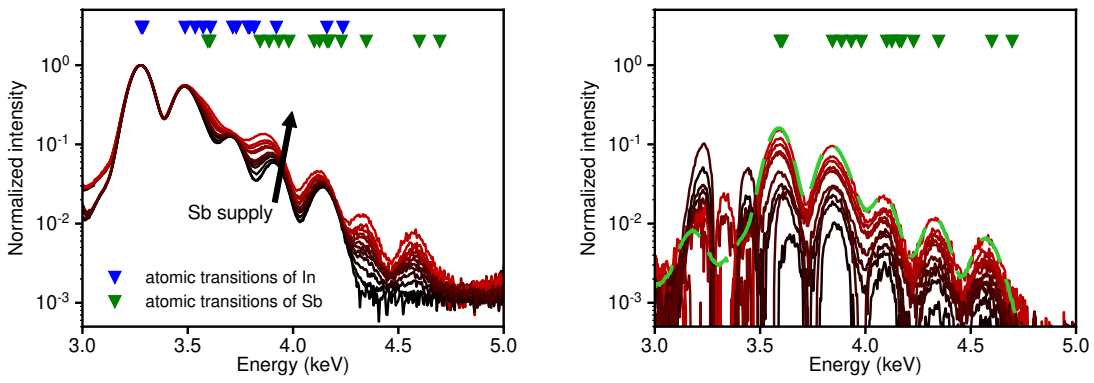

Figure 4.7: Results from the GIXRF measurements with In and Sb transitions marked in blue and green, respectively. (a) Normalized signals from both sample series. (b) Calculated Sb related signal. The blue dashed line is the signal from a GaSb sample.

adsorption models were employed. For this, the average number of incorporated Sb atoms was calculated from measured Sb content, stack thickness and number of deposition cycles for a base area of one square cm. Neglecting desorption processes during growth the number of incorporated atoms was assumed to be identical to the number of atoms adsorbed on the wafer surface after the flush. Using the atom density of the GaAs(001) surface ($6.26 \cdot 10^{14}$ cm^{-2}), a maximum Sb surface coverage of 23% was determined, corresponding to a surface density of $1.47 \cdot 10^{14}$ cm^{-2} (see Fig. 4.9b). Therefore multilayer adsorption models (e.g. the BET model [198]) were not considered and the behavior was modeled using a Langmuir-type adsorption model (see section 2.5).

In the "constant-flush-time" sample series (Fig. 4.9a), the amount of incorporated Sb atoms saturates at around $6 \cdot 10^{13}$ cm^{-2} atoms or 10% surface coverage while the number of Sb atoms increases slowly for the "constant-TESb-supply" sample series without showing saturation. Fitting the analytical equation of a simple Langmuir adsorption process (equation 2.11) to the data obtained from "constant-flush-time" samples yields a reasonably good fit. At longer flush times however, no agreement between the calculated data and the model fit could be obtained.

Using the model with a reaction component (equation 2.16) resulted in a very similar fit for "constant-flush-time" samples and yielded a slightly better fit to the data from "constant-TESb-supply" samples as it allows for the incorporation of the

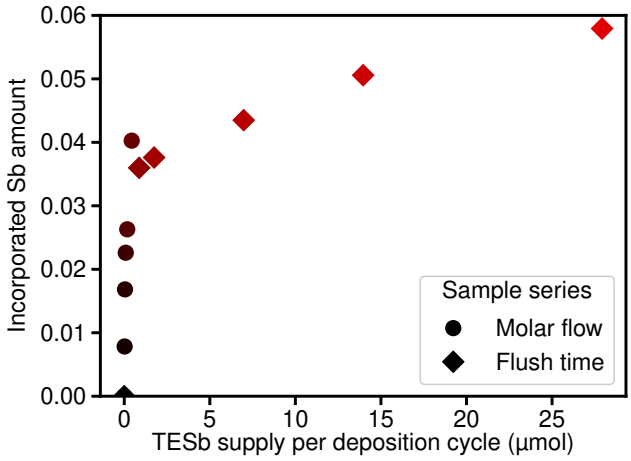

Figure 4.8: Extracted Sb content.

offset between both sample series via the reaction time component. However, it still fails to account for the slow increase of incorporated Sb atoms with flush time.

Therefore the model was extended with a second reaction component. The total number of sites is then described by

$$\begin{aligned} n_{total} &= n_{fast} + n_{slow} && (4.1)\\ &= n_{free,\ fast} + n_{TESb,\ fast} + n_{Sb,\ fast} \\ &\quad + n_{free,\ slow} + n_{TESb,\ slow} + n_{Sb,\ slow} && (4.2) \end{aligned}$$

This leads to the rate equations fast

$$\begin{aligned} \frac{dn_{free,\ fast}}{dt} &= -n_{free,\ fast} \cdot P_{TESb} \cdot k_{ads} \\ &\quad + n_{TESb,\ fast} \cdot k_{des} && (4.3)\\ \frac{dn_{TESb,\ fast}}{dt} &= n_{free,\ fast} \cdot P_{TESb} \cdot k_{ads} \\ &\quad - n_{TESb,\ fast} \cdot k_{des} - k_{r,\ fast} \cdot n_{TESb,\ fast} && (4.4)\\ \frac{dn_{Sb,\ fast}}{dt} &= k_{r,\ fast} \cdot n_{TESb,\ fast} && (4.5) \end{aligned}$$

and the slow component

$$\frac{dn_{free,\ slow}}{dt} = -n_{free,\ slow} \cdot P_{TESb} \cdot k_{ads} + n_{TESb,\ slow} \cdot k_{des} \tag{4.6}$$

$$\frac{dn_{TESb,\ slow}}{dt} = n_{free,\ slow} \cdot P_{TESb} \cdot k_{ads} - n_{TESb,\ slow} \cdot k_{des} - k_{r,\ slow} \cdot n_{TESb,\ slow} \tag{4.7}$$

$$\frac{dn_{Sb,\ slow}}{dt} = k_{r,\ slow} \cdot n_{TESb,\ slow} \tag{4.8}$$

Note that the adsorption constant was taken as identical for the fast and the slow case. This is justified assuming reaction components are occurring during the InAs and GaAs growth. Thus the adsorbed atoms show the same behavior. Then, the analytical solution is given by

$$n_{Sb} = n_{fast} \cdot (1 - \exp(-k_{r,\ fast} \cdot \Theta \cdot t)) + (n_{total} - n_{fast}) \cdot (1 - \exp(-k_{r,\ slow} \cdot \Theta \cdot t)) \tag{4.9}$$

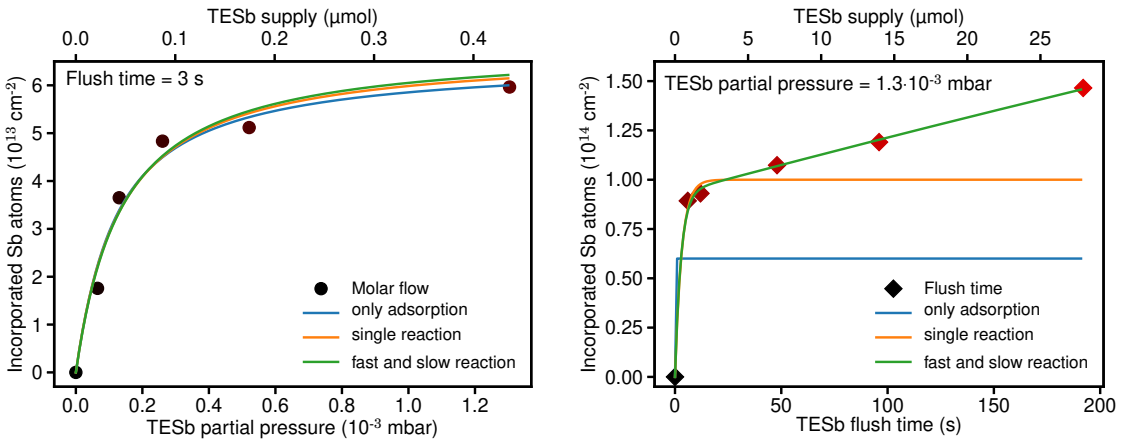

(a) **(b)**

Figure 4.9: Incorporated Sb atoms with respect to the varied growth parameter. Solid lines are fits to the respective Langmuir-type adsorption model. (a) Variation of the TESb molar flow at a constant flush time. (b) Variation of the TESb flush time at a constant molar flow.

A simultaneous fit of both the short and long term behavior was now possible,

accounting for the saturating behavior of the samples with constant flush time and the slow increase of the samples with constant partial pressure (Fig. 4.9). In the fitting of the model to the experimental data, the parameter n_{total} can be treated in two different ways. The first way takes n_{total} as a free parameter, which leads to the fitting parameters in the left column of table 4.1. As no saturation of the incorporated Sb atoms is experimentally observed, this leads to very large errors for $k_{r,slow}$ and n_{total}. Alternatively, assuming formation of a single monolayer of Sb only at maximum coverage, e.g. a surface coverage of 100 %, where n_{total} equals the atom density of the GaAs(001) surface ($6.26 \cdot 10^{14}$ cm^{-2}) the fitting parameters in the right column of table 4.1 were obtained.

Table 4.1: Results from fitting the adsorption model

	Results	
Fit parameter	n_{total} free	n_{total} fixed
K	(4052 ± 809) mbar^{-1}	(4024 ± 784) mbar^{-1}
$k_{r,fast}$	(0.42 ± 0.05) s^{-}1	(0.43 ± 0.05) s^{-}1
$k_{r,slow}$	$(5.3 \pm 357.7) \cdot 10^{-5}$ s^{-}1	$(6.5 \pm 0.6) \cdot 10^{-4}$ s^{-}1
n_{fast}	$(9.3 \pm 0.4) \cdot 10^{13}$ cm^{-2}	$(9.3 \pm 0.2) \cdot 10^{13}$ cm^{-2}
n_{total}	$(6.2 \pm 411.4) \cdot 10^{15}$ cm^{-2}	

While the results for the slow reaction constant differ significantly, depending on the fitting method, they are not contradictory. In both cases the fast and slow reaction constants differ by several orders of magnitude (a factor of 8400 with free and a factor of 662 with fixed n_{total}). The fast process must be directly connected to the TESb supply, since the region of low Sb supply can also be fitted with the simpler models, whereas the slow process could be rooted in a parasitic saturation effect at reactor walls. Therefore, short flush times are necessary in order to avoid these parasitic effects. This would, however, also limit the maximum amount of incorporated Sb.

With the developed model, the Sb amount in a given sample can be extrapolated from its growth parameters, as long as the In+Sb content and the total SML stack thickness are known. For a different sets of growth parameters (e.g. growth temperatures, molar flow rates, reactor pressures etc.), a recalibration of the model may be necessary.

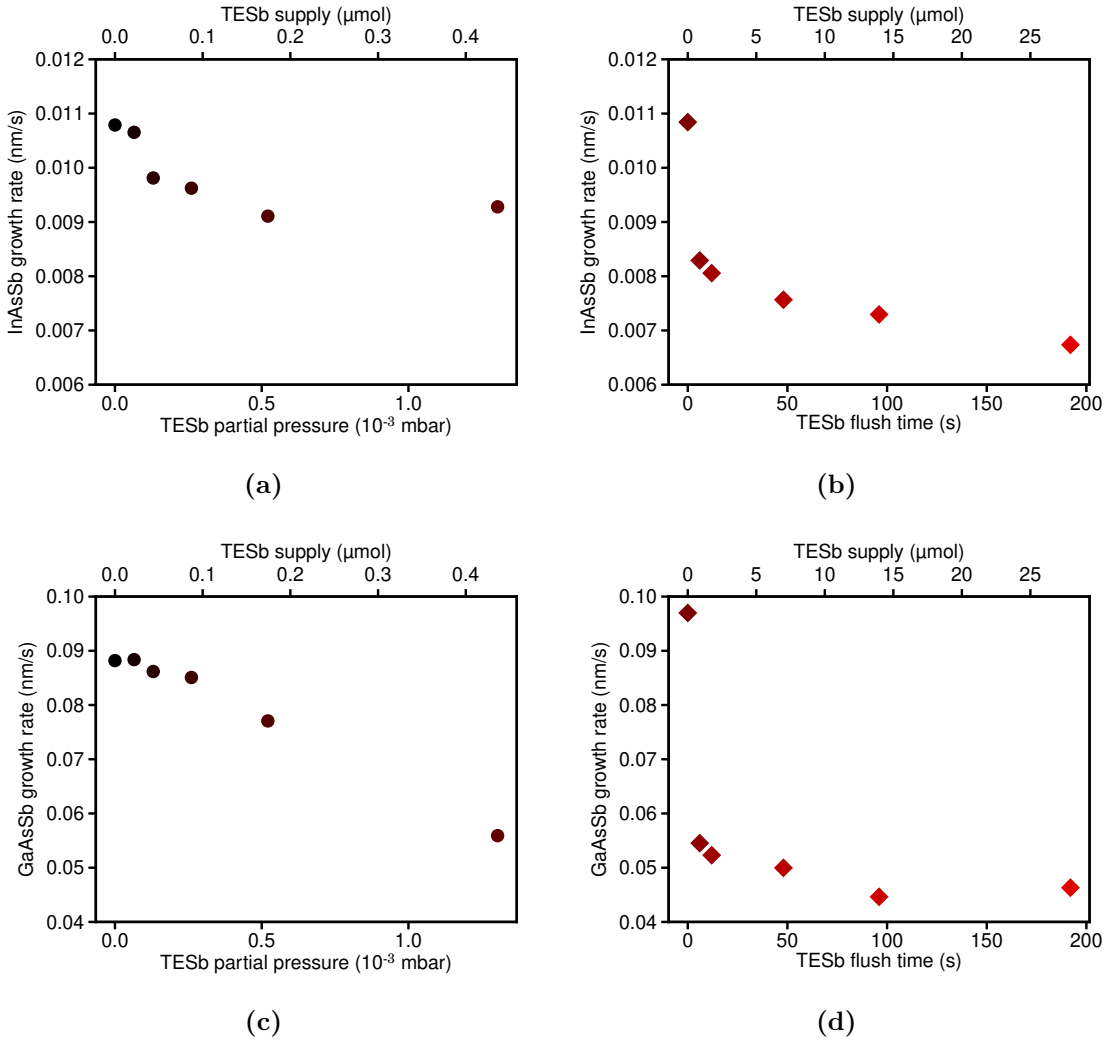

Figure 4.10: Evolution of the SML growth rates with the Sb supply for both sample series. (a) InAsSb and (c) GaAsSb growth rate vs TESb partial pressure. (b) InAsSb and (d) GaAsSb growth rate vs flush time.

4.1.3 Structural changes and local Sb distribution

As previously mentioned in section 4.1.2, the total thickness of InAs/GaAs SML stacks decreases upon the introduction of a TESb flush. Using thicknesses, In+Sb composition, and In/Sb ratio as previously obtained from XRD and GIXRF measurements, the average InAsSb and GaAsSb growth rate can be calculated. In the sample series with low TESb supply, i.e. "constant-flush-time", the InAsSb growth rate was reduced by approximately 14% (from 0.011 nm/s to 0.009 nm/s) while the GaAsSb growth rate was reduced by about 37% (to 0.056 nm/s from 0.088 nm/s). Although TESb was supplied prior to InAs deposition, the effect on the growth rate was more pronounced for the GaAs deposition. The "constant-TESb-supply" sample series showed the growth rate reductions equalize at large supplies. Here the InAsSb growth rate was reduced from 0.011 nm/s to 0.007 nm/s (about 48%) whereas the the GaAsSb growth rate was reduced from 0.097 nm/s to 0.046 nm/s, i.e. by 52%.

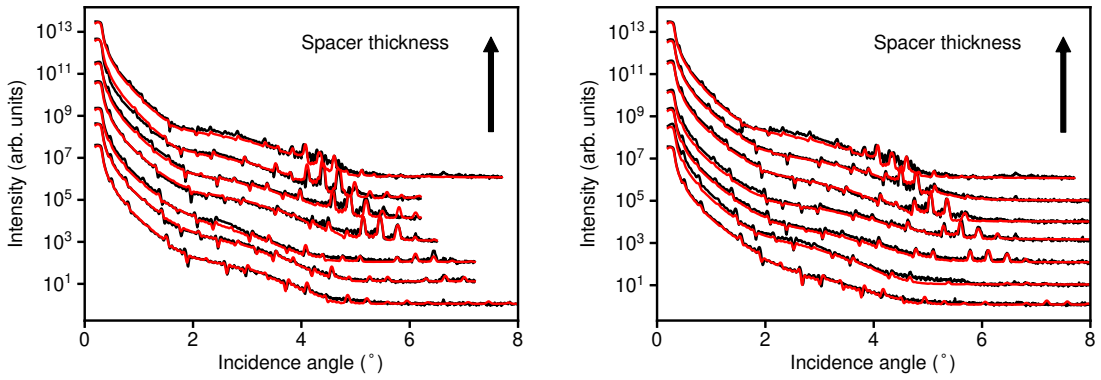

(a) (b)

Figure 4.11: XRR scans (black) and fits (red) for the sample series with varying GaAs spacer. The topmost measurement is obtained from the reference sample without TESb supply. (a) 6.98 and (b) 13.96 µmol TESb supply. Scans are vertically shifted for clarity.

As all XRD measurements can be fitted assuming a homogeneous InGaAs layer instead of the actual SML stack, no indications of structural changes apart from the growth rate reduction could be deduced, even for the highest amount of TESb supply. To gain more insight, XRR was used as it is sensitive to interface roughness. As the vertical structural coupling of the InAsSb islands is controlled by the spacer thickness between them, two sample series were fabricated. The layer structure is the same as before with a 5-fold superlattice containing 7x InAs/GaAs SML stacks

separated by GaAs spacers. Starting from an InAs/GaAs reference sample, two TESb supply levels (6.98 and 13.96 µmol) were investigated. In each sample series, the spacer growth time was varied from 10 s to 20 s in steps of 2 s.[1] Figs. 4.11a and 4.11b show the obtained XRR scans with their respective fits from both sample series.

A group of distinct peaks appears between 4° and 5° incidence angle in the reference sample and shifts to larger angles as the spacer thickness decreases. For samples with short spacer growth times, these peaks disappear. They can be attributed to the internal SML structure (compare Fig. 3.5a).

Moreover, a number of small peaks is found over almost the whole measurement range, reflecting the average 5-fold InGaAs/GaAs superlattice.

Lastly, a very broad peak ranging from about 2° to 4° incidence angle is overlaid with the previous signals, stemming from a thin ($\sim$ 1 nm) oxide layer on top of each sample.

Table 4.2: Results from XRR fits

TESb supply (µmol)	growth time (s)	Spacer thickness (nm)	roughness (nm)
0	10	0.88 ± 0.11	0.25
6.98	10	0.44 ± 0.11	0.25
6.98	12	0.50 ± 0.11	0.25
6.98	14	0.56 ± 0.11	0.25
6.98	16	0.65 ± 0.08	0.22
6.98	18	0.77 ± 0.06	0.25
6.98	20	0.83 ± 0.11	0.20
13.96	10	0.44 ± 0.11	0.23
13.96	12	0.48 ± 0.08	0.26
13.96	14	0.54 ± 0.08	0.21
13.96	16	0.59 ± 0.08	0.20
13.96	18	0.68 ± 0.08	0.23
13.96	20	0.77 ± 0.08	0.25

To fit XRR scans, XRD measurements were performed first to obtain the average thickness of the single InAs and GaAs sheets. The results were then used in the

[1] For an analysis of the optical properties, PL samples with the same growth parameters but containing only a single SML stack were grown as well (see section 4.2.3).

simulation of the XRR scans. For spacer thicknesses below 1.75 ML the signals originating from the SML stack were not resolved anymore. However, simulations yielded a nearly constant roughness of 0.20 - 0.26 for all samples. The disappearance of the SML-related peaks is caused by the limited dynamic range of the measurement setup at larger angles. Additionally local structural changes may not be resolvable by this technique due to its spatially averaging nature.

Local In and Sb distribution

For the determination of the local In and Sb distribution, a 3-fold 4x InAs/GaAs SML stack with 13.96 µmol TESb supply and a single 4x InAs/GaAs SML stack with the same TESb supply were investigated by XSTM.

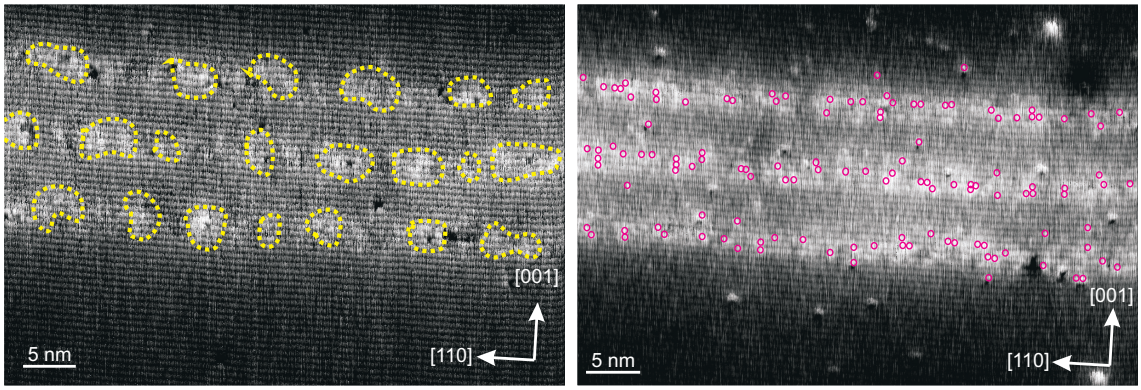

(a) **(b)**

Figure 4.12: XSTM images of a 3-fold 4x InAs/GaAs SML stack with 13.96 µmol TESb supply. (a) Empty-state image, taken at a sample voltage of +2.4 V and a tunneling current of 40 pA. In-rich regions are highlighted by yellow dotted lines. (b) Empty-state image, taken at a sample voltage of -1.8 V and a tunneling current of 40 pA. Single Sb atoms are marked as pink solid circles.

Empty-state images of the 3-fold superlattice reveal In-rich regions with a width of about 3.4 nm and 2×10^{12} cm^{-2} areal density (Fig. 4.12a). InAs/GaAs SMLs have previously shown In-rich regions with a width of around 5 nm at the same density [85]. Analyzing the local lattice constant, a segregation coefficient of 0.68 ± 0.05 was found for SML grown with TESb supply, as opposed to 0.75 ± 0.07 without TESb [84, 85]. The positions of incorporated Sb atoms can be determined by analyzing filled-state images (Fig. 4.12b). Here, a slight clustering tendency was seen, thus disfavoring an even Sb incorporation throughout the SML stack.

For determination of the Sb atom position with respect to the In-rich regions, a filled- and an empty-state image of the single 4x SML stack were taken. The position of the Sb atoms was determined from the empty-state image and then overlaid with the filled-state image. This revealed Sb atoms are preferably incorporated in or at the border of the In-rich regions (Fig. 4.13). Therefore, addition of TESb should not change the type-I band alignment of the InAs/GaAs SMLs.

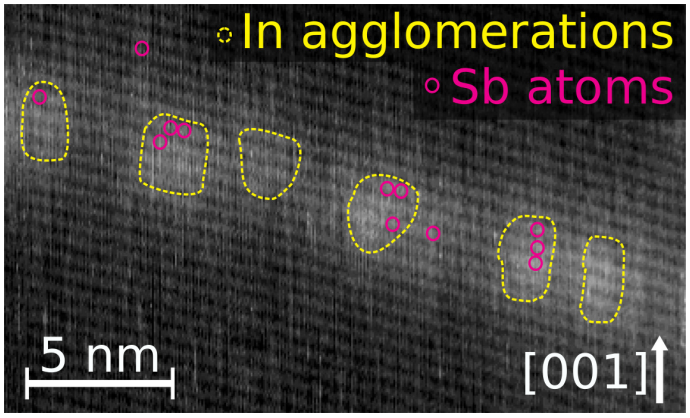

Figure 4.13: Empty-state XSTM image, taken at +2.5 V sample voltage and 40 pA tunneling current. In-rich regions are marked by yellow dotted lines. The positions of Sb atoms (red circles) have been determined from an filled-state image taken at the same sample position with -2.2 V sample voltage and 40 pA tunneling current.

4.2 Analysis of charge carrier localization

4.2.1 Analysis of photoluminescence measurements

Lineshape

Photoluminescence spectroscopy was used to analyze the optical and electronic properties of the SML stacks. As detailed in [127], the PL lineshape of SML stacks can be modeled assuming a quantum well structure with localization centers, e.g. interface roughnesses and compositional fluctuations. A model comprising contributions from both free charge carriers and excitons was presented by Christen [191, 196]. Since statistical broadening was assumed to be large in comparison to intrinsic lifetime broadening, the latter one was neglected. The luminescence lineshape is then given

by

$$I = \underbrace{I_{2D} \cdot \mathrm{erfc}\left(\frac{E_g - E}{\sqrt{2}\sigma}\right) \cdot \exp\left(\frac{E_g - E}{k \cdot T}\right)}_{\text{free charge carriers}} + \underbrace{I_{0D} \cdot \frac{1}{\sqrt{2\pi}\sigma}\left(\frac{(E_g - E)^2}{-2\sigma}\right)}_{\text{excitons}} \tag{4.10}$$

E_g is the average energy gap of the SML stack, I_{2D} is the maximum amplitude of the 2D contribution term, I_{0D} is the maximum amplitude of the 0D contribution, σ is the broadening term which includes compositional and thickness fluctuations, k is the Boltzmann constant and T is the lattice temperature.

While such model accounts for the high-energy tail of the emission, the low energy tail is not well accounted for. An extension of the model above is possible with an excitonic lineshape as given by Schubert and Tsang [195] which describes the relaxation of charge carriers into states of lower energy by a first-order partial differential equation

$$\frac{dn(E,T)}{dt} = -\int_{-\infty}^{E} \frac{1}{\sqrt{2\pi}\sigma}\left(\frac{(E - E_g)^2}{-2\sigma}\right) dE \frac{1}{\tau_c} n(E,t) \tag{4.11}$$

where τ_c is a time constant for relaxation of charge carriers into energy minima. With this, the excitonic lineshape can be written as

$$\begin{aligned} I =& I_0 \cdot \exp\left(-\frac{1}{2}\left(\frac{E - Eg}{\sigma}\right)^2\right) \\ & \times \exp\left(-\frac{\tau_r}{\tau_c}\frac{1}{\sqrt{2\pi}\sigma}\int_{-\infty}^{E}\left(-\frac{1}{2}\left(\frac{E^* - Eg}{\sigma}\right)^2\right) dE^*\right) \end{aligned} \tag{4.12}$$

The spectral lineshape then depends on the radiative lifetime ratio τ_r/τ_c. If charge carriers have enough time to relax into states of lower energy before recombining radiatively, τ_r/τ_c becomes large and the spectral center of gravity shifts below the average band gap, leading to an increasingly asymmetric lineshape. Vice versa, if τ_r/τ_c is small, i.e. charge carriers recombine radiatively before they relax into states of lower energy, the lineshape approaches a simple gaussian centered around the average band gap (see Fig. 4.14).

Replacing the excitonic component of the model as presented by Christen with the model proposed by Schubert leads to

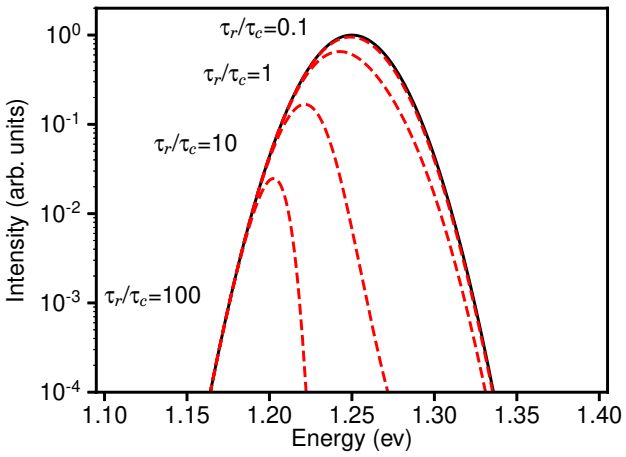

Figure 4.14: Lineshape according to the model proposed by Schubert for different ratios of τ_r and τ_c. For simulation, a band gap of 1.25 eV and a broadening of 20 meV is assumed. The black curve is a simple gaussian centered at the band gap. The dashed red curves were simulated using (4.12).

$$
\begin{aligned}
I =& I_{2D} \cdot \operatorname{erfc}\left(\frac{E_g - E}{\sqrt{2}\sigma_{2D}}\right) \cdot \exp\left(\frac{E_g - E}{k \cdot T}\right) \\
&+ I_{0D} \cdot \exp\left(-\frac{1}{2}\left(\frac{E - Eg}{\sigma_{0D}}\right)^2\right) \\
&\times \exp\left(-\frac{\tau_r}{\tau_c}\frac{1}{\sqrt{2\pi}\sigma_{0D}}\int_{-\infty}^{E}\left(-\frac{1}{2}\left(\frac{E^* - Eg}{\sigma_{0D}}\right)^2\right) dE^*\right)
\end{aligned}
\tag{4.13}
$$

LO phonon replicas are already present in the low-temperature photoluminescence of InAs/GaAs SML stacks and the addition of TESb to the growth cycle results an increase of their intensity (see section 4.2.2). As the relative intensity of the phonon replicas is expressed by the Huang-Rhys factor, the model was further extended by adding terms to the excitonic component scaled by the Poisson distribution [108, 200 and 208] [109–111], and with an appropriate energy separation to account for the phonon energy (around the LO phonon energy of GaAs of 35.3 meV [45]).

$$I = \sum_{i=0}^{n} I_{0D} \cdot \frac{S^n \cdot e^{-S}}{n!} \cdot \exp\left(-\frac{1}{2}\left(\frac{E-(Eg-n\cdot E_{LO})}{\sigma_{0D}}\right)^2\right) \times \exp\left(-\frac{\tau_r}{\tau_c}\frac{1}{\sqrt{2\pi}\sigma_{0D}}\int_{-\infty}^{E}\left(-\frac{1}{2}\left(\frac{E^*-(Eg-n\cdot E_{LO})}{\sigma_{0D}}\right)^2\right)dE^*\right) \tag{4.14}$$

A correction of the spectrum according to the spectral transfer function of the measurement setup leads to a non-constant noise floor. This characteristic was included by a second-order polynomial. The complete luminescence shape is therefore given by

$$I = I_{2D} \cdot \mathrm{erfc}\left(\frac{E_g-E}{\sqrt{2}\sigma_{2D}}\right) \cdot \exp\left(\frac{E_g-E}{k\cdot T}\right) \sum_{i=0}^{n} I_{0D} \cdot \frac{S^n \cdot e^{-S}}{n!} \cdot \exp\left(-\frac{1}{2}\left(\frac{E-(Eg-n\cdot E_{LO})}{\sigma_{0D}}\right)^2\right) \times \exp\left(-\frac{\tau_r}{\tau_c}\frac{1}{\sqrt{2\pi}\sigma_{0D}}\int_{-\infty}^{E}\left(-\frac{1}{2}\left(\frac{E^*-(Eg-n\cdot E_{LO})}{\sigma_{0D}}\right)^2\right)dE^*\right) + p_2\cdot E^2 + p_1\cdot E + p_0 \tag{4.15}$$

Fig. 4.15 shows a fit of the complete lineshape as given in equation 4.15 to the low temperature measurement of a sample containing a single 7x InAs/GaAs SML stack with 6.98 µmol TESb supply. From it, the Huang-Rhys factor, broadening factors, and integrated intensities of 2D and 0D contributions were extracted and the ratio of integrated intensities was calculated.

The fitting of the spectra is performed using the scipy library [199] which uses a Levenberg-Marquard algorithm. For spectra as depicted in Fig. 4.15 where the LO phonon peaks clearly visible the fitting procedure works very well. For spectra with less distinct features however, an almost identical sum spectrum can be obtained from a fit with slightly varying parameters, e.g. a small shift in peak energy can be compensated by an adjustment of broadening factor and peak intensity, resulting in an increase of the errors obtained from the fit. This is especially pronounced for the extracted integrated intensities. Therefore, only qualitative comparisons were made for this parameter.

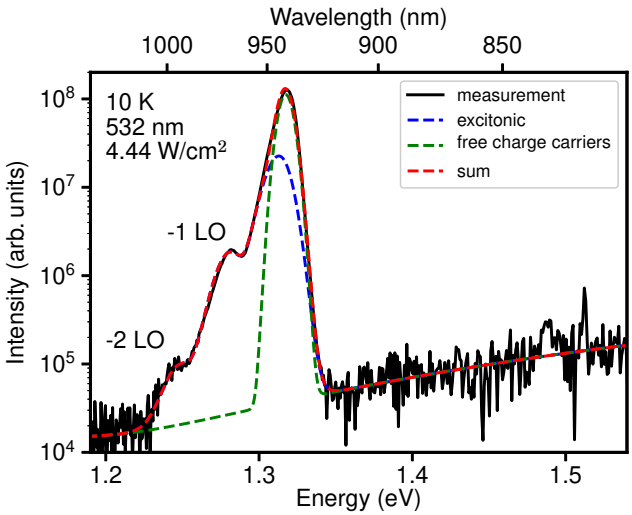

Figure 4.15: Fit of equation 4.15 to the experimentally obtained low-temperature photoluminescence of a sample containing a 7x InAs/GaAs SML stack with 6.98 µmol TESb supply.

Temperature-dependent PL peak positions

In addition to the low-temperature lineshape, the shift of the PL peak energy with temperature can be analyzed. An often used empirical model describing the band gap shift with temperature was proposed by Varshni [200].

$$E(T) = E(0) + \frac{\alpha T^2}{T + \beta} \tag{4.16}$$

Here, E(0) is the band gap a T = 0K, α is the limit for the band gap shift (slope) at infinite temperature and β is comparable to the Debye temperature. In later publications, a deviation of the model from measured data at low temperatures was found, leading to the proposition of alternative models, e.g. the model by Pässler [201].

$$E(T) = E_0 - \frac{\alpha\Theta}{2}\left(\sqrt[p]{1 + \left(\frac{2T}{\Theta}\right)^p} - 1\right) \tag{4.17}$$

α is again the slope limit for T $\rightarrow \infty$, Θ is comparable to the average phonon temperature and p is connected to the degree of phonon dispersion.

Both models describe the monotonic shrinking of the band gap with increasing

temperature. However, in samples with charge carrier localization, a deviating behavior of energy-temperature dependence has been found [202–212], often exhibiting an S-shape. To account for this, Eliseev proposed the band-tail model [203], which adds a σ^2/kT-term to the temperature dependence.

$$E(T) = E_0 - \frac{\alpha\Theta}{2}\left(\sqrt[p]{1+\left(\frac{2T}{\Theta}\right)^p} - 1\right) - \frac{\sigma^2}{kT} \tag{4.18}$$

k is the Boltzmann constant and σ is a measure of the average potential fluctuations in the measured sample.

As the model behind the additional term is based on a Gaussian density of states, it does not take into account the actual shape of the luminescence spectrum. Therefore, σ values extracted from the temperature dependent peak energy positions deviate significantly from the broadening factors extracted from a full lineshape fit as described in the previous section. However, it still provides a clear indicator for the onset of (strong) charge carrier localization and is significantly more robust than the lineshape analysis.

4.2.2 Addition of Sb

To gain an understanding of the influence of Sb on electronic and optical properties, an initial InAs/GaAs submonolayer stack was chosen as basis for a sample series where only the supplied TESb amount is varied. The basic structure is a 7x submonolayer stack with nominally 0.135 nm InAs (0.45 ML) and 0.889 nm GaAs (3.15 ML), forming on average an InGaAs layer of 7.17 nm total thickness and $x_{In} = 0.132$. Using this initial structure, an Sb flush was added prior to each InAs deposition. Control of the TESb amount was achieved by varying the flush time from 3 to 96 s while maintaining a constant TESb molar flow of 8.73 µmol/min ($1.3{\cdot}10^{-3}$ mbar partial pressure), resulting in an absolute TESb supply of 0.44 to 13.96 µmol. Due to growth rate reduction and Sb incorporation, the thickness of the SML stack is reduced to 3.95 nm and the In+Sb composition is increased to 0.204 for the largest TESb amount.

Low-temperature PL spectra of the sample series and the parameters extracted directly from the measurement are shown in Fig. 4.16. A monotonous redshift of the peak emission wavelength from 882 to 952 nm at 10 K is found. Furthermore the intensity of the -1 LO phonon replica, which is already present in the sample

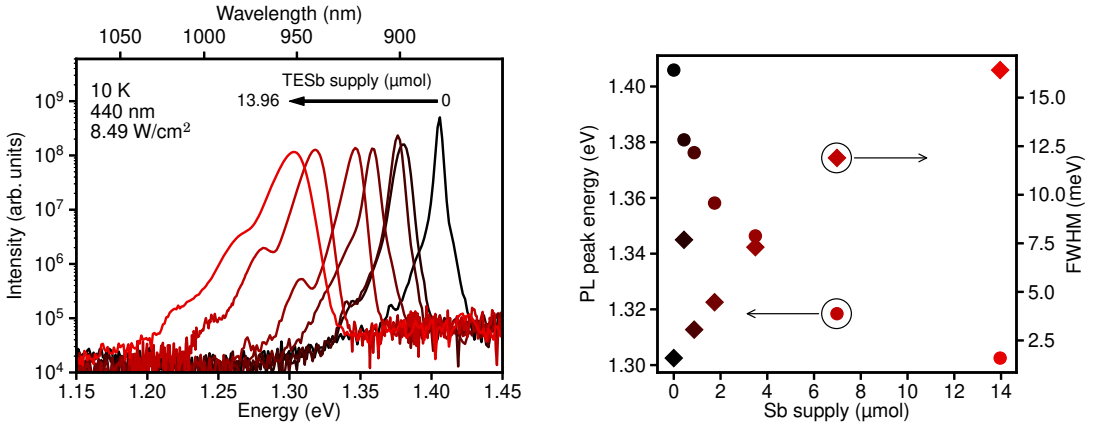

Figure 4.16: Low temperature photoluminescence of InAs/GaAs SML stacks with increasing TESb supply. (a) Measured spectra and (b) extracted peak energy positions and FWHM.

without Sb, increases in intensity. At sufficiently large TESb supplies, the -2 LO phonon replica can be observed as well. The FWHM of the emission increases from 1.6 to 16.4 meV.

The obtained spectra were fitted with the previously introduced lineshape model (section 4.2.1). Broadening factors of 0D and 2D contributions increase approximately linear upon addition of TESb (2D: 1.5±0.1 to 6.6±0.3 meV, 0D: 8.1±0.3 to 22.5±3.6 meV, see Fig. 4.17a). As XRR scans (c.f. section 4.1.3) showed no increase in interface roughness, the larger broadening is attributed to an increased compositional disorder.

Fig. 4.17b shows the development of the HRF from 0.028±0.005 to 0.106±0.028 with increasing Sb supply. This is an indication of an enhanced dipole moment and agrees with the eight-band k·p simulation for Sb incorporation into the In-rich regions in the SML stack (section 4.1.1). Huang-Rhys factors of up to 0.026 have been determined for InAs/GaAs quantum dots by Heitz *et al.* [110, 111]. The value determined here is even larger than the one calculated theoretically for the largest local Sb content. This can be explained with the assumptions made for the simulation. A sigmoidal composition profile was assumed over the simulation area, which results in the central quantum dot having the largest In-content and a localization of the wave function in it. In real samples, the difference between neighboring quantum

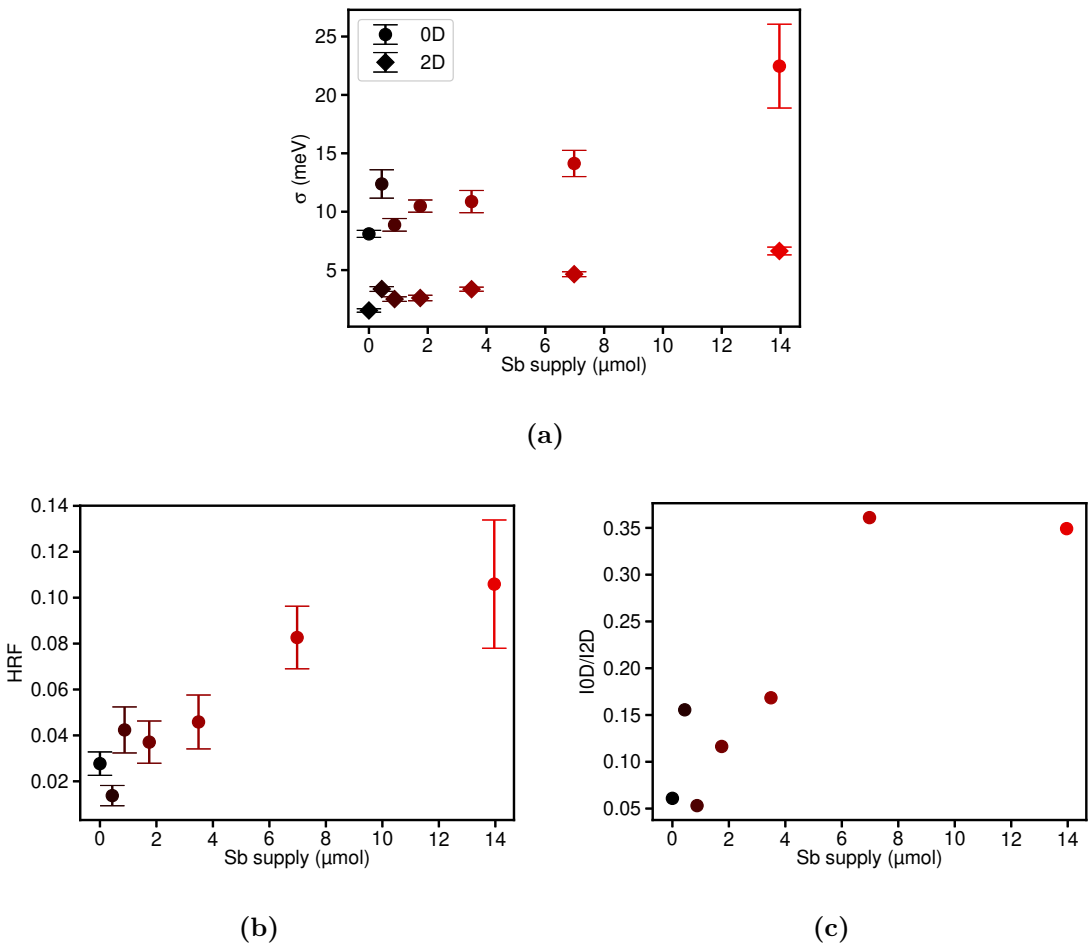

Figure 4.17: Parameters extracted from the lineshape fit of PL measurements at 10 K (see Fig. 4.16). (a) Extracted broadening factors, (b) Huang-Rhys factor and (c) 0D/2D intensity ratio.

dots might be less pronounced, enabling an even larger spreading of the electron wave function and thereby a further reduction of the wave function overlap, i.e. an increase of the HRF.

Finally, the ratio of the integrated intensities is extracted from the lineshape fit (Fig. 4.17c), showing at maximum a six-fold increase of the 0D contribution from 0.06 to 0.36.

From temperature-dependent measurements, the shift of the peak emission energy was determined (Fig. 4.18a). Samples with TESb supplies of 3.49 µmol and less exhibited predominantly band gap shrinkage with only minimal signs of localization at best. For two samples with largest TESb supply in this series (6.98 and 13.96

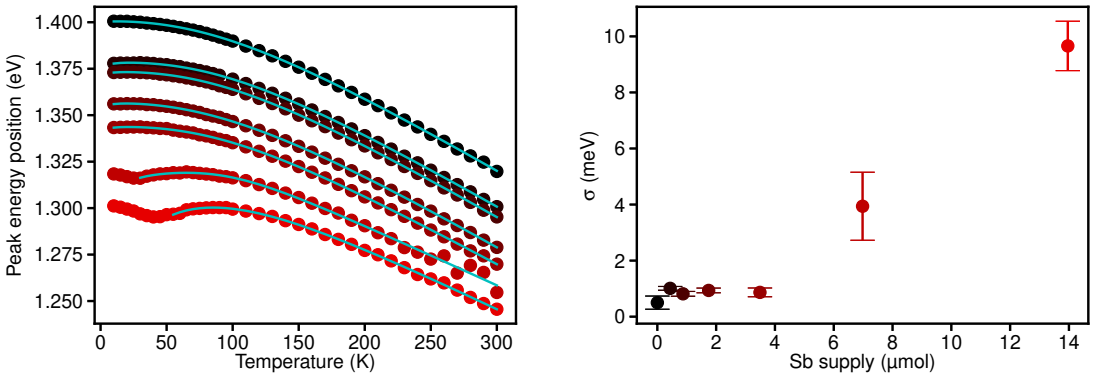

(a) **(b)**

Figure 4.18: Results from the temperature-dependent PL measurements of the samples with varying TESb flush time. (a) Peak energy positions. (b) Potential fluctuations as extracted from a fit of the extended Pässler model (compare (4.18)).

µmol), however, a noticable S-shape, which is characteristic for a redistribution of charge carriers with temperature, is found. Fitting the obtained data with (4.18) allows for extraction of the average potential fluctuations (Fig. 4.18b). For samples not exhibiting an S-shape, potential fluctations up to 1.0 meV only were found. For the other two samples, a strong increase to 3.9±1.2 meV at 6.98 µmol TESb supply and to 9.7±0.9 meV at 13.96 meV is found.

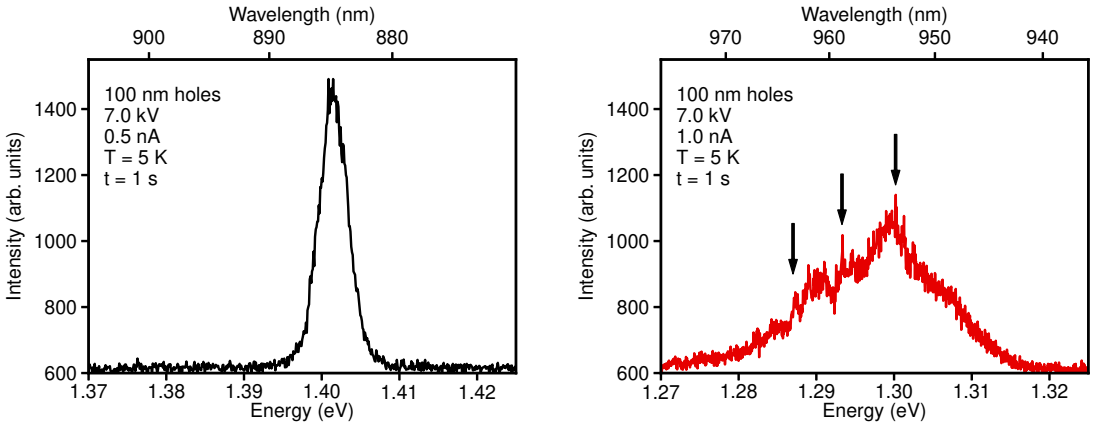

(a) **(b)**

Figure 4.19: Spatially resolved CL spectra of (a) a sample without Sb and (b) a sample with 13.96 µmol TESb supply.

Finally, highly spatially resolved cathodoluminescence measurement shows a narrow emission spectrum where no individual emission lines can be discerned for the sample without TESb flush before the InAs deposition (Fig. 4.19a). In contrast, the sample with 13.96 µmol TESb supply exhibits a much broader spectrum with excitonic emission lines (Fig. 4.19b), which is direct proof of an enhanced charge carrier localization.

Overall, the supplied TESb amount is a parameter by which the emission wavelength of the SML stack can be tuned. For sufficiently large supplies, evidence of strong charge localization is found from temperature-dependent PL and spatially resolved CL measurements, in agreement with the eight-band k·p simulations of Sb incorporation into the In-rich regions and the amount of supplied TESb can be used to adjust the localization depth in the SML stack.

4.2.3 Variation of the GaAs spacer thickness

The influence of TESb on structural properties has been neglected for the simulations, but as was shown in section 4.1.3 that incorporation of Sb also entails a growth rate reduction. Specifically the GaAs spacer between the InAs sheets is of interest as it controls the vertical electronic coupling. Therefore its influence on localization properties needed to be investigated in detail.

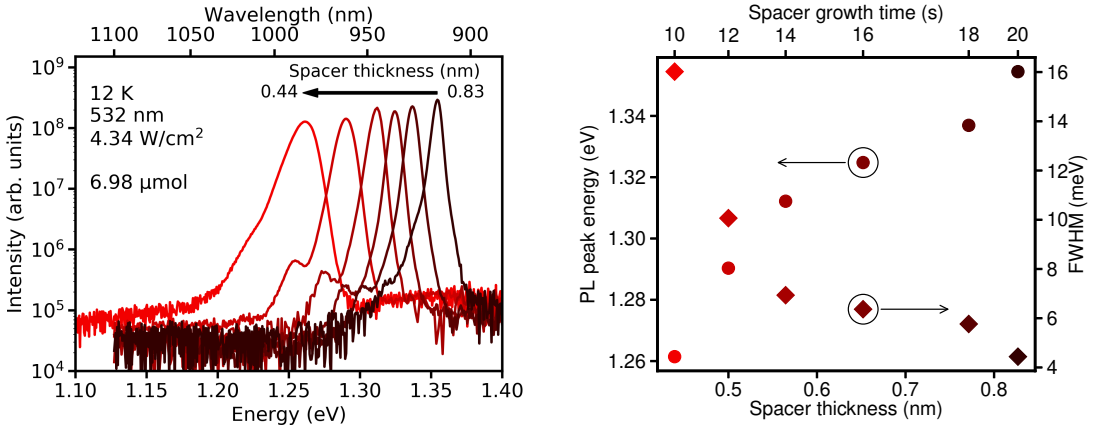

Figure 4.20: Low temperature photoluminescence of InAs/GaAs SML stacks with 6.98 µmol TESb supply and varying spacer thickness. (a) Measured spectra and (b) extracted peak energy positions and FWHM.

Starting with the two largest TESb supplies from the previous investigation, two sample series were fabricated, where the spacer thickness between the InAs sheets was varied by increasing the spacer growth time[2] from 10 to 20 s in steps of 2 s.

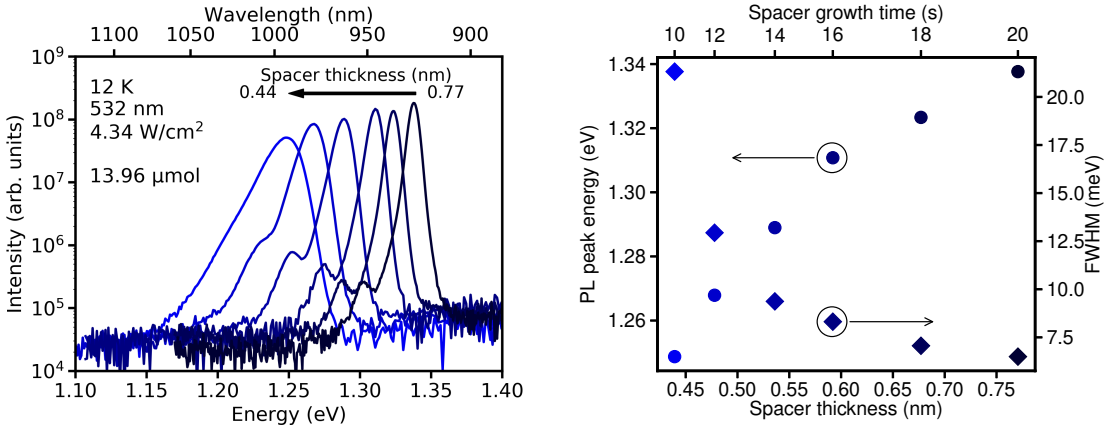

(a) **(b)**

Figure 4.21: Low temperature photoluminescence of InAs/GaAs SML stacks with 13.96 µmol TESb supply and varying spacer thickness. (a) Measured spectra and (b) extracted peak energy positions and FWHM.

As figures 4.20 and 4.21 show, the emission wavelength increases with decreasing spacer thickness (from 916 to 983 nm with 6.98 µmol and from 927 nm to 993 nm for 13.96 µmol TESb). At the same time, the FWHM increases from 4.4 to 16.0 meV and from 6.5 to 21.3 meV, respectively, and the emission becomes more quantum dot like, i.e. the 0D contribution to the total emission intensity increases (Fig. 4.22a).

No clear trend with respect to spacer thickness could be determined for the Huang-Rhys factor. For small InAs sheet separations the luminescence lineshape becomes very broad, which makes it difficult to discern individual peaks and leads to large fitting errors. On average, however, the HRF is larger for samples with larger TESb supply (see Fig. 4.22b), as one would expect from the previous investigation of the TESb flush series.

To determine the onset of strong charge carrier localization with respect to the spacer thickness, temperature-dependent measurements were again performed. For both sample series, the potential fluctuations increase with decreasing spacer thick-

[2]These are the complementary samples to the 5-fold 7x SML stacks used for the investigation with XRR in section 4.1.3

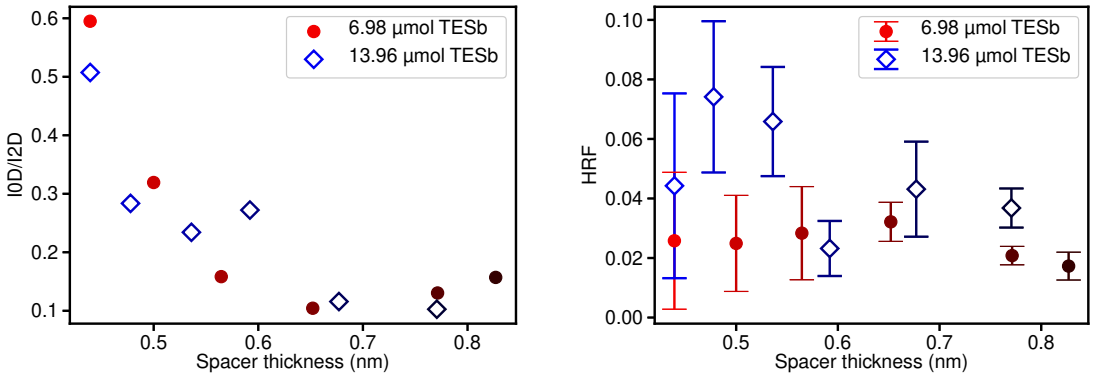

(a) **(b)**

Figure 4.22: Parameters extracted from the lineshape fits of low-temperature PL measurements on the samples with varying GaAs spacer thicknesses. (a) Extracted 0D/2D intensity ratios and (b) Huang-Rhys factors.

nesses, resulting in distinct S-shapes in the temperature-dependence for sufficiently small InAs sheet separations.

For a TESb supply of 6.98 µmol, the spacer thickness reduction from 0.83±0.11 to 0.44±0.11 nm (2.9±0.4 to 1.6±0.4 monolayers) leads to an increase of the potential fluctuations from 0.8±0.2 to 13.5±0.9 meV. At the larger supply of 13.96 µmol TESb an increase of 1.6±0.1 to 15.3±1.1 meV is found for spacer thicknesses reduced from 0.77±0.08 to 0.44±0.11 nm (2.7±0.3 to 1.6±0.4 monolayers).

For potential fluctuations below 2 meV, an S-shape is only barely discernible in the temperature-dependent PL peak energies. Additionally, once the fluctuations are larger than this threshold, they increase exponentially (Fig. 4.23c). Therefore this value is defined as onset of strong charge carrier localization. Consequently, 0.5±0.11 nm (1.8±0.4 ML) and 0.54±0.08 nm (1.9±0.3 ML) are the spacer thicknesses for 6.98 µmol and 13.96 µmol TESb, respectively, below which charge carrier localization sets in. This matches very well with the thickness value where the In+Sb content has dropped to half of its initial value (1.80±0.34 ML, calculated from the previously obtained segregation coefficient of 0.68±0.05).

As the larger TESb amount shows larger potential fluctuations and at starts at a slightly larger spacer thickness, it seems as if a critical local Sb density has to be present in order to enable strong charge carrier localization.

This investigation is concluded with three further samples that allow a comparison

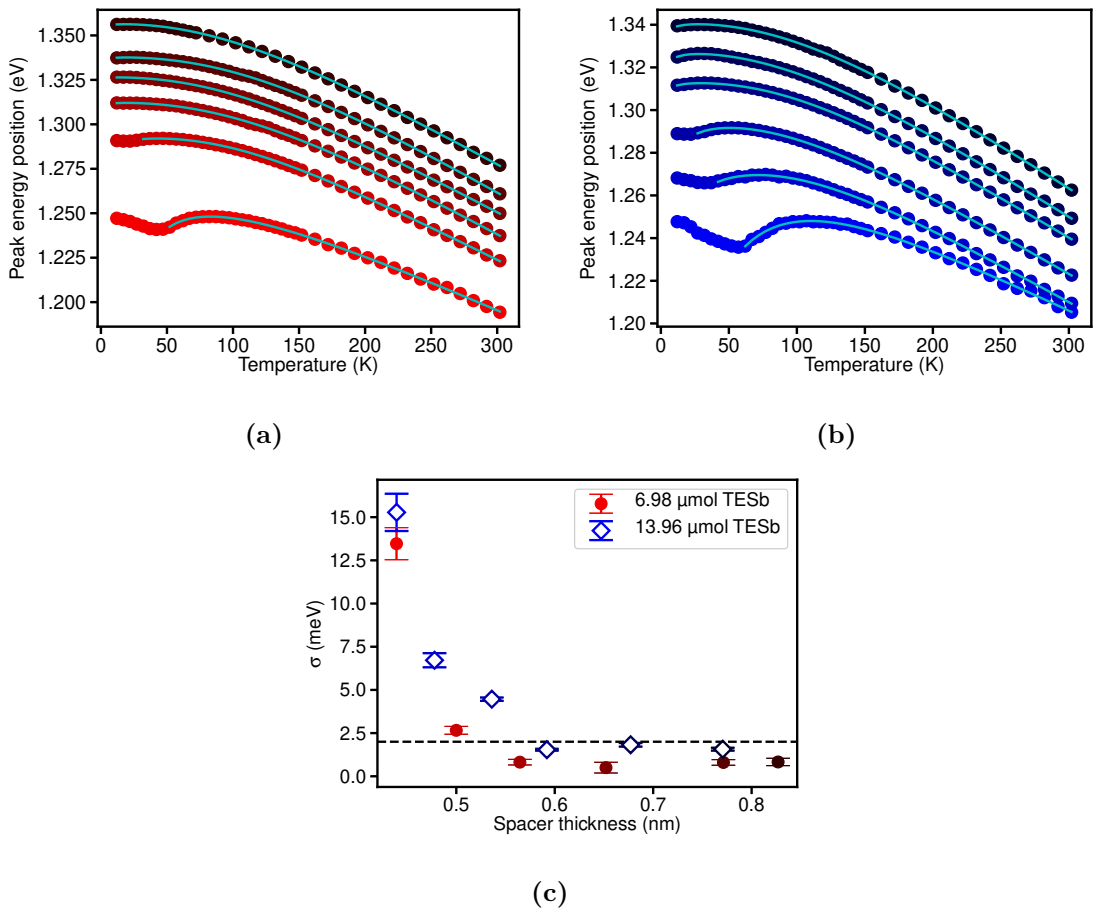

Figure 4.23: Results from the temperature-dependent PL measurements on the samples with varying GaAs spacer thicknesses. Peak energies of the samples with (a) 6.98 µmol and (b) 13.96 µmol TESb supply. (c) Potential fluctuations extracted from a fit of the peak energy positions.

between Sb-free and Sb-containing SML structures for reduction of spacer thickness. The first two are 10x InAs/GaAs SML stacks without TESb supply with spacer thicknesses of 0.96 nm (3.4 ML) and 0.48 nm (1.7 ML), respectively. The third sample is a 20x SML stack with 0.44 µmol TESb supply and a spacer thickness of 0.31 nm (1.1 ML). Fig. 4.24a shows the low temperature PL spectra. The reduction of the InAs sheet separation (black and red curve) leads to a redshift of the emission from 905.5 nm to 955.5 nm and an increase of the FWHM from 3.0 to 4.8 meV, which is a factor of 1.6. However, this increase is still significantly smaller than the one resulting from an addition of TESb (compare Fig. 4.16). In contrast, the 20x stack containing Sb (blue curve) is redshifted to 1093 nm due to Sb and the larger total

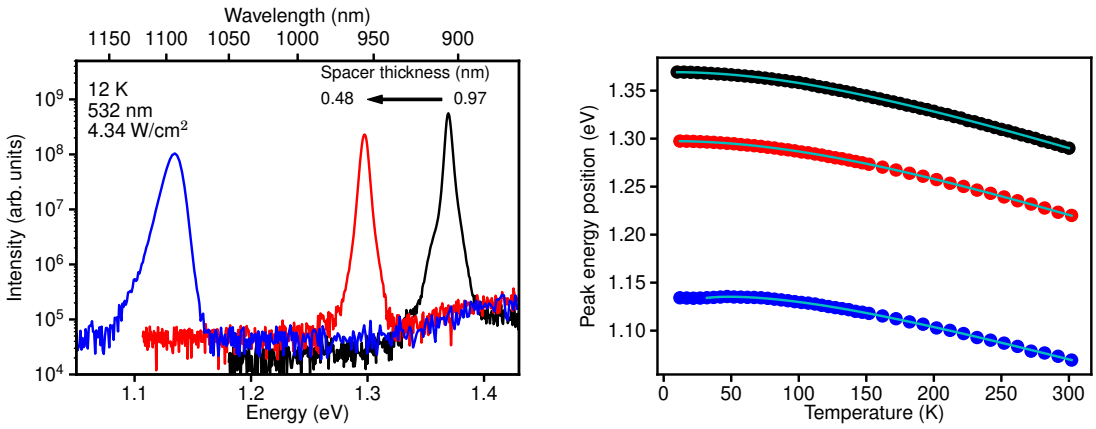

Figure 4.24: (a) PL measurements at 10 K showing the influence of the spacer thickness on samples with and without TESb supply. (b) Peak energy positions extracted from temperature-dependent PL measurements.

stack thickness. It exhibits a FWHM of 12.4 meV, being comparable to samples with significantly larger TESb supplies. Temperature-dependent PL measurements finally show, that the samples without TESb supply exhibit only band gap shrinkage whereas an S-shape is present for the Sb-containing sample. The extracted potential fluctuations are 0.5±0.3 meV without TESb and 4.4±0.5 meV with TESb.

From this investigation, the spacer thickness could be identified as an additional parameter besides the TESb supply for tuning of the emission wavelength and localization depth in SML stacks. As a prerequisite for the latter, TESb has to be supplied during the growth sequence as no evidence of strong charge carrier localization is found for binary InAs/GaAs SML stacks.

4.2.4 Varying the number of deposition cycles

As the layer thicknesses separating the TESb flushes are only about one nm (about 4 monolayers) at maximum, it is conceivable that Sb accumulation effects may occur. Therefore the influence of the number of deposition cycles on optical properties was investigated. Using the largest TESb supply of 13.96 µmol, the number of deposition cycles was varied between 4 and 25 while keeping InAs/GaAs ratio and individual sheet thickness constant.

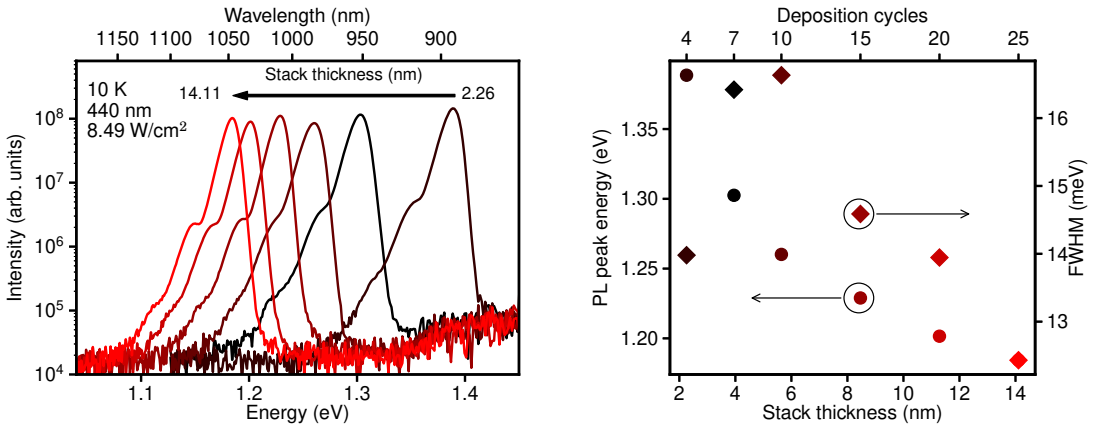

(a) (b)

Figure 4.25: Low temperature photoluminescence of InAs/GaAs SML stacks with 13.96 µmol TESb supply and a varying number of deposition cycles i.e. total stack thickness. (a) Measured spectra and (b) extracted peak energy positions and FWHM.

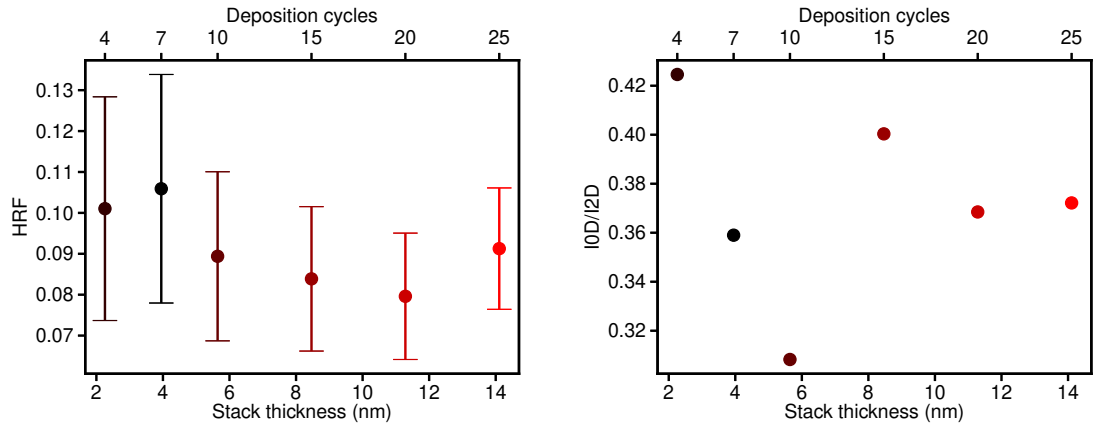

(a) (b)

Figure 4.26: Parameters extracted from lineshape fits of the low-temperature PL measurements (see Fig. 4.25a) of samples with varying total stack thickness. (a) Extracted Huang-Rhys factors and (b) 0D/2D intensity ratios.

As seen in Fig. 4.25, the emission wavelength continuously redshifts from 952 nm to 1047 nm upon increasing the deposition cycles from 4 to 25, which corresponds to an increase of the total SML stack thickness from 2.26 nm to 14.11 nm. The FWHM first increases from 13.98 meV at 4 deposition cycles to 16.63 meV at 10 repetitions. Further increasing to 25 growth cycles decreases the FWHM again

to 12.43 meV. Therefore, the maximum relative shift in this series is about 35%. However, comparing these results to the TESb flush series shows that all samples have large emission broadenings in comparison to samples with less or without TESb supply. Further analysis of the lineshape yielded similar results (Fig. 4.26) for both Huang-Rhys factors and 0D/2D ratios which remain on a comparatively high level relative to samples without TESb.

In temperature-dependent PL measurements, the peak energies of all samples exhibit an S-shape. The extracted potential fluctuations vary by a factor of about 2, but again, the extracted values are large compared to samples with less TESb supply and remain above the previously defined onset for strong charge carrier localization of 2 meV at all times.

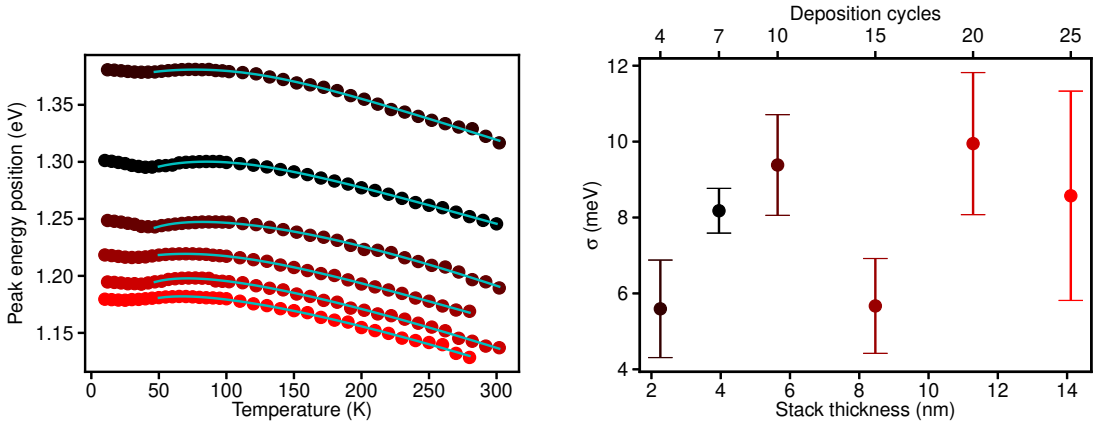

(a) **(b)**

Figure 4.27: (a) Temperature-dependent peak energy positions and (b) extracted potential fluctuations.

Judging from this investigation, it is unlikely that the repeated supply of TESb leads to accumulation effects. While there is a certain spread in the determined results, all of them remain on a level above samples with smaller TESb supplies and at the same time, no indication of an increase of localization with increasing stack thickness is found. An additional point is that the samples were not grown in a consecutive manner. The sample series consists of 6 samples and the first and last sample are 30 epitaxy runs apart. Therefore, it is not unreasonable to assume that the variations determined from the measurements are caused by run to run differences of the epitaxy.

4.3 Tuning of luminescence properties

In the previous section, the influence of TESb supply, GaAs spacer thickness between InAs sheets, and number of deposition cycles on emission wavelength and localization properties has been investigated by low-temperature and temperature-dependent PL measurements. As this section puts more focus on the application aspect, room-temperature PL measurements were investigated and the emission wavelength and FWHM were extracted directly from the PL spectra.

Table 4.3: General influence of growth parameters on emission properties as extracted from low-temperature PL measurements

Growth parameter	Influence on emission wavelength	FWHM
TESb supply	↑	↑
Spacer thickness	↓	↓
Number of deposition cycles	↑	→

Table 4.3 shows a very simple summary of the influence of the investigated growth parameters. As the total stack thickness primarily shifts the emission wavelength and has only a very small influence on the FWHM, it should be possible to control both emission properties independently of each other. For this, either TESb supply, or spacer thickness, or a combination of both were used to choose the emission broadening while the emission wavelength was afterwards adjusted by the number of deposition cycles.

This is showcased in Fig. 4.28 for three different wavelengths (940 nm, 970 nm and 1050 nm) with two samples for each wavelength. In all cases, the first sample is a submonolayer stack without TESb supply. Upon addition of the TESb flush, the redshifted emission has to be compensated. For the samples in Figs. 4.28a and 4.28b, this was achieved by changing the number of deposition cycles. The reduced GaAs spacer thickness is a byproduct of the TESb flush due to the growth rate reduction. In the last case, (Fig. 4.28c), the spacer growth time was adjusted as well.

An additional question to answer was the wavelength range which can be covered with the submonolayer stacks. In previous works at the TU Berlin, the SML stacks have shown emission wavelengths of up to 1050 nm [126, 127]. In this thesis, the

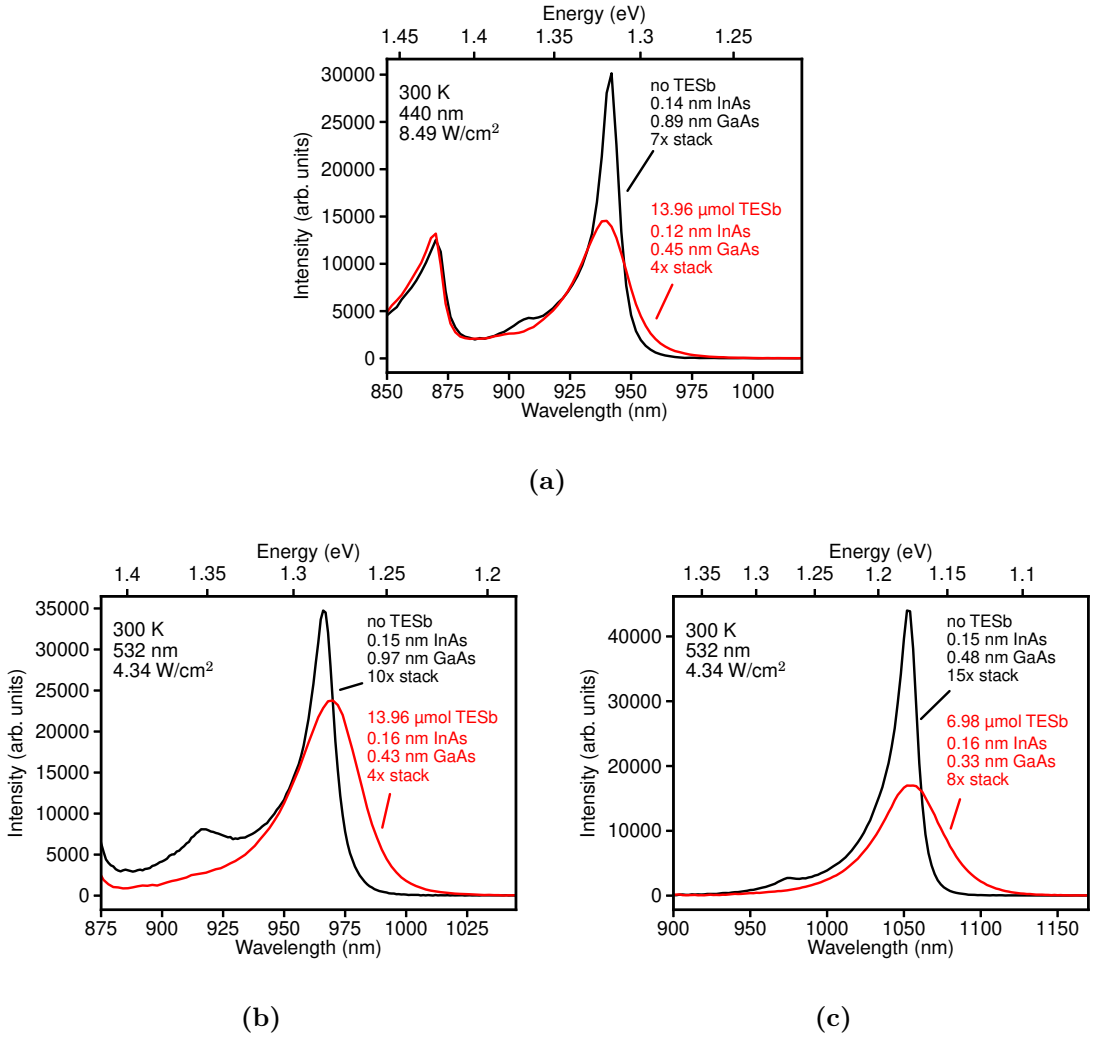

Figure 4.28: Comparison of different SML stacks without and with TESb supply, adjusted to approximately the same emission wavelength at (a) 940 nm, (b) 970 nm, and (c) 1050 nm.

maximum wavelength achieved without TESb is 1083 nm for a 15x SML stack of 6.93 nm thickness and an In-content of 31.8% (0.15 nm InAs and 0.31 nm GaAs). A further increase of the stack thickness or composition resulted in the formation of dislocations (visible by optical inspection with a nomarski microscope) and a degradation of the PL emission.

As has been shown previously, supplying TESb during the growth sequence without changing any other parameters leads to a significant redshift of the emission. However, this also cannot be done infinitely and has certain limitations. A too large amount of Sb also leads to the formation of defects, necessitating a careful adjustment of all three growth parameters. As shown in section 4.2.3, a 20x SML stack with 0.44 µmol TESb supply and a spacer thickness of 0.31 nm exhibits a PL emission wavelength of 1093 nm at 10 K and still shows signs of charge carrier localization. At room temperature the PL wavelength of this sample is 1160 nm. The maximum wavelength achieved in this thesis is 1178 nm for a 30x SML stack with 0.44 µmol TESb supply. Larger TESb supplies, total layer thicknesses, or average compositions again led to formation of defects.

To gain an overview of the achievable emission properties of submonolayer stacks, it is helpful to put the FWHM in relation to emission wavelength (see Fig. 4.29).

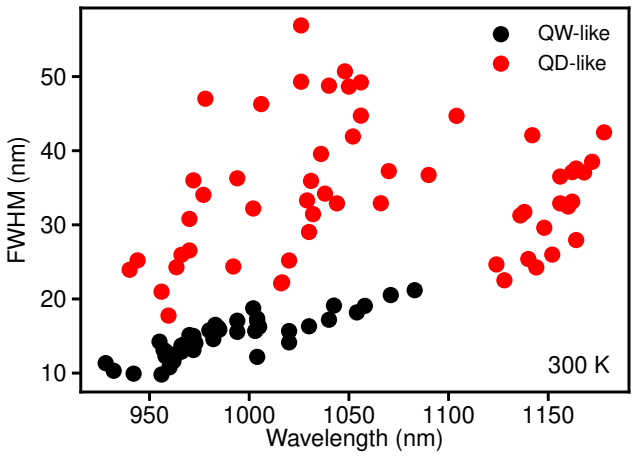

Figure 4.29: FWHM with respect to the emission wavelength.

By doing so, a wavelength range from 900 to about 1100 nm is covered with samples showing quantum well-like emission properties (black circles). The FWHM of these samples samples lies between 5 and 20 nm and shows an overall increase

with increasing emission wavelength. As longer wavelengths are achieved for SML stacks of larger thickness, formation of In-rich regions with varying degrees of local In content, i.e. an increase of compositional disorder, is more likely. An extended wavelength range is covered by samples exhibiting quantum dot-like properties (red circles) as the maximum achievable wavelength is increased to about 1180 nm. Additionally, the FWHM is now tunable independently of the wavelength, due to the additional tuning parameter provided by TESb supply. At maximum, the FWHM can now be tuned between 5 and 50 nm.

5 Properties of lasers with SML QDs

With the ability to control the degree of localization independently of the emission wavelength as demonstrated in the previous sections, it was now possible to compare active media of different electronic configuration in laser diodes. For this analyis, 980 nm was the chosen target wavelength as it has been increasingly used in VCSELs due to its advantages of a higher differential gain [20, 21, 23, 91] and improved temperature stability as compared to VCSELs emitting at 850 nm [18, 19].

Characteristic laser properties are often obtained from length-dependent measurements (see section 2.6), therefore edge-emitting lasers (section 3.3.1) were investigated instead of VCSELs.

A TESb flush of 6.98 µmol was added to the growth sequence of an initial InAs/GaAs submonolayer stack. Using the adsorption model as described in the previous chapter, the average layer compositions were determined to be $In_{0.17}GaAs$ without and $In_{0.13}GaAsSb_{0.14}$ with the flush. To achieve roughly the same emission wavelength around 980 nm, the number of deposition cycles has been adjusted accordingly. A summary of structural and optical properties is given in table 5.1.

Table 5.1: Structural and optical properties of the active regions

Average composition	$In_{0.17}GaAs$	$In_{0.13}GaAsSb_{0.14}$
Deposition cycles	12	6
SML stack thickness (nm)	8.1	2.5
PL emission wavelength (nm)	988	977

5.1 Static laser characteristics

As detailed in section 3.3.1, 100 µm broad laser stripes were fabricated. Using an 1-D mode solver [142] and the structural parameters from tables 3.1 and 5.1, optical

confinement factors of both broad-area structures can be calculated to be 0.0157 without and 0.0048 with TESb.

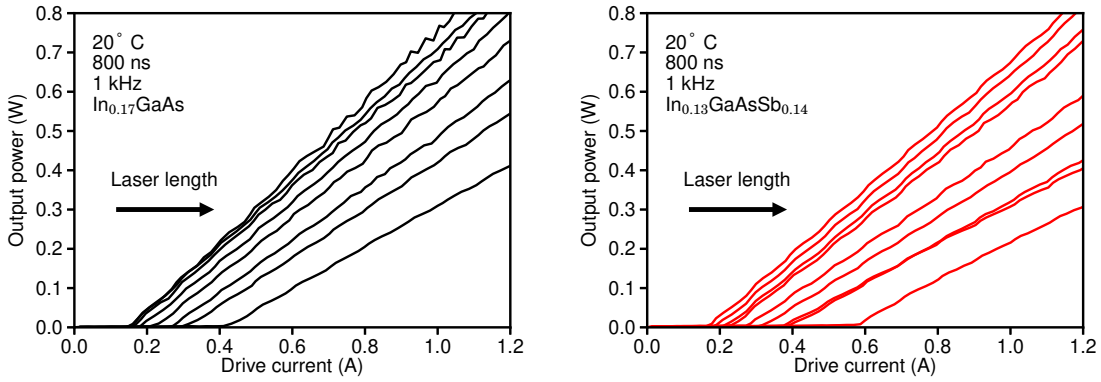

(a) **(b)**

Figure 5.1: L-I curves of broad-area lasers for laser lengths ranging from 1 to 4 mm with (a) InAs/GaAs and (b) InAsSb/GaAs SML stacks as active region.

Fig. 5.1 shows L-I curves of lasers with lengths ranging from 1 to 4 mm. Sub-optimal laser processing may lead to degraded laser performances [194] which manifests in reduced slope efficiencies above threshold. So only those lasers with the largest slope efficiencies for a given device length were selected for subsequent analysis.

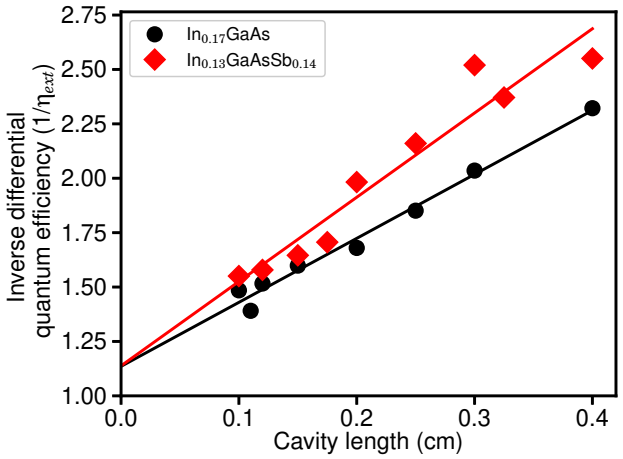

Figure 5.2: Cavity length dependent inverse differential quantum efficiency. Filled symbols are the values extracted from the L-I measurements, solid lines are obtained from least-squares fits of equation 2.20.

Fig. 5.2 shows the inverse differential quantum efficiency with respect to laser cavity length. By fitting the obtained data with (2.20), the internal quantum efficiency and optical losses were obtained. The quantum efficiency remains constant at 0.88±0.03 without and 0.88±0.08 with TESb supply. Meanwhile, the losses increase from 3.12±0.26 cm^{-1} to 4.10±0.77 cm^{-1}.

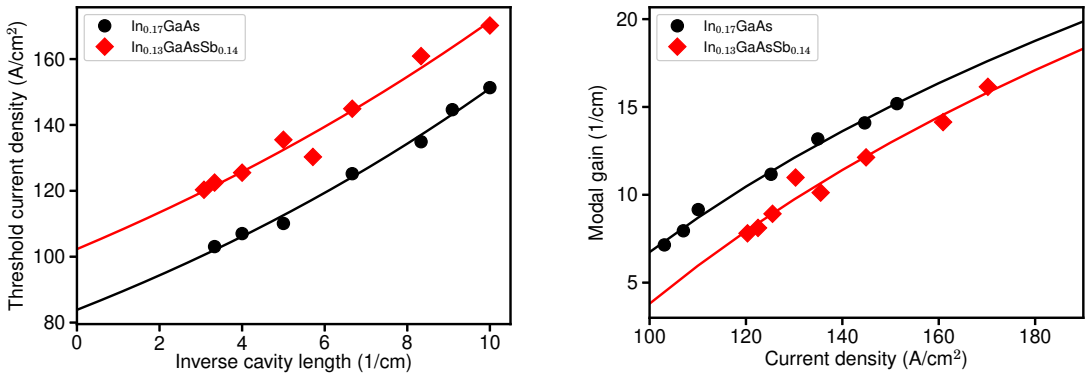

(a) **(b)**

Figure 5.3: Determination of gain parameter and transparency current density. (a) Analysis of the threshold current density vs. inverse cavity length. Solid lines are fits to equation 2.22. (b) Calculated modal gain for different laser lengths vs. threshold current density. Solid lines are fits to (2.21).

To determine the gain parameter at the point of material transparency Γg_0 and the corresponding transparency current density J_{tr}, both the length dependent fit with (2.22) and the approach using the empirical relation between gain and current density (2.21) were employed (compare section 2.6). The second one was performed to verify the applicability of the logarithmic gain approximation as it has been suggested to be inadequate for quantum dot lasers [213].

From the length-dependent fit, an increase of the transparency current density from 63.4±1.4 A/cm^2 to 75.4±2.8 A/cm^2 and a slight increase of the gain parameter 20.5±0.8 cm^{-1} to 23.3±1.7 cm^{-1} was obtained for the Sb-containing active region design.

The fit of (2.21) to the calculated modal gain confirmed both lasers are accurately described by such approximation. Thereby, the increase of the gain parameter from 20.5±0.8 cm^{-1} to 22.6±1.7 cm^{-1} was found, in agreement with the length-dependent fit. Deviations of 13% were found for the transparency current in both cases with an increase from 72.0±1.6 A/cm^2 to 84.5±3.3 A/cm^2. This is likely caused by the

least-squares algorithm which is used for the fit as it minimizes the deviation of threshold current density in the length-dependent fit and the deviation of modal gain in the gain approximation. The qualitative result is, however, the same with an increase of about 18% due to the addition of TESb.

Using the results from the length-dependent measurements and the calculated optical confinement factors, the averaged material gain was determined to 1504±52 cm^{-1} without TESb and 5715±387 cm^{-1} with TESb.

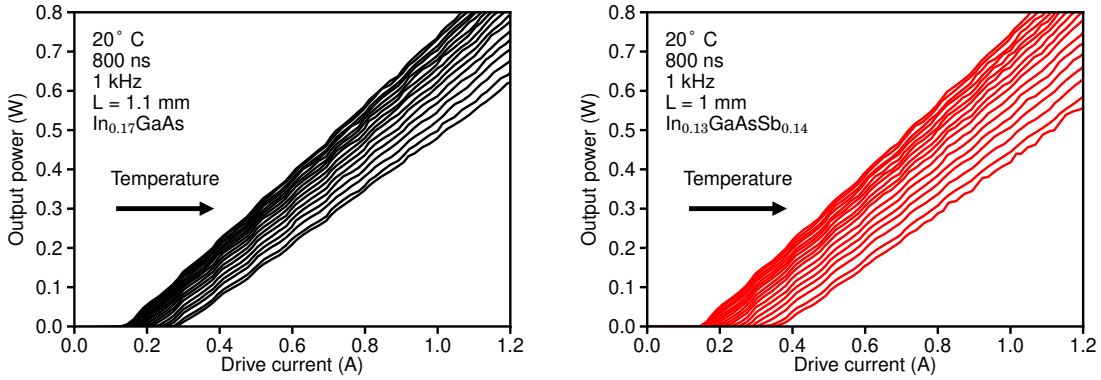

(a) **(b)**

Figure 5.4: Temperature-dependent L-I curves from the broad-area lasers. (a) InAs/GaAs and (b) InAsSb/GaAs active region.

As last figure of merit of the static characteristics from the analysis of broad-area lasers, the temperature stability was investigated. Temperature-dependent L-I curves were recorded for lasers of 1.1 mm (no Sb) and 1 mm (6.98 µmol Sb) length (see Fig. 5.4) in the temperature range from 0° C to 80° C.

Two separate regimes exist with a transition between 40° C and 45° C (Fig. 5.5). Both regions were fitted with the relation 2.30. Below a heatsink temperature of 45° C a decrease of the characteristic temperature from 140.3±2.2 K to 111.9±1.9 K was found, whereas above it, T0 decreases from 88.8±3.0 K to 70.5±1.5 K upon addition of Sb.

The obtained parameters are summarized in table 5.2. Overall, the Sb leads to an increased material gain and a simultaneous increase in threshold current density. The first one can be explained by the large density (∼10^{12} cm^{-2}) of 0D localization centers in the SML stack. The second aspect is caused by the interplay of density, confinement factor and inhomogeneous broadening. As Sb is incorporated into the

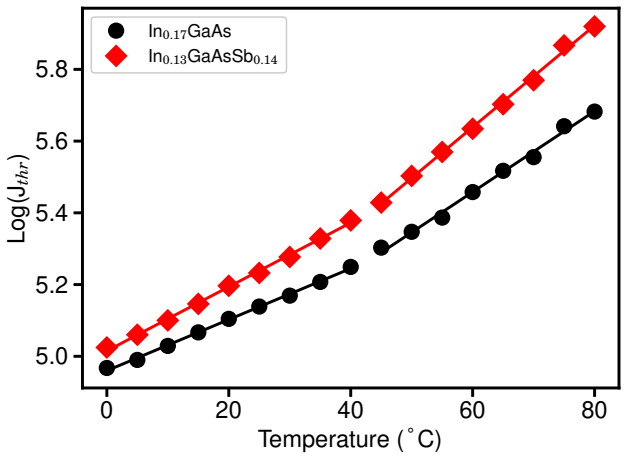

Figure 5.5: Threshold current density with respect to the temperature for the broad-area lasers.

SML stack, the inhomogeneous broadening increases, distributing the gain over a larger spectral range and reducing the peak gain (compare PL spectra in Fig. 4.28b). Additionally, the total stack thickness is reduced for the Sb-containing laser (table 5.1), thus decreasing the confinement factor, further limiting the maximum modal gain. Coupled with the large density of 0D localization centers which need to be inverted before contributing to the lasing process, an increase of threshold current is within expectations. Theoretical calculations suggest that the optimal QD density lies in the low 10^{11} cm^{-2} range [213, 214]. A possible explanation for the decreased temperature stability is given by the influence of Sb incorporation on the wave functions (see section 4.1.1). As Sb is incorporated into the In-rich regions, the electron wave function delocalizes from them. Thus, a larger electron leakage current from the SML stack is within expectation.

The gain of the SML stacks was reexamined again on narrow-stripe lasers to extract wavelength-resolved gain curves. Two 700 µm long lasers fabricated from the same wafer material as the broad-area lasers were investigated here. Due to some processing issues, the lasers have a different ridge width, the laser without TESb being 3.8 µm and the laser with TESb being 3.3 µm wide. The confinement factors calculated with a 2-D modesolver [143] are identical to the ones of the broad-area lasers.

Table 5.2: Internal parameters obtained from the broad-area lasers

	$In_{0.17}GaAs$	$In_{0.13}GaAsSb_{0.14}$
Lasing wavelength (nm)	990±5	979±3
η_i	0.88±0.03	0.88±0.08
α_i (cm^{-1})	3.12±0.26	4.10±0.77
J_{tr} (A/cm^2)	63.4±1.4	75.4±2.8
Γg_0 (cm^{-1})	20.5±0.8	23.3±1.7
Γ	0.0157	0.0048
g_{mat} (cm^{-1})	1504±52	5715±387
T0 ($< 45°$ C)	140.3±2.2	111.9±1.9
T0 ($> 45°$ C)	88.8±3.0	70.5±1.5

Fig. 5.6 shows the LI curves for both lasers under dc conditions. Again, a linear fit above threshold can be used to determine the external quantum efficiency and the threshold current density. Adding Sb results in a decrease of the quantum efficiency from 0.99 to 0.94 while the threshold current density increases significantly from 385 A/cm^{-2} to 669 A/cm^{-2}.[1]

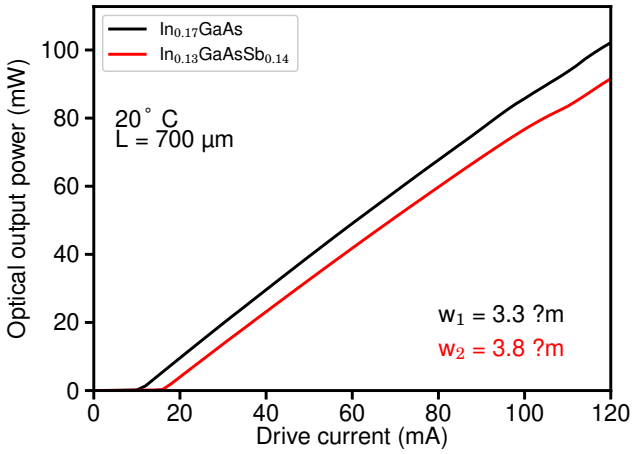

Figure 5.6: L-I curves of the investigated narrow-stripe lasers.

To extract the gain, high-resolution optical spectra were recorded below threshold. As described in section 2.6, two methods are available to extract the gain. As the Hakki-Paoli method is more sensitive to measurement noise, the internal losses

[1]The errors obtained from the fit are smaller than 1% of the fit values, therefore they are not mentioned here.

extracted from the long wavelength region of the spectra are unrealistically small or even positive. As such this method was only used to double check the overall result from the nonlinear least-squares fit.

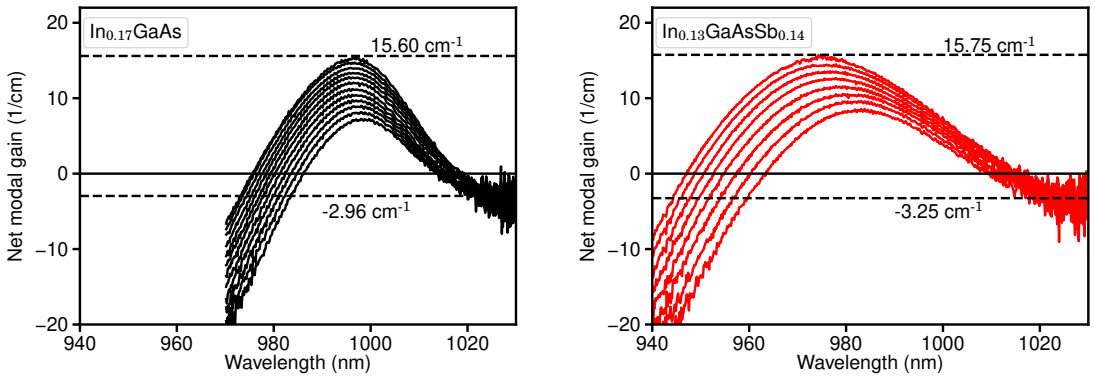

(a) **(b)**

Figure 5.7: Gain obtained from the high-resolution optical spectra of the narrow-stripe lasers driven at currents below threshold. (a) InAs/GaAs and (b) InAsSb/GaAs active region. The dashed lines at the top mark the maximum achieved modal gain while the bottom ones are calculated by averaging the long wavelength tail of all gain curves to obtain the internal losses.

From the gain spectra shown in Fig. 5.7, the internal losses and the maximum modal gain can be determined. For the $In_{0.17}GaAs$ active region a peak modal gain of 15.60±0.14 cm^{-1} and internal losses of 2.96±0.37 cm^{-1} are found while the $In_{0.13}GaAsSb_{0.14}$ active region shows a very similar gain of 15.75±0.18 cm^{-1} and increased internal losses of 3.25±0.49 cm^{-1}.

To extract the local gain parameter and the transparency current density, the peak modal gain was put into relation to the respective current density and fitted with the logarithmic gain approximation (Fig. 5.8)

As before, the gain approximation works very well. From the fit, a gain coefficient of 27.63±0.27 cm^{-1} and a transparency current density of 231±1 A/cm^2 is obtained for the laser without Sb. For the laser with Sb values of 16.20±0.49 cm^{-1} and 269±6 A/cm^2 were determined.

The discrepancy between achieved peak modal gain and gain parameter can be explained by the clamping of the gain once the lasing threshold is reached. As such the maximum gain achieved in this investigation is determined by the losses of the laser structure. The gain parameter on the other hand can be interpreted as a

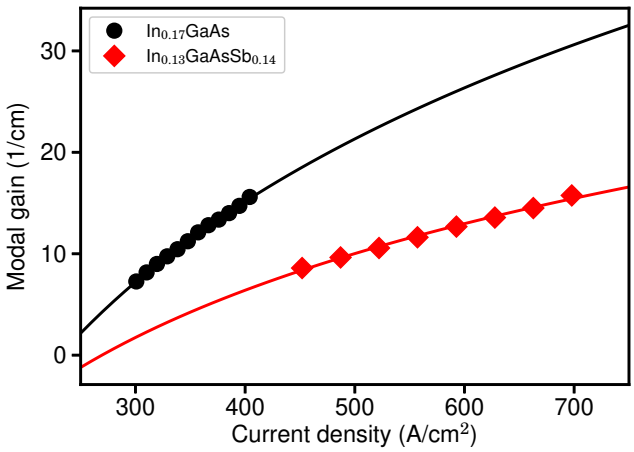

Figure 5.8: Peak modal gain obtained from the gain spectra with respect to the current density.

measure for the potentially achievable modal gain of the active region in question. Therefore, the SML stack without Sb would be able to achieve lasing action in structures of larger losses.

Using the confinement factor and the gain parameter, the material gain could be calculated to 1572±29 cm^{-1} for the laser without and 2696±145 cm^{-1} for the laser with Sb.

Lastly, as expected from the previous PL investigations, the gain measurements show that the FWHM of the gain spectra is strongly increased by about 50% from 25.9±0.3 nm to 42.9±0.2 nm upon the addition of Sb.

Table 5.3 summarizes the results obtained from static measurements on narrow-stripe lasers. Most show similar trends as the parameters obtained from the broad-area lasers, e.g. the transparency current density increases by ∼17%. Internal losses also show an increase in the narrow stripe lasers, albeit only by about 10% in contrast to ∼31% as obtained from broad area lasers which may be explained by differences in processing.

The most striking deviation is in terms of the material gain. While the values for the SML stack without Sb is nearly identical (1504 and 1572 cm^{-1}), a difference of a factor of ∼2 is found for the laser with Sb (5715 to 2969 cm^{-1}). This however, can be explained with the different methods of determination and the influence of the width of the gain spectrum. As mentioned before, any gain value from the

Table 5.3: Internal parameters obtained from the narrow-stripe lasers

	$In_{0.17}GaAs$	$In_{0.13}GaAsSb_{0.14}$
Lasing wavelength (nm)	996±0.2	975±1
J_{th} (A/cm^2)	385	669
η_{ext}	0.99	0.94
ΔG (nm)	25.9±0.3	42.9±0.2
G_{max} (cm^{-1})	15.60±0.14	15.75±0.18
α_i (cm^{-1})	2.96±0.37	3.25±0.49.
J_{tr} (kA/cm^2)	231±1	269±6
Γg_0 (cm^{-1})	27.63±0.27	16.20±0.49
Γ	0.0157	0.0048
g_{mat} (cm^{-1})	1572±29	2696±145

broad-area lasers is averaged over the whole emission spectrum (i.e. modes) as it is determined from L-I curves. In contrast, the value obtained from the optical spectra is only valid for a single longitudinal mode. As such, the results from an analysis of gain-current approximation based on spectrally resolved gain measurements and the ones obtained from length-dependent L-I measurements diverge with the width of the gain spectrum.

5.2 Dynamic laser characteristics

5.2.1 Small-signal response

To assess modulation capabilities of the lasers, small-signal measurements were performed. All obtained curves were fitted with three-pole transfer functions as described in section 2.6. Fig. 5.9 shows the S_{21} response curves with the largest -3-dB bandwidth for both lasers.

For the laser without Sb a maximum bandwidth of 7.2 GHz at a drive current of 90 mA was found and for the laser with Sb a bandwidth of 5.8 GHz at drive currents of 100 mA. As lasers based on quantum dots exhibit a higher intrinsic damping as compared to quantum well lasers, a decreased -3-dB frequency is expected due to the larger degree of 3D localization upon addition of Sb to the active region.

By comparing the resonance frequency to the square root of current above threshold, the D-factor (see (2.38)) could be determined. For the laser without TESb flush

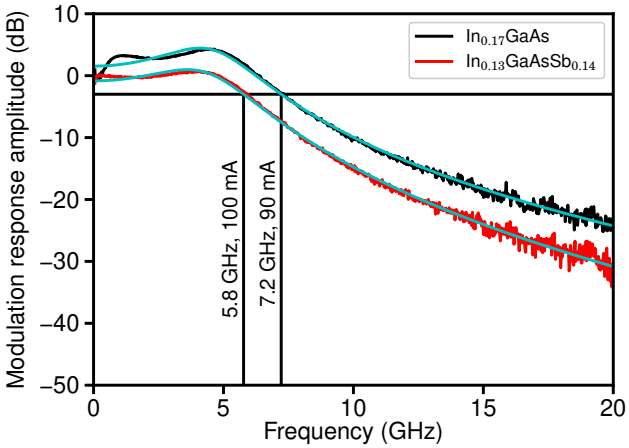

Figure 5.9: Small-signal response curves with maximum -3-dB bandwidth for the two investigated lasers.

during SML growth, a D-factor of 0.626±0.008 GHz/$\sqrt{mA}$ was extracted, while for the laser with Sb, a value of 0.534±0.002 GHz/$\sqrt{mA}$ was found. By neglecting transport effects ($\chi \sim 1$), the differential gain can be extracted using (2.39), showing a decrease from (5.11±0.21)·10^{-16} cm^{-2} to (3.26±0.28)·10^{-16} cm^{-2}.

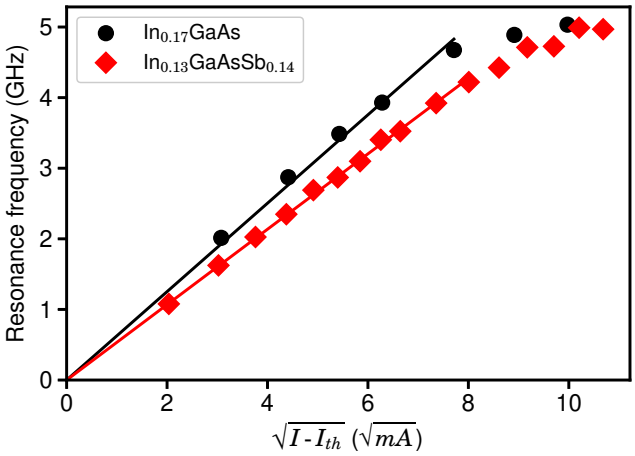

Figure 5.10: Resonance frequency with respect to the square root of the bias current above threshold. Symbols are extracted from S21 measurements, solid lines are fits to (2.38) to determine the D-factor.

Another figure of merit, the K-factor, can be obtained from the damping factor vs the squared resonance frequency (see (2.40)). Here an increase from 0.810±0.014 ns

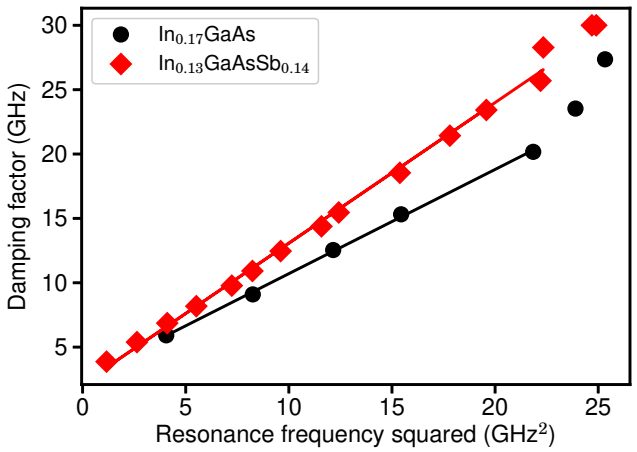

Figure 5.11: Damping factor vs squared resonance frequency. Solid lines are obtained by fitting (2.40) to the data determined from small-signal measurements (symbols).

to 1.092±0.024 ns was found. By using the group velocity as extracted before, the resulting photon lifetime, and the differential gain as obtained from the D-factor, the gain compression factor could be calculated. The addition of Sb changes the gain compression only slightly from (5.402±0.33)·10^{-17} cm^3 to (5.28±0.50)·10^{-17} cm^3.

Finally, the MCEF was extracted by plotting the -3-dB frequency with respect to the square root of the current above threshold. The addition of Sb decreases this value it from 0.887±0.016 GHz/$\sqrt{mA}$ to 0.726±0.005 GHz/$\sqrt{mA}$.

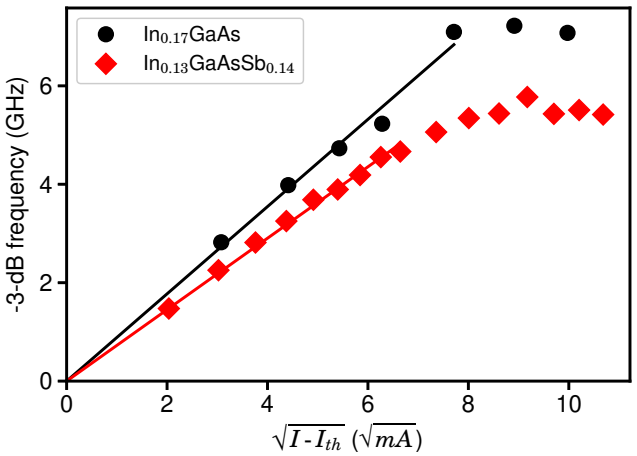

Figure 5.12: Determination of the MCEF from comparing -3-dB frequency vs square root of the bias current above threshold.

Table 5.4: Internal parameters obtained from the narrow-stripe lasers

	$In_{0.17}GaAs$	$In_{0.13}GaAsSb_{0.14}$
D-factor (GHz/$\sqrt{mA}$)	0.626±0.008	0.534±0.002
K-factor (ns)	0.810±0.014	1.092±0.024
MCEF (GHz/$\sqrt{mA}$)	0.887±0.016	0.726±0.005
$\partial g/\partial n$ (10^{-16} cm^2)	5.11±0.21	3.26±0.28
τ_p (ps)	6.48±0.52	6.27±0.58
ε (10^{-17} cm^3)	5.40±0.33	5.28±0.50

The results from the small-signal modulation measurements are summarized in table 5.4. Overall, the small-signal performance declines upon the addition of Sb. Similar to before, this can be explained by gain distribution over a large spectral range and the reduced optical confinement factor. For broad gain spectra as in the Sb-containing device, charge carriers can also recombine at energies not in resonance with the lasing modes, thus decreasing the overall modulation efficiency.

5.2.2 Large-signal modulation

As a final test, large signal modulation experiments were performed with the lasers. The used PRBS sequence has a length of 2^7-1 bit. Both lasers were compared at working points yielding comparable -3-dB frequencies (58 mA for the laser without Sb and 110 mA for the laser with Sb).

All laser showed signal overshoots and high intensity noise when using the 45-GHz single mode detector as in the small-signal measurements, even at the lower bit rate limit of the Bit Pattern Generator of 6 Gbit/s. Therefore the detector unit was replaced with a custom made 28-GHz limiting photoreceiver to enable a comparison of the lasers in terms of achievable bit rate. A maximum error-free bit rate of 12.5 Gbit/s and a signal-to-noise-ratio (SNR) of 3.4 at a drive current of 58 mA was achieved for the laser without Sb. The laser with Sb reached 17 Gbit/s and a SNR of 2.8 at a drive current of 110 mA. The corresponding error curves and eye diagrams are shown in Fig. 5.13.

The larger drive current of the Sb-containing laser also corresponds to a larger output power. Assuming all of the light emitted from one facet is collected by the tapered fiber, the output power of the laser with InAs/GaAs SML active region was ∼24 mW whereas the laser with InAsSb/GaAs submonolayer stack emitted

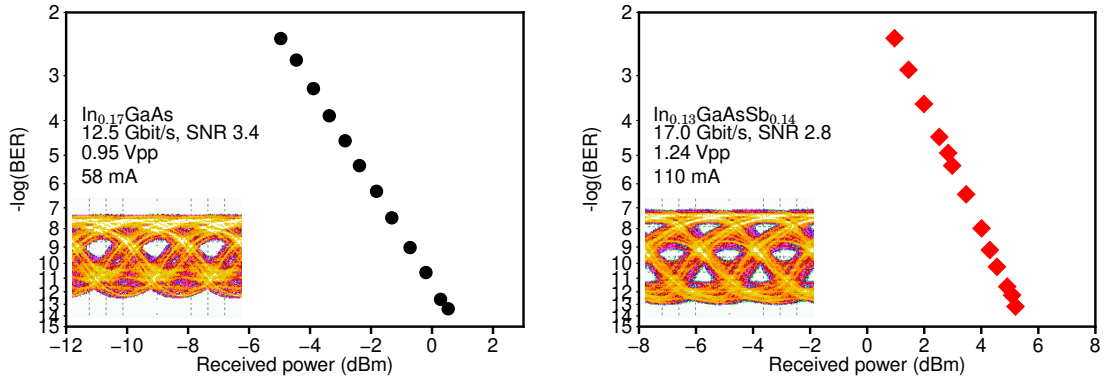

Figure 5.13: BER curves and eye diagrams obtained from the narrow-stripe lasers.

∼42 mW (compare Fig. 5.6). Additionally a larger voltage swing had to be used for the Sb-containing laser (0.95 Vpp to 1.24 Vpp, see Fig. 5.13).

Therefore, the larger bit rate is primarily achieved due to the higher signal at the photoreceiver. Operating the laser without Sb at a sufficiently large drive current and voltage swing should therefore enable larger bit rates.

6 Conclusion

Summary

With the use of an TESb flush, a method for altering the electronic confinement in InAs/GaAs SML stacks has been developed and successfully applied to edge-emitting directly modulated laser diodes. The detailed structural and optical analysis of the Sb incorporation allowed to develop an analytical model for the incorporation behavior and to control the degree of confinement and inhomogeneous broadening of the emission which was then introduced into the active region design of laser diodes. Such devices were compared for static and dynamic characteristics with regard to active region design.

By combining results from XRD and GIXRF measurements, the total amount of incorporated Sb could be determined. For short TESb supply times the incorporation behavior was found to follow Langmuir-type adsorption. At longer time scales, however, parasitic reactor effects need to be taken into account. To fully model the behavior, two additional reaction components are necessary and a difference between the reaction constants of a factor of >600 was found. Moreover, a growth rate reduction upon addition of TESb to the growth sequence was observed.

XSTM measurements showed a preferential Sb incorporation into In-rich regions in the SML stacks. Resulting from the shift of local valence and conduction band edges a decreased transition energy, reduced wave function overlap, and increased dipole moment was predicted from eight-band k·p simulations for such incorporation behavior.

Analysis of temperature-dependent photoluminescence measurements using an extended lineshape model yielded results agreeing to the simulations, showing a redshift of emission wavelength and increase of Huang-Rhys factor. Furthermore, samples with large Sb contents exhibited an S-shape in the temperature-dependent PL peak energy positions and individual emission lines in spatially resolved CL measurements, thus confirming the enhanced charge carrier localization.

In addition to the supplied TESb amount, the thickness of the GaAs spacer and number of deposition cycles have been identified as tuning parameters for the optical and electronic properties. A maximum spacer thickness for the presence of strong charge carrier localization of 1.8 to 1.9 ML GaAs was found, suggesting a critical local Sb atom density.

Using these three parameters, the optical properties of SML stacks can be adjusted to the target application. PL wavelength and FWHM could be independently tuned in a range of 900 to 1180 nm and 10 to 50 nm, respectively.

After analysis of the fundamental properties, the application in edge-emitting lasers has been investigated. Length-dependent measurements on broad-area lasers show a strong increase of the material gain at the cost of increased internal losses and transparency current density.

An investigation of spectrally resolved gain curves using narrow-stripe laser shows an increase of the gain bandwidth by about 50% and confirms that Sb leads to an increase in material gain.

The increase of both internal losses and threshold current can be explained by the decreased confinement factor which limits the modal gain, gain distribution over a larger spectral range causing a decrease of the peak gain and large density of localization centers which have to be inverted before contributing to the lasing process.

Finally, the modulation capabilities of the narrow-stripe lasers were investigated. A decrease of -3-dB bandwidth was determined for the Sb-containing device from small-signal measurements. In large-signal measurements, a larger bit rate could be achieved using the laser with Sb when both lasers were driven at working points with similar -3-dB bandwidths. However, this was primarily caused by the difference in optical output power.

In summary, InAs/GaAs SML stacks without Sb seem to be more suitable for the application in directly modulated lasers. While SML stack characteristics can be successfully tuned from QW- to QD-like by using Sb, the very high density of localization centers and broad gain distribution incur drawbacks in the form of increased drive currents and modulation swings.

Suggestions for further research

Using the presented work as a basis, further investigations of Sb-containing InAs/GaAs SML stacks could be performed.

Using the proposed incorporation model the influence of growth parameters (growth temperature, reactor pressure, growth rates, etc.) on the incorporation behavior of Sb could be investigated.

Additionally, the maximum wavelength achieved in this thesis is 1180 nm, limited by defect formation. As conventional Stranski-Krastanov In(Ga)GaAs high-density quantum dot ensembles have been shown to reach emission wavelengths of up to 1320 nm [51–53], it would be interesting to see if the SML growth mode is also an alternative for the fabrication of high QD densities emitting in this spectral range.

Using the approach of this thesis, the application in devices for which broad gain spectra are advantageous, e.g. semiconductor optical amplifiers, mode-locked lasers, and temperature-stable VCSELS, could be investigated.

Furthermore, only single SML stacks have been used in this work. As no 2D-3D transition occurs during SML growth, requirements concerning the spacer thickness between SML stacks might be less strict compared to multiple layers of SK-QDs, thus potentially allowing for larger optical confinement factors and modal gains.

Finally, the performance of directly modulated lasers using Sb-containing SML stacks is limited by the very high density 0D localization centers. As simulations suggest an optimal density in the low 10^{11} cm^{-2} range, the ability to tune the density of In-rich regions in the SML stack would be of interest.

Bibliography

[1] P. Savolainen et al. “Red lasers grown by all-solid-source molecular beam epitaxy”. In: *Semiconductor Science and Technology* **14**, p. 425 (1999) (cit. on p. 1).

[2] A. Knigge, M. Zorn, A. Weyers, and G. Tränkle. “High-performance vertical-cavity surface-emitting lasers with emission wavelength between 650 and 670 nm”. In: *Electronics Letters* **38**, p. 882 (2002) (cit. on p. 1).

[3] M. A. Emanuel, J. A. Skidmore, M. Jansen, and R. Nabiev. “High-Power InAlGaAs-GaAs Laser Diode Emitting Near 731 nm”. In: *IEEE Photonics Technology Letters* **9**, p. 1451 (1997) (cit. on p. 1).

[4] Thomas J. Dougherty et al. “Photodynamic therapy”. In: *JNCI: Journal of the National Cancer Institute* **90**, p. 889 (1998) (cit. on p. 1).

[5] L. J. Mawst, S. Rusli, A. Al-Muhanna, and J. K. Wade. “Short-Wavelength (0.7 µm $< \lambda <$ 0.78 µm) High-Power InGaAsP-Active Diode Lasers”. In: *IEEE Journal of Selected Topics in Quantum Electronics* **5**, p. 785 (1999) (cit. on p. 1).

[6] Bingkun Zhou, Thomas J. Kane, George J. Dixon, and Robert L. Byer. “Efficient, frequency-stable laser-diode-pumped Nd:YAG laser”. In: *Optics Letters* **10**, p. 62 (1985) (cit. on p. 1).

[7] G. T. Maker and A. I. Ferguson. “Frequency modulation mode-locking and Q-switching of diode-laser-pumped Nd:YLF laser”. In: *Electronics Letters* **25**, p. 1025 (1989) (cit. on p. 1).

[8] Kimio Shigihara et al. “High-Power Operation of Broad-Area Laser Diodes with GaAs and AlGaAs Single Quantum Wells for Nd:YAG Laser Pumping”. In: *IEEE Journal of Quantum Electronics* **27**, p. 1537 (1991) (cit. on p. 1).

[9] M. Grabherr et al. “Efficient Single-Mode Oxide-Confined GaAs VCSEL’s Emitting in the 850-nm Wavelength Regime”. In: *IEEE Photonics Technology Letters* **9**, p. 1304 (1997) (cit. on p. 1).

[10] R. Jäger et al. “57% wallplug efficiency oxide-confined 850 nm wavelength GaAs VCSELs”. In: *Electronics Letters* **33**, p. 330 (1997) (cit. on p. 1).

[11] T. E. Sale, C. Amamo, Y. Ohiso, and T. Kurokawa. “Using strained $(Al_xGa_{1-x})_yIn_{1-y}As_zP_{1-z}$ system materials to improve the performance of 850 nm surface- and edge-emitting lasers”. In: *Applied Physics Letters* **71**, p. 1002 (1997) (cit. on p. 1).

[12] H.C. Kuo, Y.S. Chang, C.F. Lin, T.C. Lu, and S.C. Wang. “MOCVD growth of high-performance InGaAsP/InGaP strain-compensated VCSELs with 850 nm emission wavelength”. In: *Journal of Crystal Growth* **261**, p. 355 (2004) (cit. on p. 1).

[13] S. A. Blokhin et al. “Oxide-confined 850 nm VCSELs operating at bit rates up to 40 Gbit/s”. In: *Electronics Letters* **45**, p. 501 (2009) (cit. on p. 1).

[14] P. Westbergh et al. “High-Speed, Low-Current-Density 850 nm VCSELs”. In: *IEEE Journal of Selected Topics in Quantum Electronics* **15**, p. 694 (2009) (cit. on p. 1).

[15] Petter Westbergh et al. “40 Gbit/s error-free operation of oxide-confined 850 nm VCSEL”. In: *Electronics Letters* **46**, p. 1014 (2010) (cit. on p. 1).

[16] J. S. Major, W. E. Plano, D. F. Welch, and D. Scifres. “Single-mode InGaAs-GaAs laser diodes operating at 980 nm”. In: *Electronics Letters* **27**, p. 539 (1991) (cit. on p. 1).

[17] B. Pedersen, B. A. Thompson, S. Zemon, W. J. Miniscalco, and T. Wei. “Power Requirements for Erbium-Doped Fiber Amplifiers Pumped in the 800, 980, and 1480 nm Bands”. In: *IEEE Photonics Technology Letters* **4**, p. 46 (1992) (cit. on p. 1).

[18] L.A. BuckmanWindover et al. “Parallel-Optical Interconnects > 100 Gb/s”. In: *Journal of Lightwave Technology* **22**, p. 2055 (2004) (cit. on pp. 1, 77).

[19] L. Schares et al. “Terabus: Terabit/Second-Class Card-Level Optical Interconnect Technologies”. In: *IEEE Journal of Selected Topics in Quantum Electronics* **12**, p. 1032 (2006) (cit. on pp. 1, 77).

[20] Chao-Kun Lin, Ashish Tandon, Kostadin Djordjev, Scott W. Corzine, and Michael R. T. Tan. "High-Speed 985 nm Bottom-Emitting VCSEL Arrays for Chip-to-Chip Parallel Optical Interconnects". In: *IEEE Journal of Selected Topics in Quantum Electronics* **13**, p. 1332 (2007) (cit. on pp. 1, 77).

[21] A. Mutig et al. "120°C 20 Gbit/s operation of 980 nm VCSEL". In: *Electronics Letters* **44**, p. 1305 (2008) (cit. on pp. 1, 77).

[22] Alex Mutig and Dieter Bimberg. "Progress on High-Speed 980 nm VCSELs for Short-Reach Optical Interconnects". In: *Advances in Optical Technologies* **2011**, p. 1 (2011) (cit. on p. 1).

[23] A. Mutig et al. "Modulation Characteristics of High-Speed and High-Temperature Stable 980 nm Range VCSELs Operating Error Free at 25 Gbit/s up to 85 °C". In: *IEEE Journal of Selected Topics in Quantum Electronics* **17**, p. 1568 (2011) (cit. on pp. 1, 77).

[24] Hideyuki Nasu. "Short-Reach Optical Interconnects Employing High-Density Parallel-Optical Modules". In: *IEEE Journal of Selected Topics in Quantum Electronics* **16**, p. 1337 (2010) (cit. on p. 1).

[25] A. Larsson et al. "1060 nm VCSELs for long-reach optical interconnects". In: *Optical Fiber Technology* (2018) (cit. on p. 1).

[26] Benjamin Potsaid et al. "Ultrahigh speed 1050nm swept source / Fourier domain OCT retinal and anterior segment imaging at 100,000 to 400,000 axial scans per second". In: *Optics Express* **18**, p. 20029 (2010) (cit. on p. 1).

[27] V. Jayaraman et al. "Rapidly swept, ultra-widely-tunable 1060 nm MEMS-VCSELs". In: *Electronics Letters* **48**, p. 1331 (2012) (cit. on p. 1).

[28] Thor Ansbaek, Il-Sug Chung, Elizaveta S. Semenova, Ole Hansen, and Kresten Yvind. "Resonant MEMS Tunable VCSEL". In: *IEEE Journal of Selected Topics in Quantum Electronics* **19**, p. 1702306 (2013) (cit. on p. 1).

[29] F. Bugge et al. "Growth of laser diode structures with emission wavelength beyond 1100 nm for yellow–green emission by frequency conversion". In: *Journal of Crystal Growth* **414**, p. 205 (2015) (cit. on p. 1).

[30] T. K. Sharma et al. "High-Power Highly Strained InGaAs Quantum-Well Lasers Operating at 1.2 µm". In: *IEEE Photonics Technology Letters* **14**, p. 887 (2002) (cit. on p. 1).

[31] T. K. Sharma et al. “Highly strained InGaAs/GaAs quantum wells emitting beyond 1.2 µm”. In: *Crystal Research and Technology* **40**, p. 877 (2005) (cit. on pp. 1, 7).

[32] M. Horiguchi and H. Osanai. “Spectral losses of low-OH-content optical fibres”. In: *Electronics Letters* **12**, p. 310 (1976) (cit. on p. 1).

[33] Terenuma Miya, Y. Terunuma, Tatsuya Hosaka, and Tadakazu Miyashita. “Ultimate low-loss single-mode fibre at 1.55 µm”. In: *Electronics Letters* **15**, p. 106 (1979) (cit. on p. 1).

[34] K. D. Choquette et al. “Room temperature continuous wave InGaAsN quantum well vertical-cavity lasers emitting at 1.3 µm”. In: *Electronics Letters* **36**, p. 1388 (2000) (cit. on p. 1).

[35] J. S. Harris. “GaInNAs long-wavelength lasers: progress and challenges”. In: *Semiconductor Science and Technology* **17**, p. 880 (2002) (cit. on p. 1).

[36] G. Jaschke, R. Averbeck, L. Geelhaar, and H. Riechert. “Low threshold InGaAsN/GaAs lasers beyond 1500nm”. In: *Journal of Crystal Growth* **278**, p. 2248 (2005) (cit. on p. 1).

[37] N. Laurand et al. “C-band emission from GaInNAsSb VCSEL on GaAs”. In: *Electronics Letters* **42**, p. 29 (2006) (cit. on p. 1).

[38] M. A. Wistey et al. “GaInNAsSb/GaAs vertical cavity surface emitting lasers at 1534 nm”. In: *Electronics Letters* **42**, p. 282 (2006) (cit. on p. 1).

[39] G. Thompson and P. Kirkby. “(GaAl)As Lasers With a Heterostructure for Optical Confinement and Additional Heterojunctions for Extreme Carrier Confinement”. In: *IEEE Journal of Quantum Electronics* **9**, p. 311 (1973) (cit. on p. 1).

[40] G. H. B. Thompson, G. D. Henshall, J. E. A. Whiteaway, and P. A. Kirkby. “Narrow-beam five-layer (GaAl)As/GaAs heterostructure lasers with low threshold and high peak power”. In: *Journal of Applied Physics* **47**, p. 1501 (1976) (cit. on p. 1).

[41] W. T. Tsang. “Symmetric Separate Confinement Heterostructure Lasers with Low Threshold and Narrow Beam Divergence by M.B.E.” In: *Electronics Letters* **16**, p. 939 (1980) (cit. on p. 1).

[42] Raymond Dingle, William Wiegmann, and Charles H. Henry. "Quantum States of Confined Carriers in Very Thin $Al_xGa_{1-x}As$-GaAs-$Al_xGa_{1-x}As$ Heterostructures". In: *Physical Review Letters* **33**, p. 827 (1974) (cit. on p. 1).

[43] J. P. van der Ziel, R. Dingle, R. C. Miller, W. Wiegmann, and W. A. Nordland. "Laser oscillation from quantum states in very thin GaAs-$Al_{0.2}Ga_{0.8}As$ multilayer structures". In: *Applied Physics Letters* **26**, p. 463 (1975) (cit. on p. 1).

[44] Peter S. Zory, ed. *Quantum well lasers*. Quantum electronics - principles and applications. Academic Press, 1993 (cit. on p. 1).

[45] Sadao Adachi. *Properties of Group-IV, III-V and II-VI semiconductors*. eng. Wiley Series in Materials for Electronic & Optoelectronic Applications. Chichester: Wiley, 2006 (cit. on pp. 1, 6, 59).

[46] Y. Arakawa and H. Sakaki. "Multidimensional quantum well laser and temperature dependence of its threshold current". In: *Applied Physics Letters* **40**, p. 939 (1982) (cit. on pp. 2, 8).

[47] M. Asada, Y. Miyamoto, and Y. Suematsu. "Gain and the Threshold of Three-Dimensional Quantum-Box Lasers". In: *IEEE Journal of Quantum Electronics* **22**, p. 1915 (1986) (cit. on pp. 2, 8).

[48] I. N. Stranski and L. Krastanow. "Zur Theorie der orientierten Ausscheidung von Ionenkristallen aufeinander". In: *Monatshefte für Chemie* **71**, p. 351 (1938) (cit. on pp. 2, 7).

[49] Ernst Bauer. "Phänomenologische Theorie der Kristallabscheidung an Oberflächen. I". In: *Zeitschrift für Kristallographie* **110**, p. 372 (1958) (cit. on pp. 2, 6).

[50] Frank Heinrichsdorff. "MOCVD growth and laser applications of In(Ga)As-GaAs Quantum Dots". PhD thesis. Technische Universität Berlin, 1998 (cit. on pp. 2, 11, 26).

[51] A. Passaseo et al. "Long wavelength emission in $In_xGa_{1-x}As$ quantum dot structures grown in a GaAs barrier by metalorganic chemical vapor deposition". In: *Applied Physics Letters* **84**, p. 1868 (2004) (cit. on pp. 2, 93).

[52] A. Passaseo et al. “Tuning of long-wavelength emission in $In_xGa_{1-x}As$ quantum dot structures”. In: *Physica E: Low-dimensional Systems and Nanostructures* **23**, p. 390 (2004) (cit. on pp. 2, 93).

[53] Denis Guimard et al. “Ground state lasing at 1.30 µm from InAs/GaAs quantum dot lasers grown by metal–organic chemical vapor deposition”. In: *Nanotechnology* **21**, p. 105604 (2010) (cit. on pp. 2, 93).

[54] Jun Tatebayashi, Masao Nishioka, and Yasuhiko Arakawa. “Over 1.5 µm light emission from InAs quantum dots embedded in InGaAs strain-reducing layer grown by metalorganic chemical vapor deposition”. In: *Applied Physics Letters* **78**, p. 3469 (2001) (cit. on p. 2).

[55] M. Kuntz et al. “Direct modulation and mode locking of 1.3 µm quantum dot lasers”. In: *New Journal of Physics* **6**, p. 181 (2004) (cit. on p. 2).

[56] D. Bimberg et al. “High speed nanophotonic devices based on quantum dots”. In: *physica status solidi (a)* **203**, p. 3523 (2006) (cit. on p. 2).

[57] Dejan Arsenijević, Moritz Kleinert, and Dieter Bimberg. “Breakthroughs in Photonics 2013: Passive Mode-Locking of Quantum-Dot Lasers”. In: *IEEE Photonics Journal* **6**, p. 1 (2014) (cit. on p. 2).

[58] M. Kuntz et al. “35 GHz mode-locking of 1.3µm quantum dot lasers”. In: *Applied Physics Letters* **85**, p. 843 (2004) (cit. on p. 2).

[59] M. Laemmlin et al. “Distortion-free optical amplification of 20–80 GHz modelocked laser pulses at 1.3 µm using quantum dots”. In: *Electronics Letters* **42**, p. 697 (2006) (cit. on p. 2).

[60] G. Fiol et al. “Quantum-Dot Semiconductor Mode-Locked Lasers and Amplifiers at 40 GHz”. In: *IEEE Journal of Quantum Electronics* **45**, pp. 1429–1435 (2009) (cit. on p. 2).

[61] G. Fiol et al. “Hybrid mode-locking in a 40 GHz monolithic quantum dot laser”. In: *Applied Physics Letters* **96**, p. 011104 (2010) (cit. on p. 2).

[62] G. Fiol, M. Kleinert, D. Arsenijević, and D. Bimberg. “1.3 µm range 40 GHz quantum-dot mode-locked laser under external continuous wave light injection or optical feedback”. In: *Semiconductor Science and Technology* **26**, p. 014006 (2011) (cit. on p. 2).

[63] D. Arsenijević, M. Kleinert, and D. Bimberg. "Phase noise and jitter reduction by optical feedback on passively mode-locked quantum-dot lasers". In: *Applied Physics Letters* **103**, p. 231101 (2013) (cit. on p. 2).

[64] M. Stubenrauch, G. Stracke, D. Arsenijević, A. Strittmatter, and D. Bimberg. "15 Gb/s index-coupled distributed-feedback lasers based on 1.3 µm InGaAs quantum dots". In: *Applied Physics Letters* **105**, p. 011103 (2014) (cit. on p. 2).

[65] C. Meuer et al. "40 GHz small-signal cross-gain modulation in 1.3 µm quantum dot semiconductor optical amplifiers". In: *Applied Physics Letters* **93**, p. 051110 (2008) (cit. on p. 2).

[66] Christian Meuer et al. "Static gain saturation in quantum dot semiconductor optical amplifiers". In: *Optics Express* **16**, p. 8269 (2008) (cit. on p. 2).

[67] Christian Meuer et al. "High-Speed Small-Signal Cross-Gain Modulation in Quantum-Dot Semiconductor Optical Amplifiers at 1.3 µm". In: *IEEE Journal of Selected Topics in Quantum Electronics* **15**, p. 749 (2009) (cit. on p. 2).

[68] C. Meuer et al. "Cross-Gain Modulation and Four-Wave Mixing for Wavelength Conversion in Undoped and p-Doped 1.3-µm Quantum Dot Semiconductor Optical Amplifiers". In: *IEEE Photonics Journal* **2**, p. 141 (2010) (cit. on p. 2).

[69] H. Schmeckebier, G. Fiol, C. Meuer, D. Arsenijević, and D. Bimberg. "Complete pulse characterization of quantum dot mode-locked lasers suitable for optical communication up to 160 Gbit/s". In: *Optics Express* **18**, p. 3415 (2010) (cit. on p. 2).

[70] Christian Meuer et al. "80 Gb/s wavelength conversion using a quantum-dot semiconductor optical amplifier and optical filtering". In: *Optics Express* **19**, p. 5134 (2011) (cit. on p. 2).

[71] Christian Meuer et al. "40 Gb/s wavelength conversion via four-wave mixing in a quantum-dot semiconductor optical amplifier". In: *Optics Express* **19**, p. 3788 (2011) (cit. on p. 2).

[72] Holger Schmeckebier et al. “Quantum dot semiconductor optical amplifiers at 1.3 µm for applications in all-optical communication networks”. In: *Semiconductor Science and Technology* **26**, p. 014009 (2011) (cit. on p. 2).

[73] Holger Schmeckebier et al. “Wide-Range Wavelength Conversion of 40-Gb/s NRZ-DPSK Signals Using a 1.3-µm Quantum-Dot Semiconductor Optical Amplifier”. In: *IEEE Photonics Technology Letters* **24**, p. 1163 (2012) (cit. on p. 2).

[74] F. Hopfer et al. “Vertical-cavity surface-emitting quantum-dot laser with low threshold current grown by metal-organic vapor phase epitaxy”. In: *Applied Physics Letters* **89**, p. 061105 (2006) (cit. on p. 2).

[75] A. Strittmatter et al. “1040 nm vertical external cavity surface emitting laser based on InGaAs quantum dots grown in Stranski-Krastanow regime”. In: *Electronics Letters* **44**, p. 290 (2008) (cit. on p. 2).

[76] Qianghua Xie, Anupam Madhukar, Ping Chen, and Nobuhiko P. Kobayashi. “Vertically Self-Organized InAs Quantum Box Islands on GaAs(100)”. In: *Physical Review Letters* **75**, p. 2542 (1995) (cit. on pp. 2, 7).

[77] S. Ruvimov et al. “Structural characterization of (In,Ga)As quantum dots in a GaAs matrix”. In: *Physical Review B* **51**, p. 14766 (1995) (cit. on pp. 2, 7).

[78] D. Bimberg et al. “InGaAs-GaAs quantum-dot lasers”. In: *IEEE Journal of Selected Topics in Quantum Electronics* **3**, p. 196 (1997) (cit. on pp. 2, 7, 8).

[79] H. Eisele et al. “Cross-sectional scanning-tunneling microscopy of stacked InAs quantum dots”. In: *Applied Physics Letters* **75**, p. 106 (1999) (cit. on pp. 2, 7).

[80] B. Lita, R. S. Goldman, J. D. Phillips, and P. K. Bhattacharya. “Nanometer-scale studies of vertical organization and evolution of stacked self-assembled InAs/GaAs quantum dots”. In: *Applied Physics Letters* **74**, p. 2824 (1999) (cit. on pp. 2, 7).

[81] D. M. Bruls et al. “Determination of the shape and indium distribution of low-growth-rate InAs quantum dots by cross-sectional scanning tunneling microscopy”. In: *Applied Physics Letters* **81**, p. 1708 (2002) (cit. on pp. 2, 7, 8).

[82] J. H. Blokland et al. "Ellipsoidal InAs quantum dots observed by cross-sectional scanning tunneling microscopy". In: *Applied Physics Letters* **94**, p. 023107 (2009) (cit. on pp. 2, 7).

[83] S. Gaan, Guowei He, R. M. Feenstra, J. Walker, and E. Towe. "Size, shape, composition, and electronic properties of InAs/GaAs quantum dots by scanning tunneling microscopy and spectroscopy". In: *Journal of Applied Physics* **108**, p. 114315 (2010) (cit. on pp. 2, 7).

[84] Andrea Lenz et al. "Atomic Structure of Buried InAs Sub-Monolayer Depositions in GaAs". In: *Applied Physics Express* **3**, p. 105602 (2010) (cit. on pp. 2, 9, 56).

[85] Andrea Lenz et al. "Atomic structure and optical properties of InAs submonolayer depositions in GaAs". In: *Journal of Vacuum Science and Technology B* **29**, p. 04D104 (2011) (cit. on pp. 2, 9, 34, 41, 56).

[86] T. D. Germann et al. "High-power semiconductor disk laser based on InAs/GaAs submonolayer quantum dots". In: *Applied Physics Letters* **92**, p. 101123 (2008) (cit. on pp. 2, 11, 26).

[87] A. E. Zhukov et al. "3.9 W CW power from sub-monolayer quantum dot diode laser". In: *Electronics Letters* **35**, p. 1845 (1999) (cit. on pp. 2, 11).

[88] F. Hopfer et al. "Single-mode submonolayer quantum-dot vertical-cavity surface-emitting lasers with high modulation bandwidth". In: *Applied Physics Letters* **89**, p. 141106 (2006) (cit. on p. 2).

[89] Friedhelm Hopfer et al. "20 Gb/s 85°C Error-Free Operation of VCSELs Based on Submonolayer Deposition of Quantum Dots". In: *IEEE Journal of Selected Topics in Quantum Electronics* **13**, p. 1302 (2007) (cit. on pp. 2, 11).

[90] N. N. Ledentsov et al. "Submonolayer Quantum Dots for High Speed Surface Emitting Lasers". In: *Nanoscale Research Letters* **2**, p. 417 (2007) (cit. on pp. 2, 11).

[91] A. Mutig et al. "Temperature-Dependent Small-Signal Analysis of High-Speed High-Temperature Stable 980-nm VCSELs". In: *IEEE Journal of Selected Topics in Quantum Electronics* **15**, p. 679 (2009) (cit. on pp. 2, 11, 77).

[92] Zhangcheng Xu et al. “InGaAs/GaAs quantum-dot–quantum-well heterostructure formed by submonolayer deposition”. In: *Nanotechnology* **14**, p. 1259 (2003) (cit. on pp. 2, 10, 34).

[93] Oliver Stier, Marius Grundmann, and Dieter Bimberg. “Electronic and optical properties of strained quantum dots modeled by 8-band k·p theory”. In: *Physical Review B* **59**, p. 5688 (1999) (cit. on pp. 2, 8, 41, 42).

[94] S. Harrison et al. “Heterodimensional charge-carrier confinement in stacked submonolayer InAs in GaAs”. In: *Physical Review B* **93**, p. 085302 (2016) (cit. on pp. 3, 10, 34, 43).

[95] Vladimir V. Mitin, Viatcheslav A. Kočelap, and Michael A. Stroscio. *Introduction to Nanoelectronics: Science, Nanotechnology, Engineering, and Applications*. Cambridge University Press, 2008 (cit. on p. 6).

[96] I. Vurgaftman, J. R. Meyer, and L. R. Ram-Mohan. “Band parameters for III-V compound semiconductors and their alloys”. In: *Journal of Applied Physics* **89**, p. 5815 (2001) (cit. on pp. 6, 11, 12, 35).

[97] F. C. Frank and J. H. van der Merwe. “One-Dimensional Dislocations. I. Static Theory”. In: *Proceedings of the Royal Society A: Mathematical, Physical and Engineering Sciences* **198**, p. 205 (1949) (cit. on p. 7).

[98] J. W. Matthews and A. E. Blakeslee. “Defects in epitaxial multilayers I. Misfit dislocations”. In: *Journal of Crystal Growth* **27**, p. 118 (1974) (cit. on p. 7).

[99] R. People and J. C. Bean. “Calculation of critical layer thickness versus lattice mismatch for Ge_xSi_{1-x}/S strained-layer heterostructures”. In: *Applied Physics Letters* **47**, p. 322 (1985) (cit. on p. 7).

[100] M. J. Ekenstedt, S. M. Wang, and T. G. Andersson. “Temperature-dependent critical layer thickness for $In_{0.36}Ga_{0.64}As$/GaAs single quantum wells”. In: *Applied Physics Letters* **58**, p. 854 (1991) (cit. on p. 7).

[101] D. Schlenker et al. “Critical layer thickness of 1.2-μm highly strained GaInAs/GaAs quantum wells”. In: *Journal of Crystal Growth* **221**, p. 503 (2000) (cit. on p. 7).

[102] M. Volmer and A. Weber. “Keimbildung in übersättigten Gebilden”. In: *Zeitschrift für Physikalische Chemie* **119U**, p. 277 (1926) (cit. on p. 7).

[103] R. Leon et al. "Self-forming InAs/GaP quantum dots by direct island growth". In: *Applied Physics Letters* **72**, p. 1356 (1998) (cit. on p. 7).

[104] H. Eisele et al. "Change of InAs/GaAs quantum dot shape and composition during capping". In: *Journal of Applied Physics* **104**, p. 124301 (2008) (cit. on pp. 7, 8).

[105] M. Grundmann et al. "Ultranarrow Luminescence Lines from Single Quantum Dots". In: *Physical Review Letters* **74**, p. 4043 (1995) (cit. on p. 7).

[106] M. Grundmann, O. Stier, and D. Bimberg. "InAs/GaAs pyramidal quantum dots: Strain distribution, optical phonons, and electronic structure". In: *Physical Review B* **52**, p. 11969 (1995) (cit. on p. 8).

[107] Oliver Stier. "Electronic and Optical Properties of Quantum Dots and Wires". eng. PhD thesis. Technische Universität Berlin, 2001 (cit. on p. 8).

[108] B. Henderson and G. F. Imbusch. *Optical Spectroscopy of Inorganic Solids*. Monographs on the physics and chemistry of materials. Clarendon Press, Oxford University Press, 1989 (cit. on pp. 8, 59).

[109] Lorenzo Pavesi and Mario Guzzi. "Photoluminescence of $Al_xGa_{1-x}As$ alloys". In: *Journal of Applied Physics* **75**, p. 4779 (1994) (cit. on pp. 8, 59).

[110] R. Heitz, I. Mukhametzhanov, O. Stier, A. Madhukar, and D. Bimberg. "Enhanced Polar Exciton-LO-Phonon Interaction in Quantum Dots". In: *Physical Review Letters* **83**, p. 4654 (1999) (cit. on pp. 8, 59, 63).

[111] R. Heitz et al. "Resonant Raman scattering in self-organized InAs/GaAs quantum dots". In: *Applied Physics Letters* **77**, p. 3746 (2000) (cit. on pp. 8, 59, 63).

[112] K. Huang and A. Rhys. "Theory of light absorption and non-radiative transitions in F-centres". In: *Proceedings of the Royal Society A: Mathematical, Physical and Engineering Sciences* **204**, p. 406 (1950) (cit. on p. 8).

[113] Nomura Shintaro and Kobayashi Takayoshi. "Exciton-LO-Phonon couplings in spherical semiconductor microcrystallites". In: *Physical Review B* **45**, p. 1305 (1992) (cit. on p. 8).

[114] N. Kirstaedter et al. "Gain and differential gain of single layer InAs/GaAs quantum dot injection lasers". In: *Applied Physics Letters* **69**, p. 1226 (1996) (cit. on p. 8).

[115] Mikhail V. Maximov et al. "InGaAs/GaAs Quantum Dot Lasers with Ultrahigh Characteristic Temperature (T_0 = 385 K) Grown by Metal Organic Chemical Vapour Deposition". In: *Japanese Journal of Applied Physics* **36**, p. 4221 (1997) (cit. on p. 8).

[116] F. Heinrichsdorff, M. Grundmann, O. Stier, A. Krost, and D. Bimberg. "Influence of In/Ga intermixing on the optical properties of InGaAs/GaAs quantum dots". In: *Journal of Crystal Growth* **195**, p. 540 (1998) (cit. on pp. 9, 27).

[117] J. G. Keizer, A. B. Henriques, A. D. B. Maia, A. A. Quivy, and P. M. Koenraad. "Atomically resolved study of the morphology change of InAs/GaAs quantum dot layers induced by rapid thermal annealing". In: *Applied Physics Letters* **101**, p. 243113 (2012) (cit. on pp. 9, 27).

[118] J. M. Gerard and J. Y. Marzin. "High quality ultrathin InAs/GaAs quantum wells grown by standard and low-temperature modulated-fluxes molecular beam epitaxy". In: *Applied Physics Letters* **53**, p. 568 (1988) (cit. on p. 9).

[119] O. Brandt et al. "Radiative decay of excitonic states in bulklike GaAs with a periodic array of InAs lattice planes". In: *Physical Review B* **42**, p. 11396 (1990) (cit. on p. 9).

[120] O. Brandt et al. "Structural and optical properties of (100) InAs single-monolayer quantum wells in bulklike GaAs grown by molecular-beam epitaxy". In: *Physical Review B* **41**, p. 12599 (1990) (cit. on p. 9).

[121] J. H. Lee, K. Y. Hsieh, and R. M. Kolbas. "Photoluminescence and stimulated emission from monolayer-thick pseudomorphic InAs single-quantum-well heterostructures". In: *Physical Review B* **41**, p. 7678 (1990) (cit. on p. 9).

[122] O. Brandt, H. Lage, and K. Ploog. "Excitons in InAs/GaAs submonolayer quantum wells". In: *Physical Review B* **43**, p. 14285 (1991) (cit. on p. 9).

[123] O. Brandt, H. Lage, G.C. La Rocca, A. Heberle, and K. Ploog. "Role of broken translational invariance for the optical response of excitons in low-dimensional semiconductors". In: *Surface Science* **267**, p. 319 (1992) (cit. on p. 9).

[124] Oliver Brandt, Matthias Ilg, and Klaus Ploog. "Coherently strained InAs insertions in GaAs: do they form quantum wires and dots?" In: *Microelectronics Journal* **26**, p. 861 (1995) (cit. on p. 9).

[125] Vitaliy A. Shchukin and Dieter Bimberg. "Spontaneous ordering of nanostructures on crystal surfaces". In: *Reviews of Modern Physics* **71**, p. 1125 (1999) (cit. on p. 9).

[126] Franziska Luckert. "MOCVD-Wachstum von Sub-Monolagen-Quantenpunkten". MA thesis. Technische Universität Berlin, 2008 (cit. on pp. 10, 11, 73).

[127] Konstantin Pötschke. "Untersuchungen zur Bildung von Quantenpunkten im Stranski-Krastanow und im Submonolagen Wachstumsmodus". PhD thesis. Technische Universität Berlin, 2009 (cit. on pp. 10, 11, 26, 34, 41, 57, 73).

[128] Zhangcheng Xu, Dan Birkedal, Michael Juhl, and Jørn M. Hvam. "Submonolayer InGaAs/GaAs quantum-dot lasers with high modal gain and zero-linewidth enhancement factor". In: *Applied Physics Letters* **85**, p. 3259 (2004) (cit. on p. 11).

[129] Bastian Herzog et al. "Fast gain and phase recovery of semiconductor optical amplifiers based on submonolayer quantum dots". In: *Applied Physics Letters* **107**, p. 201102 (2015) (cit. on p. 11).

[130] Benjamin Lingnau et al. "Ultrafast gain recovery and large nonlinear optical response in submonolayer quantum dots". In: *Physical Review B* **94**, p. 014305 (2016) (cit. on p. 11).

[131] Chris G. Van de Walle. "Band lineups and deformation potentials in the model-solid theory". In: *Physical review B* **39**, p. 1871 (1989) (cit. on p. 12).

[132] Irving Langmuir. "The constitution and fundamental properties of solids and liquids. Part I. Solids." In: *Journal of the American Chemical Society* **38**, p. 2221 (1916) (cit. on pp. 12, 41).

[133] Junichi Murota, Takashi Matsuura, and Masao Sakuraba. "Atomically controlled processing for group IV semiconductors". In: *Surface and Interface Analysis* **34**, p. 423 (2002) (cit. on pp. 13–15, 41).

[134] S. M. Sze and Kwok K. Ng. *Physics of Semiconductor Devices*. 3rd edition. Wiley-Interscience, 2007 (cit. on p. 16).

[135] Martin A. Afromowitz. "Refractive index of $Ga_{1-x}Al_xAs$". In: *Solid State Communications* **15**, p. 59 (1974) (cit. on p. 17).

[136] Kamran S. Mobarhan. *Test and Characterization of Laser Diodes: Determination of Principal Parameters*. Tech. rep. Newport, 1999 (cit. on p. 18).

[137] K. Petermann. *Laser Diode Modulation and Noise*. Springer Netherlands, 1988 (cit. on p. 19).

[138] Peter M. Smowton and Peter Blood. "The Differential Efficiency of Quantum-Well Lasers". In: *IEEE Journal of selected Topics in Quantum Electronics* **3**, p. 8 (1997) (cit. on p. 19).

[139] T. A. DeTemple and C. M. Herzinger. "On the Semiconductor Laser Logarithmic Gain-Current Density Relation". In: *IEEE Journal of Quantum Electronics* **29**, p. 1246 (1993) (cit. on p. 19).

[140] Julian S. Osinski, Piotr Grodzinski, Yao Zou, and P. Daniel Dapkus. "Threshold Current Analysis of Compressive Strain (0-1.8%) in Low-Threshold, Long-Wavelength Quantum Well Lasers". In: *IEEE Journal of Quantum Electronics* **29**, p. 1576 (1993) (cit. on p. 19).

[141] Nelson Tansu, Ying-Lan Chang, Tetsuya Takeuchi, David P. Bour, and Luke J. Mawst. "Temperature Analysis and Characteristics of Highly Strained InGaAs–GaAsP–GaAs ($\lambda > 1.17$ µm) Quantum-Well Lasers". In: *IEEE Transactions on Quantum Electronics* **38**, p. 640 (2002) (cit. on p. 19).

[142] Manfred Hammer. *1-D mode solver for dielectric multilayer slab waveguides* (cit. on pp. 20, 77).

[143] Manfred Hammer. *2-D multilayer waveguide mode solver variational effective index approximation* (cit. on pp. 20, 81).

[144] Basil W. Hakki and Thomas L. Paoli. "cw degradation at 300°K of GaAs double-heterostructure junction lasers. II. Electronic gain". In: *Journal of Applied Physics* **44**, p. 4113 (1973) (cit. on p. 20).

[145] Basil W. Hakki and Thomas L. Paoli. "Gain spectra in GaAs double-heterostructure injection lasers". In: *Journal of Applied Physics* **46**, p. 1299 (1975) (cit. on p. 20).

[146] D. J. Bossert and D. Gallant. "Improved method for gain/index measurements of semiconductor lasers". In: *Electronics Letters* **32**, p. 338 (1996) (cit. on p. 20).

[147] Huiling Wang and D. T. Cassidy. "Gain Measurements of Fabry-Perot Semiconductor Lasers Using a Nonlinear Least-Squares Fitting Method". In: *IEEE Journal of Quantum Electronics* **41**, p. 532 (2005) (cit. on p. 20).

[148] Y. Barbarin et al. "Gain Measurements of Fabry-Perot InP/InGaAsP lasers using an Ultra High Resolution Spectrometer". In: *Applied Optics* **45**, p. 9007 (2006) (cit. on p. 20).

[149] L. J. P. Ketelsen. "Simple technique for measuring cavity loss in semiconductor lasers". In: *Electronics Letters* **30**, p. 1422 (1994) (cit. on p. 21).

[150] Kam Y. Lau and A. Yariv. "Ultra-High Speed Semiconductor Lasers". In: *IEEE Journal of Quantum Electronics* **21**, p. 121 (1985) (cit. on p. 21).

[151] Larry A. Coldren, Scott W. Corzine, and Milan Mashanovitch. *Diode Lasers and Photonic Integrated Circuits*. 2. edition. Wiley Series in Microwave and Optical Engineering. Wiley, 2012 (cit. on p. 22).

[152] J. E. Bowers. "High speed semiconductor laser design and performance". In: *Solid-State Electronics* **30**, p. 1 (1987) (cit. on p. 23).

[153] D. Tauber, G. Wang, R. S. Geels, J. E. Bowers, and L. A. Coldren. "Large and small signal dynamics of vertical cavity surface emitting lasers". In: *Applied Physics Letters* **62**, p. 325 (1993) (cit. on p. 23).

[154] R. Nagarajan, M. Ishikawa, T. Fukushima, R. S. Geels, and J. E. Bowers. "High Speed Quantum-Well Lasers and Carrier Transport Effects". In: *IEEE Journal of Quantum Electronics* **28**, p. 1990 (1992) (cit. on p. 23).

[155] T.R. Chen et al. "Very high modulation efficiency of ultralow threshold current single quantum well InGaAs lasers". In: *Electronics Letters* **29**, p. 1525 (1993) (cit. on p. 24).

[156] F. J. MacWilliams and N. J. A. Sloane. "Pseudo-Random Sequences and Arrays". In: *Proceedings of the IEEE* **64**, p. 1715 (1976) (cit. on p. 24).

[157] Matthias Kuntz. "Modulated InGaAs/GaAs Quantum Dot Lasers". PhD thesis. Technische Universität Berlin, 2006 (cit. on pp. 24, 39).

[158] Holger Schmeckebier. "Quantum-Dot-Based Semiconductor Optical Amplifiers for O-Band Optical Communication". PhD thesis. Technische Universität Berlin, 2017 (cit. on p. 24).

[159] Harold M. Manasevit. "Single-Crystal Gallium Arsenide on Insulating Substrates". In: *Applied Physics Letters* **12**, p. 156 (1968) (cit. on p. 25).

[160] H. M. Manasevit and W. I. Simpson. "The Use of Metal-Organics in the Preparation of Semiconductor Materials: I. Epitaxial Gallium-V Compounds". In: *Journal of The Electrochemical Society* **116**, p. 1725 (1969) (cit. on p. 25).

[161] H. M. Manasevit. "The Use of Metal-Organics in the Preparation of Semiconductor Materials: III. Studies of Epitaxial III-V Aluminum Compound Formation Using Trimethylaluminum". In: *Journal of The Electrochemical Society* **118**, p. 647 (1971) (cit. on p. 25).

[162] H. M. Manasevit, F. M. Erdmann, and W. I. Simpson. "The Use of Metalorganics in the Preparation of Semiconductor Materials: IV. The Nitrides of Aluminum and Gallium". In: *Journal of The Electrochemical Society* **118**, p. 1864 (1971) (cit. on p. 25).

[163] H. M. Manasevit. "The use of metalorganics in the preparation of semiconductor materials: Growth on insulating substrates". In: *Journal of Crystal Growth* **13-14**, p. 306 (1972) (cit. on p. 25).

[164] H. M. Manasevit and W. I. Simpson. "The Use of Metalorganics in the Preparation of Semiconductor Materials: V. The Formation of In-Group V Compounds and Alloys". In: *Journal of The Electrochemical Society* **120**, p. 135 (1973) (cit. on p. 25).

[165] H. M. Manasevit and W. I. Simpson. "The Use of Metalorganics in the Preparation of Semiconductor Materials: VI. Formation of IV-VI Lead and Tin Salts". In: *Journal of The Electrochemical Society* **122**, p. 444 (1975) (cit. on p. 25).

[166] H. M. Manasevit and K. L. Hess. "The Use of Metalorganics in the Preparation of Semiconductor Materials: VII. Gallium Antimonide". In: *Journal of The Electrochemical Society* **126**, p. 2031 (1979) (cit. on p. 25).

[167] H. M. Manasevit. "Recollections and reflections of MO-CVD". In: *Journal of Crystal Growth* **55**, p. 1 (1981) (cit. on p. 25).

[168] H. M. Manasevit, W. B. Hewitt, A. J. Nelson, and A. R. Mason. "The Use of Metalorganics in the Preparation of Semiconductor Materials: VIII. Feasibility Studies of the Growth of Group III-Group V Compounds of Boron by MOCVD". In: *Journal of The Electrochemical Society* **136**, p. 3070 (1989) (cit. on p. 25).

[169] G. B. Stringfellow. *Organometallic Vapor-Phase Epitaxy: Theory and Practice*. 2nd edition. Academic Press, 1999 (cit. on p. 25).

[170] John E. Ayers. *Heteroepitaxy of semiconductors: theory, growth, and characterization*. CRC Press, 2007 (cit. on p. 25).

[171] Thomas F. Kuech and Tatau Nishinaga, eds. *Handbook of Crystal Growth. Thin Films and Epitaxy: Basic Techniques*. 2. edition. Elsevier, 2015 (cit. on p. 25).

[172] Tim David Germann. "Design and realization of novel GaAs based laser concepts". PhD thesis. Technische Universität Berlin, 2012 (cit. on p. 26).

[173] A. Strittmatter et al. "Suppression of the wavelength blue shift during overgrowth of InGaAs-based quantum dots". In: *Journal of Crystal Growth* **310**, p. 5066 (2008) (cit. on pp. 26, 27).

[174] Dominik Kriegner, Eugen Wintersberger, and Julian Stangl. "*xrayutilities*: a versatile tool for reciprocal space conversion of scattering data recorded with linear and area detectors". In: *Journal of Applied Crystallography* **46**, p. 1162 (2013) (cit. on p. 27).

[175] Don T. Cromer and Joseph B. Mann. "X-ray scattering factors computed from numerical Hartree-Fock wave functions". In: *Acta Crystallographica* **A24**, p. 321 (1967) (cit. on p. 28).

[176] Marc De Graef and Michael E. McHenry. *Structure of Materials: An Introduction to Crystallography, Diffraction and Symmetry*. Cambridge University Press, 2007 (cit. on p. 28).

[177] Jens Als-Nielsen and Des McMorrow. *Elements of Modern X-ray Physics*. John Wiley & Sons, Inc., 2011 (cit. on p. 30).

[178] D. E. Savage et al. "Determination of roughness correlations in multilayer films for x-ray mirrors". In: *Journal of Applied Physics* **69**, p. 1411 (1991) (cit. on p. 30).

[179] D. E. Savage, N. Schimke, Y.-H. Phang, and M. G. Lagally. "Interfacial roughness correlation in multilayer films: Influence of total film and individual layer thicknesses". In: *Journal of Applied Physics* **71**, p. 3283 (1992) (cit. on p. 30).

[180] V. Holý, J. Kubena, I. Ohli'dal, K. Lischka, and W. Plotz. "X-ray reflection from rough layered systems". In: *Physical Review B* **47**, p. 15896 (1993) (cit. on p. 30).

[181] Miho Yasaka. "X-ray thin-film measurement techniques: V. X-ray reflectivity measurement". In: *The Rigaku Journal* **26**, p. 1 (2010) (cit. on p. 30).

[182] D. K. G. de Boer. "Glancing-incidence x-ray fluorescence of layered materials". In: *Physical Review B* **44**, p. 498 (1991) (cit. on p. 31).

[183] Andreas Lesnik, Jürgen Bläsing, Jonas Hennig, Armin Dadgar, and Alois Krost. "Characterization of AlInN/AlN/GaN FET structures using x-ray diffraction, x-ray reflectometry and grazing incidence x-ray fluorescence analysis". In: *Journal of Physics D: Applied Physics* **47**, p. 355106 (2014) (cit. on p. 31).

[184] J. A. Bearden and A. F. Burr. "Reevaluation of X-Ray Atomic Energy Levels". In: *Reviews of Modern Physics* **39**, p. 125 (1967) (cit. on p. 32).

[185] S. I. Salem and P. L. Lee. "Experimental Widths of K and L X-Ray Lines". In: *Atomic Data and Nuclear Data Tables* **18**, p. 233 (1976) (cit. on p. 31).

[186] Joyce Alvin Bearden. "X-ray Wavelengths". In: *Reviews of Modern Physics* **39**, p. 78 (1967) (cit. on pp. 32, 48).

[187] Matthew S. J. Marshall and Martin R. Castell. "Scanning tunneling microscopy of epitaxial nanostructures". In: *Chemical Society Reviews* **43**, p. 2226 (2014) (cit. on p. 33).

[188] Marius Grundmann, ed. *Nano-Optoelectronics: Concepts, Physics and Devices*. Springer, 2002 (cit. on pp. 33, 34).

[189] M. A. Herman, D. Bimberg, and J. Christen. "Heterointerfaces in quantum wells and epitaxial growth processes: Evaluation by luminescence techniques". In: *Journal of Applied Physics* **70**, R1 (1991) (cit. on p. 35).

[190] Claus Klingshirn. *Semiconductor Optics*. 4. edition. Graduate Texts in Physics. Springer, 2012 (cit. on p. 35).

[191] Jürgen Christen. "Bestimmung der atomaren Morphologie von GaAs/AlGaAs-Heterogrenzflächen mittels Lumineszenzuntersuchungen". PhD thesis. Technische Universität Berlin, 1988 (cit. on pp. 36, 57).

[192] Sven Rodt. "Exzitonische Komplexe in einzelnen III-V Quantenpunkten". PhD thesis. Technische Universität Berlin, 2006 (cit. on p. 36).

[193] Oliver Schulz. "Einfluss lokaler Materialmodifikationen auf die Eigenschaften von Halbleiterlasern". PhD thesis. Technische Universität Berlin, 2007 (cit. on p. 38).

[194] Kristijan Posilović. "Neuartige Wellenleiterkonzepte für brillante Halbleiterlaser". PhD thesis. Technische Universität Berlin, 2015 (cit. on pp. 38, 78).

[195] E. F. Schubert and W. T. Tsang. "Photoluminescence line shape of excitons in alloy semiconductors". In: *Physical Review B* **34**, p. 2991 (1986) (cit. on pp. 41, 58).

[196] J. Christen and D. Bimberg. "Line shapes of intersubband and excitonic recombination in quantum wells: Influence of final-state interaction, statistical broadening, and momentum conservation". In: *Physical Review B* **42**, p. 7213 (1990) (cit. on pp. 41, 57).

[197] B. L. Henke, E. M. Gullikson, and J. C. Davis. "X-ray Interactions: Photoabsorption, Scattering, Transmission, and Reflection at E = 50-30,000 eV, Z = 1-92". In: *Atomic Data and Nuclear Data Tables* **54**, p. 181 (1993) (cit. on p. 48).

[198] Stephen Brunauer, Paul Hugh Emmett, and Edward Teller. "Adsorption of Gases in Multimolecular Layers". In: *Journal of the American Chemical Society* **60**, p. 309 (1938) (cit. on p. 49).

[199] Eric Jones, Travis Oliphant, Pearu Peterson, et al. *SciPy: Open source scientific tools for Python*. 2001 (cit. on p. 60).

[200] Y. P. Varshni. "Temperature dependence of the energy gap in semiconductors". In: *Physica* **34**, p. 149 (1967) (cit. on p. 61).

[201] R. Pässler. "Basic Model Relations for Temperature Dependencies of Fundamental Energy Gaps in Semiconductors". In: *physica status solidi (b)* **200**, p. 155 (1997) (cit. on p. 61).

[202] L. Brusaferri et al. “Thermally activated carrier transfer and luminescence line shape in self-organized InAs quantum dots”. In: *Applied Physics Letters* **69**, p. 3354 (1996) (cit. on p. 62).

[203] Petr G. Eliseev, Piotr Perlin, Jinhyun Lee, and Marek Osiński. “"Blue" temperature-induced shift and band-tail emission in InGaN-based light sources”. In: *Applied Physics Letters* **71**, p. 569 (1997) (cit. on p. 62).

[204] Petr G. Eliseev, Marek Osinski, Jinhyun Lee, Tomoya Sugahara, and Shiro Sakai. “Band-Tail Model and Temperature-Induced Blue-Shift in Photoluminescence Spectra of $In_xGa_{1-x}N$ Grown on Sapphire”. In: *Journal of Electronic Materials* **29**, p. 332 (2000) (cit. on p. 62).

[205] S. Sanguinetti et al. “Carrier thermal escape and retrapping in self-assembled quantum dots”. In: *Physical Review B* **60**, p. 8276 (1999) (cit. on p. 62).

[206] L. Grenouillet et al. “Evidence of strong carrier localization below 100 K in a GaInNAs/GaAs single quantum well”. In: *Applied Physics Letters* **76**, p. 2241 (2000) (cit. on p. 62).

[207] P. G. Eliseev. “The red σ^2/kT spectral shift in partially disordered semiconductors”. In: *Journal of Applied Physics* **93**, p. 5404 (2003) (cit. on p. 62).

[208] Y. G. Hong, A. Nishikawa, and C. W. Tu. “Effect of nitrogen on the optical and transport properties of $Ga_{0.48}In_{0.52}N_yP_{1-y}$ grown on GaAs(001) substrates”. In: *Applied Physics Letters* **83**, p. 5446 (2003) (cit. on p. 62).

[209] A. Bell et al. “Exciton freeze-out and thermally activated relaxation at local potential fluctuations in thick $Al_xGa_{1-x}N$ layers”. In: *Journal of Applied Physics* **95**, p. 4670 (2004) (cit. on p. 62).

[210] M. Hugues, B. Damilano, J.-Y. Duboz, and J. Massies. “Exciton dissociation and hole escape in the thermal photoluminescence quenching of (Ga,In)(N,As) quantum wells”. In: *Physical Review B* **75**, p. 115337 (2007) (cit. on p. 62).

[211] T. Nuytten et al. “Charge separation and temperature-induced carrier migration in $Ga_{1-x}In_xN_yAs_{1-y}$ multiple quantum wells”. In: *Physical Review B* **84**, p. 045302 (2011) (cit. on p. 62).

[212] Aymeric Maros, Nikolai N. Faleev, Mariana I. Bertoni, Christiana B. Honsberg, and Richard R. King. "Carrier localization effects in $GaAs_{1-x}Sb_x$/GaAs heterostructures". In: *Journal of Applied Physics* **120**, p. 183104 (2016) (cit. on p. 62).

[213] A. E. Zhukov et al. "Gain characteristics of quantum dot injection lasers". In: *Semiconductor Science and Technology* **14**, p. 118 (1999) (cit. on pp. 79, 81).

[214] Weng W. Chow and Frank Jahnke. "On the physics of semiconductor quantum dots for applications in lasers and quantum optics". In: *Progress in Quantum Electronics* **37**, p. 109 (2013) (cit. on p. 81).

Acknowledgements

As with all works, a lot of work, time and patience was necessary to bring it to completion. But even more than that, many people contributed in various ways, be they small or large. I want to use this opportunity to express my sincere gratitude to them and hope the people I missed will forgive me.

- Prof. Dr. Dieter Bimberg for giving me the opportunity to learn and work in his group, as well as his continuous interest in this work and the support that came with it.
- Prof. Dr. André Strittmatter for being the best teacher and supervisor I can think of.
- Prof. Dr. Armin Dadgar who provided never-ending knowledge concerning anything epitaxy-related and for taking over the third review.
- Prof. Dr. Kathy Lüdge for acting as chair for the examination board.
- Jan-Hindrik Schulze for teaching me about epitaxy, material characterization, and how to critically evaluate almost anything that comes your way as well being a very pleasant office neighbor.
- Kathrin Schatke who always found or made time to fix the epitaxy machine.
- Dr. Holger Schmeckebier who was always willing to lend a helping hand and a listening ear whenever things didn't go as planned.
- Ronny Schmidt for providing guidance and help in anything cleanroom-related and for always being open to a brainstorming session, regardless of topic.
- Dejan Arsenijević who did about most, if not all of the dynamic laser measurements.

- Dr. Gernot Stracke and Dr. Tim Germann for a pleasant work atmosphere as well as for help and advice.
- Dr. Andrei Schliwa for the eight-band k·p simulations.
- Christopher Prohl, Andrea Lenz, Holger Eisele and Zeno Diemer for the XSTM images.
- Manuel Gschrey and Dr. Sven Rodt for the CL measurements.
- Dr. Jürgen Bläsing for providing the GIXRF and XRR measurements.
- Stefan Bock and Rene Linke for maintenance support.
- My family, for everything.